ISSN: 2792-0771

Seatific

Volume 3
Number 2
Year 2023

YTÜ PRESS

seatific.yildiz.edu.tr

ISSN: 2792-0771

Seatific

Volume 3 Number 2 Year 2023

ISSN: 2792-0771

Seatific

Volume 3 Number 2 Year 2023

Journal Contacts

Editor-in-Chief: Ümit Güneş, *Yıldız Technical University, İstanbul, Türkiye*
ugunes@yildiz.edu.tr

Owner on behalf of the Yıldız Technical University: Prof. Dr. Tamer Yılmaz
Journal Description: The journal is supported by Yildiz Technical University officially, and is a blind peer-reviewed free open-access journal, published two times a year.
Publisher: Yildiz Technical University - YTU Press
Language of Publication: English
Frequency: Two issues
Publication Type: Online e-version
Press Date: December 2023

Seatific
Volume 3 Number 2 Year 2023

Aim & Scope

Seatific Journal aims to present academic data to all stakeholders in the field, taking into account current developments in all types of areas related to shipping and marine sciences such as environmental impacts, energy transition, and artificial intelligence. Seatific Journal strongly aims to only publish innovative and novel studies that will contribute significantly to advancements in the fields of marine engineering, marine science, and technology.

- Aquaculture and Fishing
- Construction
- Coastal Development
- Design
- Electrical Equipment
- Emissions
- Energy
- Hydrodynamics
- Social Aspects
- Logistics
- Machinery and Control
- Marine Engines
- Marine Environment
- Materials
- Navigation
- Noise
- Manoeuvrability
- Off-Shore
- Port Operations
- Propulsion
- Protection of the Environment
- Renewable Energy
- Safety
- Seakeeping
- Ship Resistance
- Shipyards
- Stability
- Structures

ISSN: 2792-0771

Seatific

Volume 3 Number 2 Year 2023

Contents

Research Articles

Review

Seatific
Volume 3 Number 2 Year 2023

Author Guidelines

• Seatific Journal is a double-blind, peer-reviewed biannually academic journal publishing articles in both English and Turkish.
• Author(s) should remove all author(s)' names and any personal information that can be used to identify the author(s).
• All articles submitted to Seatific Journal will be uploaded to iThenticate to check the similarity rate of the paper. The Seatific Journal Desk immediately rejects any articles with a similarity rate greater than 10%.
• All submitted articles to Seatific Journal are uploaded to iThenticate to check the similarity ratio of the paper. If the similarity is more than 10%, the article is directly rejected by the Seatific Journal Desk.
• In order to gain acceptance, all articles submitted to Seatific Journal for evaluation are required to have never previously been published.
• Submissions are first reviewed by the editorial board. If an article satisfies the necessary conditions for style and content, reviewers will then proceed to evaluate its suitability for publication.
• Articles under the categories listed below are acceptable for publication:

Research Articles reflecting original experimental and/or theoretical research. A coherent treatment emphasizing new insight is expected rather than a simple accumulation of data.

Review Articles including authoritative reviews of recent advances in the basic and applied sciences with emphasis on the fundamental aspects of the subject. Manuscripts are generally longer than those found in other categories, but contributions dealing in part with original research are not excluded. Contributors who are invited by the editors or who may submit outline proposals directly are offered a small royalty upon the publication of the article.

• All articles undergo evaluation by two anonymous reviewers. If necessary, the article may be sent to a third reviewer for further assessment. The publication of an article depends upon the approval of these reviewers. Author(s) must provide the necessary corrections demanded by the reviewers.
• In general, any submitted work should provide the following formatting conditions.

No page limit or required format is needed for initial submission. A template will be sent to the author(s) of accepted articles. This can also be downloaded from the link below.

Articles should be written in MS Word in Times New Roman script with 12-pt font size, spacing of 1.5 lines, 2.5 cm margins, and left-aligned.

Tables, figures, pictures, and graphs should fit within a journal page (A4). If needed, these may be written with smaller font sizes and single-spaced.

Tables and graphs should be numbered consecutively as they appear in the text. Place footnotes for tables below the table body and indicate them with superscript lowercase letters. Avoid vertical text layout. Be sparing in the use of tables, and ensure that the data presented in tables do not duplicate results described elsewhere in the article.

• Author(s) and article information should be filled out completely on the form in the system. The article should not contain any information about the author(s).
• The study must include an abstract between 150-200 words in length and 5-8 keywords.
• Author(s) should reference and explain every figure, table, and equation used in the article.
• Corresponding author(s) should also fill out the author contributions form.
• Articles should be submitted using the online submission system to initiate the editing process. An automatic confirmation e-mail will be sent after submission. If you do not receive this e-mail, please contact us via e-mail at seatific@yildiz.edu.tr
• Seatific Journal uses APA 7th Edition style formatting for references and citations. The text rules and formats specified by the Publication Manual of the American Psychological Association (APA), Seventh Edition are to be followed both for text citations and the reference list. Here are some reference examples.

Book/eBook

• Reference Section: Bejan, A., Tsatsaronis, G., & Moran, M. J. (1996). Thermal design and optimization. Wiley.
• *In-Text:* (Bejan et al., 1996)

Edited Book

• Reference Section: Torino, G. C., Rivera, D. P., Capodilupo, C. M., Nadal, K. L., & Sue, D. W. (Eds.). (2019). Microaggression theory: Influence and implications. John Wiley & Sons. https://doi.org/10.1002/9781119466642
• *In-Text:* (Torino et al., 2019)

Journal Article

• Reference Section: Bejan, A., Gunes, U., & Sahin, B. (2019). The evolution of air and maritime transport. Applied Physics Reviews, 6(2), 021319. https://doi.org/10.1063/1.5099626
• *In-Text:* (Bejan et al., 2019)

Unpublished Dissertation or Thesis

• Reference Section: Dostal, V. (2004). A supercritical carbon dioxide cycle for next generation nuclear reactors [Unpublished doctoral dissertation]. Massachusetts Institute of Technology.
• *In-Text:* (Dostal, 2004)

Seatific
Volume 3 Number 2 Year 2023

Ethical Principles and Policies

Author Policy

Manuscript submission means the work has not been previously published (except in summary form, as part of a published conference or any academic thesis, or as an electronic preprint); it has not been evaluated anywhere else for publication; It also means that all authors or the responsible authorities of the work have given their consent to the publication of the work in question, without express or public declaration, and if accepted, its copyright in English or another language such that it cannot be published elsewhere, including electronically, without the permission of the owner.

All articles submitted to Seatific Journal will be uploaded to iThenticate to check the similarity rate of the paper. The Seatific Journal Desk immediately rejects any articles with a similarity rate greater than 10%.

Editor Policy

The Seatific Journal asks its editors to write a short commentary on their views that could potentially be seen as influencing their unbiased assessment. Such transparency is a requirement of an ethical obligation to authors and readers, as well as an equal response to the expression of opinion expected from authors, reviewers, and reviewers. The editorial staff is expected to distance themselves from decision-making arrangements that could potentially introduce a disagreement. Editors' duties:

- Publishing Decision
- Impartiality
- Security
- Disagreements and Statement
- Collaboration to take part in research

Review Policy

Reviewers of Seatific Journal are chosen from among the experts on the subjects mentioned in the manuscripts. The reasons for their selection are due to their objectivity and scientific knowledge. All those who will make the assessments are informed about what Seatific Journal expects of them. Each of them is asked to fill in an evaluation form and, if necessary, to prepare a separate report. Persons who have a disagreement on the topic of a manuscript cannot evaluate it (for example, someone who has contributed to or collaborated with one of the authors, or who is unable to provide an objective opinion on the work; also an employee or competitor of an institution whose work is being reviewed, such as people with special political and ideological views). These people should contact the editorial board and state a possible difference of opinion/conflict of interest before the manuscript is submitted to the referee committee.

- Reviews are expected to be professional, honest, courteous, punctual, and constructive. The essential elements required for a high-quality assessment are:
- Reviewers should identify the weaknesses and strengths of the work organization and methodology and comment on them.
- Reviewers should accurately and constructively criticize the author's ability to handle data (taking into account that data may be limited).
- Reviewers should identify the strengths and weaknesses of the work as a written communication tool, regardless of its composition, methodology, results, and handling.
- Reviewers should express their thoughts on whether the study has content that may raise ethical concerns or whether it has low scientific standards.
- Reviewers should provide helpful advice to the authors so that the work can be improved.
- Reviewers' criticism should be constructive and professional towards the author.
- The review should provide the editor with the correct perspective and content so that he or she can decide on acceptance (and/or revision) of the work (and/or revision).
- Reviewers are expected to identify unused works and to use citations to indicate which elements of the work have been cited previously. Reviewers should also report striking similarities between the reviewed text and any work published in another journal or submitted to Seatific Journal.
- Reviewers are sensitively expected not to contact the author directly. In many cases, the opinion of two experts will be sought; however, the views of these experts may not be the same as the final decision of the editor on the manuscript in question. Receiving advice from a reviewer, even partial, may give authors the wrong impression of the review process.

Data Access

All data on manuscripts must be available as supplementary files or stored in an external channel; they should also be made available upon request.

Changes in the Author Staff

Seatific Journal acknowledges the reorganization and addition or deletion of author names prior to publishing an accepted work. Before publishing the accepted work, requests such as adding, removing, or rearranging the names of the authors should be forwarded to Seatific Journal's Secretary by the corresponding author. This request should include:

The reason for adding, removing, or rearranging the name in question and the written consent of all authors separately (by e-mail, fax, or letter) stating that they agree with this addition, removal, or rearrangement. It should also include the approval of the author who is being added or removed in such cases.

Seatific
Volume 3 Number 2 Year 2023

Ethical Principles and and Policies

Requests not originally sent by the corresponding author will be sent by Seatific Journal's Secretary directly to the author, who must follow the procedure outlined above. The following should be noted: (1) Seatific Journal's Secretary will notify the journal's editorial board of such requests, and (2) publication of accepted work in the press will be frozen until consensus is reached on the authoring staff. After the work is published, requests to add, remove, or rearrange author names will no longer be considered.

Copyright

Authors are required to include a copyright acknowledgment letter with the manuscripts they submit to Seatific Journal. An example of this approval is below.

"The attached manuscript(s), whose author(s) and title(s) are clearly stated below, have been submitted for your consideration to be published in Seatific Journal. This manuscript/these manuscripts has/have not been published anywhere before or sent to another journal for evaluation. If any or all of the manuscripts are accepted for publication, we declare that we accept all subsequent reprint rights of each individual manuscript to belong solely and exclusively to Seatific Journal.

As the undersigned author(s), I/we accept the conditions in the Authors' Guide and expressly confirm that the paper/articles below have been written in accordance with the ethical rules set forth in this guide. In addition, all the manuscripts in question are original works, have been submitted with the documents of original copyrights, the author(s) has/have transferred all correction and control rights to Seatific Journal, and all rights including proprietary copyrights are retained if the work(s) is/are accepted. I also accept that I have transferred these rights to Seatific Journal."

Ethics & Policies

In papers to be published in journals, the manuscript should state whether ethics committee permission and/or legal/ special permission is required. If it is necessary to obtain these permissions, it should be clearly presented from which institution, on what date, and with what decision or issue number.

Developing the Evaluation Process

Seatific Journal's editors routinely review manuscripts for quality. Evaluation-attributed grading and other evaluator performance characteristics are periodically reviewed to ensure optimal efficiency for Seatific Journal. Performance measures such as review completion time should be used to review changes during processes that will contribute to the journal's efficiency. Individual performances are kept confidential. Editors who do not contribute to the quality of Seatific Journal may be removed from the editorial board.

Privacy

Information and ideas gained as a referee during the evaluation process are kept confidential and may not be used advantageously in any way. As the application is a privileged notification, it is to be kept strictly confidential.

- The application cannot be taken or copied by the evaluators. In addition, reviewers cannot share the work with their colleagues without the written permission of the editor.
- Reviewers and editors cannot make professional or personal use of the data, interpretations, or topics in the work (unless directly related to the evaluation) or write editorials or commentaries on the work before its publication unless they have the implicit permission of the authors.
- In case of any difference of opinion/conflict of interest, the evaluators should notify the editorial board.
- Evaluators should notify Seatific Journal if they are unable to review any work, or if they can only do so with some delay.
- Evaluators should objectively evaluate the quality of the work in question; make clear, unbiased, and constructive criticisms; and avoid personal criticism of the authors. There is no harm in letting the authors know/see the comments made by the referees. Therefore, the opinions of the referees should be clearly stated and supported so that the authors can understand the basis of the comments and evaluations.
- Reviewers can easily report any violation to the editor if they suspect any and, at the same time, they should strictly not share the status with other parties unless they have been informed by Seatific Journal to do so.

Price Policy

Seatific Journal does not demand any article processing or submission charges from authors.

Seatific, Vol. 3, Issue. 2, pp. 43–50, December 2023

Seatific Journal
https://seatific.yildiz.edu.tr
DOI: https://doi.org/10.14744/seatific.2023.0006

Seatific

Research Article

Numerical investigation into the effect of duct use on the performance of controllable pitch propellers

Ahmet YURTSEVEN*

Department of Marine Engineering, Yıldız Technical University, Faculty of Naval Architecture and Maritime, İstanbul, Türkiye

ARTICLE INFO

Article history
Received: May 27, 2023
Revised: September 11, 2023
Accepted: October 03, 2023

Key words:
CFD; CPP; duct; ducted propeller; spindle torque

ABSTRACT

This study uses CFD methods to solve the complex flow around a CPP propeller with ducts and aims to investigate the performance differences between ducted and non-ducted propeller designs. In particular, the values for pitch changes and blade spindle torques have been determined at different advance ratios. The study uses STAR-CCM+, a commercial computational fluid dynamics (CFD) code, and has preferred the k-ε model to predict turbulence in the flow. In addition to the thrust coefficient, torque coefficient, and propeller efficiency, the study also examines blade spindle torque, whichprovides movement to the propeller blades. The use of ducts at low advance ratios is found to be beneficial in terms of both improving performance and reducing torque.

Cite this article as: Yurtseven A. Numerical investigation into the effect of duct use on the performance of controllable pitch propellers. Seatific 2023;3:2:43–50.

1. INTRODUCTION

Propeller efficiency is the most important parameter affecting propulsion system efficiency in marine vessels. One of the methods applied to increase propeller efficiency is to change the pitch angles of the propeller blades based on vehicle speed while keeping propeller speed constant. Propellers that can perform this maneuver are called controllable pitch propellers (CPP). Another application is to make the propellers work within a non-movable nozzle (duct). These types of propellers are called ducted propellers.

Two types of ducted propeller structures are often used on ships (Celik et al., 2011). The first is the accelerating ducted propeller system that accelerates the flow on heavily loaded and diameter-restricted propellers, and the second is the decelerating ducted propeller system, which increases static pressure by slowing down the flow over the propeller to delay propeller cavitation. System efficiency has been observed to increase with the additional loading of the duct in ducted propellers. However, the additional loading of the duct is limited to the current separation at the duct. Propellers with current accelerating ducts are generally used in tug-like vessels that perform pushing and pulling operations. They are also preferred on research vessels, drilling platforms, and marine vessels that require the ability to hold position (Oosterveld, 1972).

Trawlers also use ducted propellers due to the need for a high thrust ratio at a low advance ratio. Methods based on computational fluid dynamics (CFD) can be used for the design and operating parameters of ducted propellers used in these types of boats (Caldas et al., 2019). Some studies are found in the literature on ducted propellers (Bhattacharyya et al., 2015, 2016b; Baltazar et al., 2019; Zhang et al., 2019, 2020; Gong et al., 2021; Zhang et al., 2021; Kim et al., 2022). Celik et al. (2010) developed an iterative design methodology for ducted propellers due

***Corresponding author.**
*E-mail address: ahmety@yildiz.edu.tr, yurtseven1@gmail.com

to the insufficient accuracy of classical propeller design methods under heavy loading conditions. Haimov et al. (2011) used several different types of ducts to obtain the combined effect of the Reynolds number and loading on thrust and torque by comparing model and full-scale calculations in turbulent flow, confirming the characteristics and efficiency gains of ducted propellers.

Ducts can be used with fixed pitch propellers as well as with controllable pitch propellers. In particular, the ability to change pitch in case of current separation, which can cause a decrease in thrust, has shown better characteristic values in controllable pitch propellers than in fixed pitch propellers (Elbatran et al., 2014). Very few ducted CPP propeller studies are found in the literature (Arief et al., 2021; Huisman et al., 2022). Panel methods working with potential theory have been used to analyze the performance of CPP propellers with nozzles. However, Liu et al. (2006) realized that viscous solutions should be used for torque values in particular.

Scaling effects are also found among studies. The scaling effects of both propellers and ducts have been investigated with regard to performance. Scaling effects were found to have a greater effect on the thrust from ducts than on propeller characteristics. The effect of the design and scale of the ducts on thrust with current separation has been shown to besignificant at high advance ratios. Much better results were obtained in the full-scale analysis of ducted propellers compared to scale models (Bhattacharyya et al., 2016a).

The operating procedures for CPP propellers require the blades to be rotated around their axis to change the pitch angle. This introduces the concept of spindle torque, which is not present in fixed-pitch propellers. A few studies are also found in the literature on the propeller blade spindle torque of CPP propellers (Godjevac et al., 2009; Jessup et al., 2009; Martelli et al., 2013; Tarbiat et al., 2014; Pourmostafaet al., 2021; Yurtseven et al., 2023). Determining blade spindle torques is also very important for aiding the design of CPP propellers and for avoiding excessive blade actuation pressures at the blade hub (Liu et al., 2015). The torque on the blade can be investigated numerically using potential theory verified by a simulation. Studies should also clearly analyze well the complex flow conditions around CPP propeller blades (Funeno et al., 2013).

This study uses CFD methods to analyze the complex flow around a ducted CPP propeller and aims to investigate the performance differences between ducted and non-ducted propeller designs. In particular, the values for pitch change and blade spindle torque have been determined at different advance ratios.

2. NUMERICAL MODELING

2.1. Governing equations

The analyses using computational fluid dynamics methods model the flow as three-dimensional, steady state, viscous, turbulent, and incompressible. This study has preferred the realizable k-epsilon turbulence model, with the continuity and steady state Reynolds averaged Navier-Stokes equations being as follows:

$$\frac{\partial U_i}{\partial x_i}=0 \tag{1}$$

$$pU_j\frac{\partial U_i}{\partial x_i}=-\frac{\partial P}{\partial x_i}+\frac{\partial \tau}{\partial x_j}-\frac{\partial\left(\overline{pu_i'u_j'}\right)}{\partial x_i} \tag{2}$$

where U_i is the average velocity vector, u' is the turbulence velocity vector, $pu_i'u_j'$ is the turbulence stress tensor, P is average pressure, p is density, and μ is dynamic viscosity. The study uses Simcenter Star CCM+ version 2020.3, a commercial CFD code. The solver applies the finite volume method to discretize the governing equations.

Both spatial and temporal discretization has been done with accurate second-order schemes to improve accuracy. The well-known SIMPLE algorithm is used for pressure-velocity matching. More information about the numerical solution can be found in the solver manual (Siemens, 2021).

Figure 1 shows a flow stream volume to represent the flow around the propeller. The dimensions in the figure are defined based on propeller diameter. The following conditions have been defined: uniform velocity inlet for the inlet surface, pressure outlet for the outlet surface, symmetry at the side surface, and no-slip for all other surfaces. This study was carried out by conducting analyses under open water propeller test conditions. As shown in Figure 2, propeller pitch changes

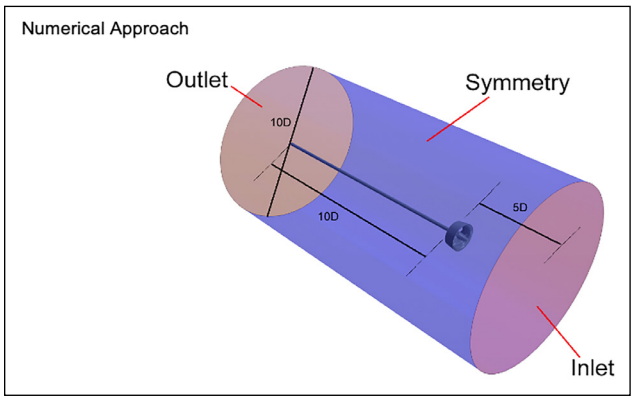

Figure 1. Solution volume and boundary types.

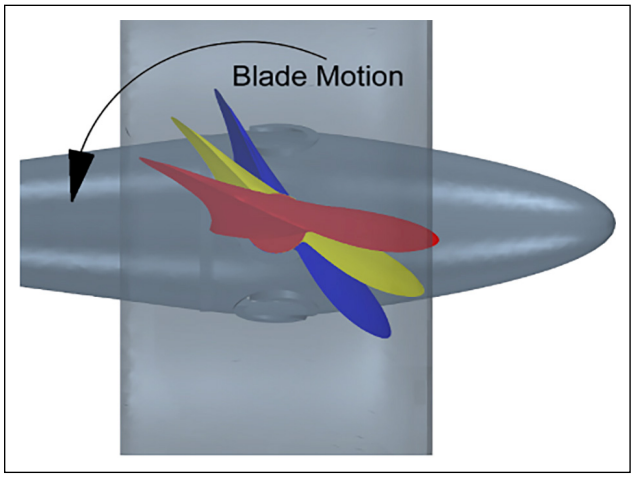

Figure 2. Propeller blade movement for changing pitch.

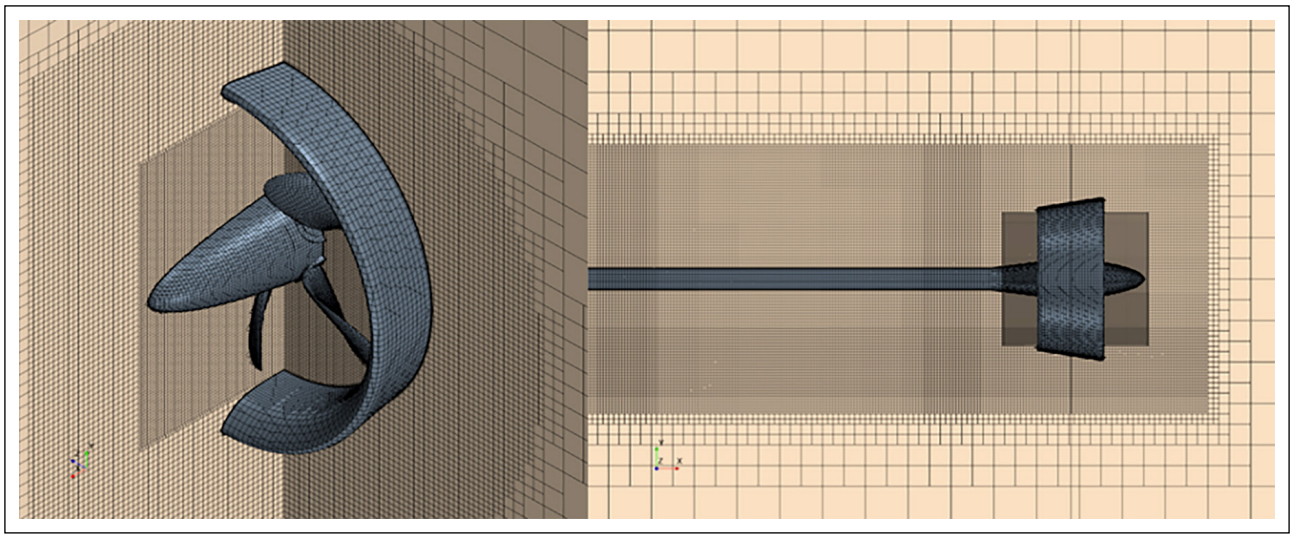

Figure 3. Detailed view of the solution grid.

were achieved through maneuvers that were obtained by rotating the propeller blades around the shaft axis.

CPP propellers'ability to change pitch angle (unlike FPP propellers) as well as to rotate around the main drive shaft also requires the blades to rotate around their own spindle axis. This leads to the need for an additional motion model in simulations. This study uses the motion reference frame for the propeller's main rotational motion. Although the overset motion model needed to be used for pitch changes, each pitch angle was generated and analyzed sequentially due to the simulations being run independently of time.

2.2. Grid structure

In order to analyze the solution volume using the finite volume method, a solution mesh consisting of unstructured hexahedral mesh elements was generated as shown in Figure 3.

Solution element refinement zones were designed for the propeller blades, shaft, hub, and duct based on the solution mesh. Prism layer elements are used close to the surfaces for accurate estimation of high-speed gradients.

2.3. Verification study

Roache's (1994) solution grid convergence index (GCI) method was used to determine the numerical uncertainty in the simulation studies. GCI is based on the Richardson extrapolation method, which estimates the exact numerical solution to be obtained using a zero-dimensional solution element through systematically obtained solution mesh results. GCI is also recommended by the American Society of Mechanical Engineers (ASME; Celik et al., 2008), International Towing Tank Conference (ITTC, 1999), and American Institute of Aeronautics and Astronautics (AIAA; Cosner et al., 2006) for numerical uncertainty assessments (Kim et al., 2021).

This study performed GCI by generating the solution mesh at three different resolutions. The basic size of the solution mesh elements were determined as shown by Equation 3.

$$h=\left[\frac{1}{N}\sum_{i=1}^{N}(\Delta V_i)\right]^{1/3} \tag{3}$$

where N is the number of solution elements, ΔV_i is the volume of each solution element, and h is the basic dimension. For the three different solution mesh resolutions (i.e., fine, medium, and coarse), the basic dimensions are h_1, h_2 and h_3 respectively. Refinement factors are taken as $r_{21}=h_2/h_1$, $r_{32}=h_3/h_2$. The equations used for calculating the GCI are as follow:

$$\varepsilon_{32}=\varphi_3-\varphi_2,\ \varepsilon_{21}=\varphi_2-\varphi_1 \tag{4}$$

where the φ values indicate the result of the analysis at each mesh resolution.

$$p=\frac{1}{\ln(r_{21})}\left|\ln\left|\varepsilon_{32}/\varepsilon_{21}\right|+q(p)\right| \tag{5}$$

$$q(p)=\ln\left(\frac{r_{21}^{p}-S}{r_{32}^{p}-S}\right) \tag{6}$$

$$S=1.\mathrm{sgn}\left(\varepsilon_{32}/\varepsilon_{21}\right) \tag{7}$$

The p value indicates the order value of the GCI method that is used.

$$\varphi_{ext}^{21}=(r_{21}^{p}\varphi_1-\varphi_2)/(r_{21}^{p}-1) \tag{8}$$

Table 1. Results from the GCI study (J=0.16)

	Value
N_1	8713836
N_2	4477850
N_3	2322435
$\square_1$	0.870
$\square_2$	0.864
$\square_3$	0.849
p	15.150
$\square^{21}_{\text{ext}}$	0.870
e^{21}_{a}	0.0069
e^{21}_{ext}	0.00018
GCI^{21}_{fine} (%)	0.023

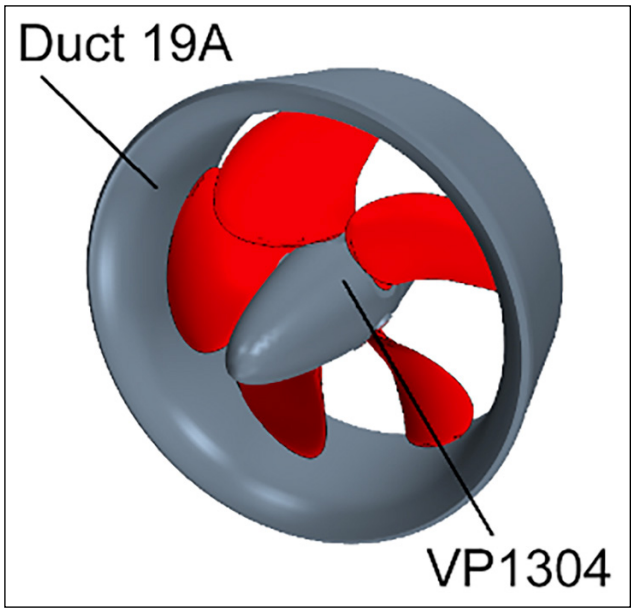

Figure 4. The VP1304 propeller and Duct 19A duct geometry.

$$e_a^{21} = \left| \frac{\varphi_1 - \varphi_2}{\varphi_1} \right| \quad (9)$$

$$e_{ext}^{21} = \left| \frac{\varphi_{ext}^{12} - \varphi_1}{\varphi_{ext}^{12}} \right| \quad (10)$$

$$GCI_{fine}^{21} = \frac{1.25 e_a^{21}}{r_{21}^{p} - 1} \quad (11)$$

The sub-index *ext* here indicates the exact value. Table 1 shows the results from the GCI study, with *N* indicating the number of cells, φ indicating the coefficient of thrust, and e indicating the error quantities. Thus, the solution grid was determined to be needed at a medium resolutionfor the analysis.

2.4. Problem description

2.4.1. Geometry

The study uses the 5-blade CPP test propeller VP1304 as shown in Figure 4 together with Duct 19A, a standard duct frequently encountered in the literature.

The geometric dimensions and details are given in Table 2.

2.5. Validation study

Figure 5 shows the comparison of the experimental data obtained under open water propeller test conditions with the results from the numerical study.

According to the data obtained at six different advance ratios, the results from the numerical study are understood to show good agreement with the experimental results.

Table 2. Geometric details of the VP1304 propeller

D	0.250 m
Blade number	5
Rotation direction	Right
$P_{0.7}/D$	1.635
Propeller Shaft	Downstream

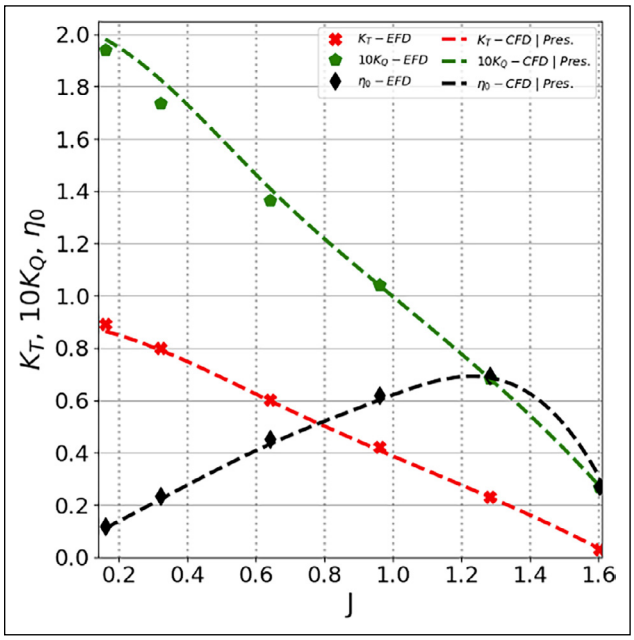

Figure 5. Experimental and numerical study results for the VP1304 propeller (Heinke, 2011).

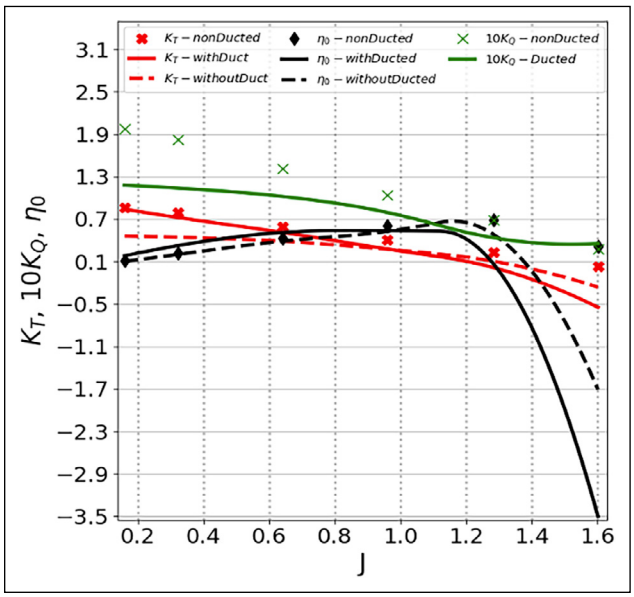

Figure 6. Performance coefficients for the ducted and non-ducted VP1304 CPP.

CPP: Controllable pitch propellers.

3. RESULTS

This section presents the numerical simulation results for the VP1304 test propeller and Duct 19A duct. The thrust coefficient, torque coefficient, and propeller efficiency have been analyzed based on the advance ratio, as frequently used in the literature, in order to determine the propeller operating performance. The results are also discussed in terms of the spindle torque coefficient as proposed by Yurtseven and Aktay (2023).

Figure 6 shows the propeller performance coefficients for the VP1304 propeller designs with and without Duct

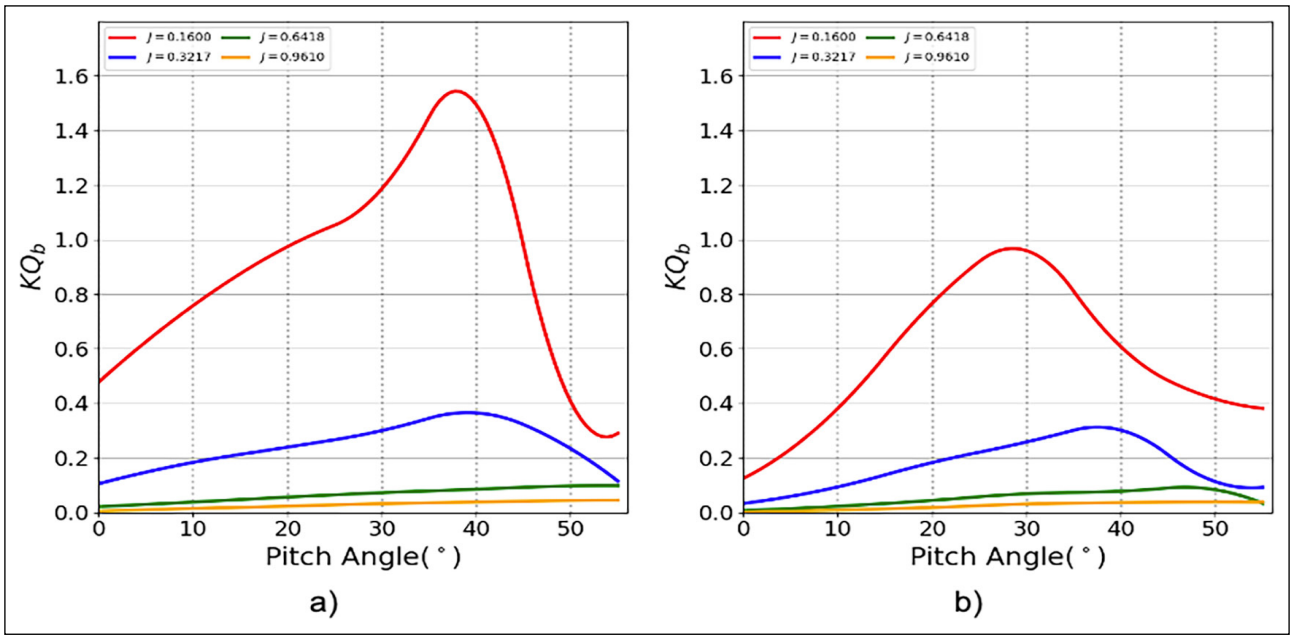

Figure 7. Spindle torque coefficient for (a) non-ducted propeller and (b) ducted propeller.

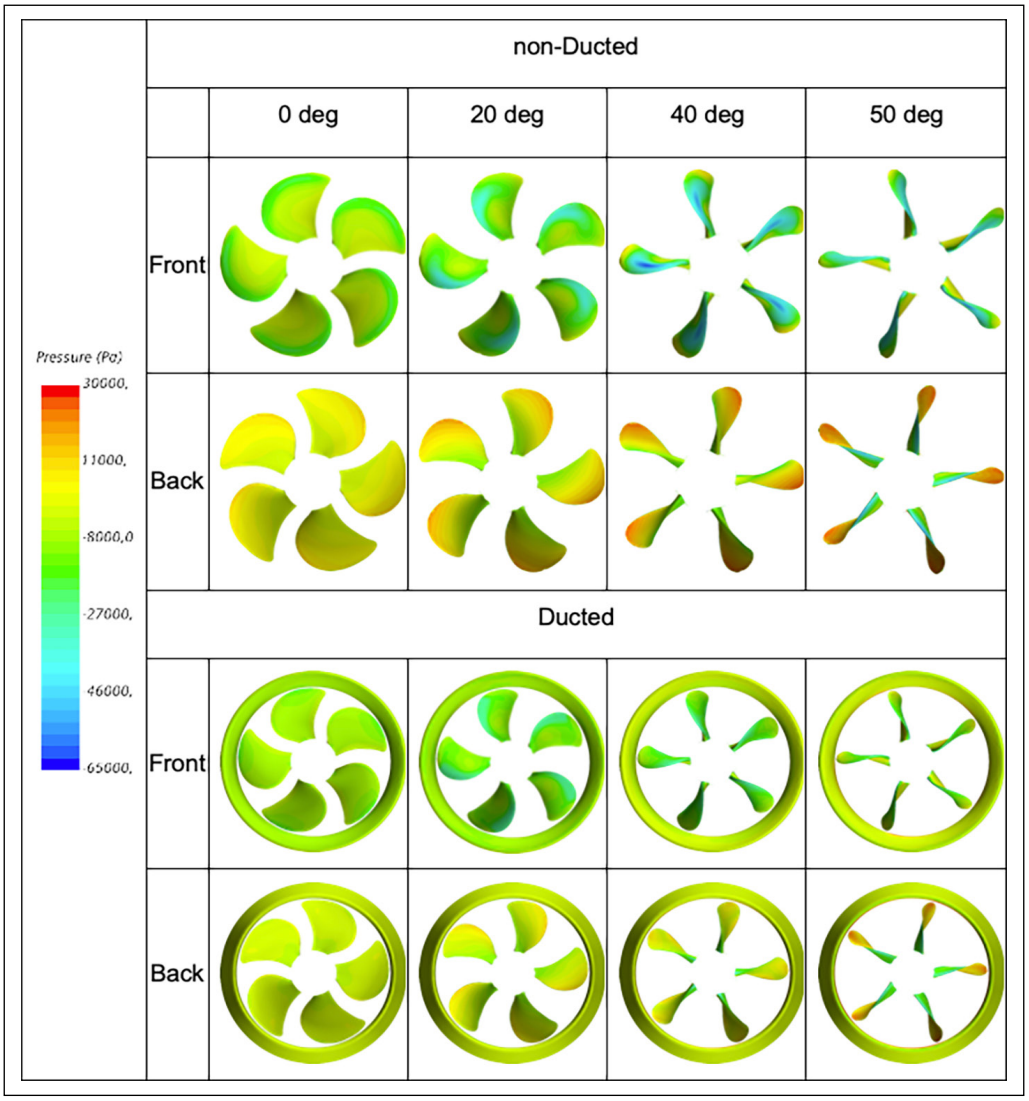

Figure 8. Upstream(front) and downstream(back) pressure distributions for non-ducted and ducted propellers (J=0.16).

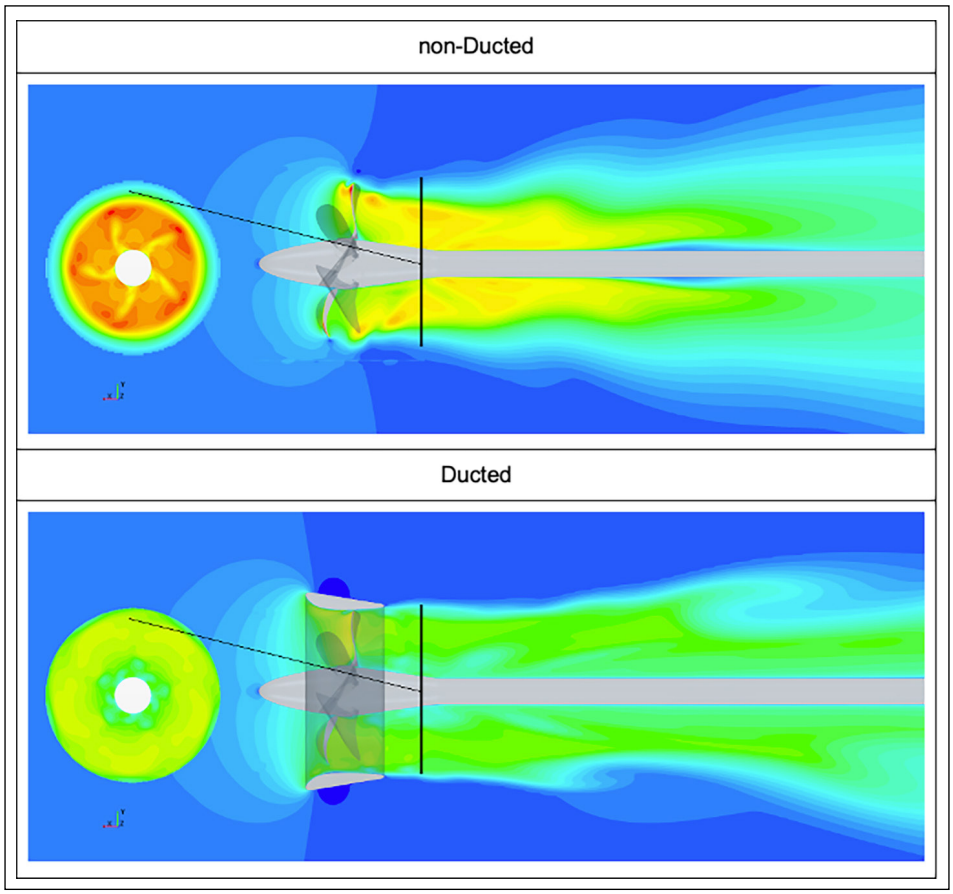

Figure 9. Velocity distributions along the longitudinal center planes of ducted and non-ducted propellers (J=0.16).

19A. In terms of thrust, two cases occur for the ducted propeller design. The ducted case shows the performance changes should be examined separately as those realized on the propeller itself and then the performance change on the propeller group, which can be called the ducted propeller group. An increase in the is known to decrease the propeller loading. For the ducted propeller, the thrust coefficient of the propeller alone gives lower values than the non-ducted propeller for all advance ratios. Although these values converge as the advance ratio increases, no specific high value was found. However, the thrust coefficient of the ducted propeller group gives very similar results to that for the non-ducted propeller at low advance ratios (i.e., under heavy load conditions). However, this similarity deteriorates negatively as the advance ratio increases.

In terms of propeller torque coefficient, the ducted propeller is seen to give significantly lower values, especially at low advance ratios. Therefore, it has a higher propeller efficiency than for the non-ducted propeller. However, this situation again converges to the torque coefficient of the non-ducted propeller, with the propeller efficiency decreasing significantly as the advance ratio increases.

Figure 7 gives thespindle torque coefficients for the VP1304 CPP propeller, ductedin Figure 7a and non-ducted in Figure 7b. The curves are plotted as a function of the change in blade pitch angle, with 0° indicating the design pitch of the propeller at full track and 55° indicating the feathering position. Figure 7a shows the highest value of the blade spindle torque coefficient to be obtained at a low advance ratio. The spindle torque coefficient is seen to decrease as the advance ratio increases. Figure 7b shows the highest spindle torque coefficient in the ducted design to decrease significantly compared to the non-ducted design and to occur at a lower pitch angle. This decrease is practically insignificant after the advance ratio increases to a certain point.

Figure 8 shows the pressure distributions at different pitch angles for the front face and back face for the ducted and non-ducted propeller designs at an advance ratio of J=0.16. In Figure 8, the front face shows the upstream region, and the back face shows the downstream region. The ducted propeller achieves a more homogeneous pressure distribution by increasing the pressure on the front face and decreasing the pressure on the back face, especially in the regions close to the blade tips up to a 40° pitch angle. In addition, because the flow is accelerated at all angles, a general reduction in the pressure distribution is obtained on the surfaces. In this case, the ducted design reduces the overall blade spindle torque on the propellers. However, the accelerated flow shows the blades to stall much earlier when changing pitch.

Figure 9 shows the velocity distributions on the longitudinal center plane for the ducted and non-ducted propeller designs. According to these velocity distributions, the use of a duct increases the current flowing through the propeller to about 3%,thus increasing efficiency and reducing the torque on the

blade shaft axis, which allows the blade to maneuver much more effectively. In addition, the wake zone distributions shown in Figure 9 also reveal the use of the duct to correct the propeller wake, thus contributing to the increase in efficiency.

4. CONCLUSION

This study placed a standard Duct 19A nozzle as a test duct on the VP1304 propeller, provided experimental data to the VP1304 as a CPP test propeller, and then examined the change in propeller performance.

At low advance ratios (i.e., under heavy load conditions), the blade spindle torque was observed to decrease for the ducted propeller compared to the non-ducted propeller.

Because the flow is accelerated and a homogeneous distribution of the wake is obtained in the ducted propeller, the thrust values of the ducted propeller group increased at low advance ratios. At the same time, an increase in propeller efficiency was also achieved.

The blade spindle torque, which provides the movement of the blades for pitch change in CPP propellers, was observed to besignificantly reduced in the ducted propeller. This reduction was also found to be more pronounced at low advance ratios, with the use of ducts also observed to cause the blades to stall earlier.

Future studies should investigate the cavitation behavior and flow-induced noise in ducted and non-ducted CPP propellers.

DATA AVAILABILITY STATEMENT

The published publication includes all graphics and data collected or developed during the study.

CONFLICT OF INTEREST

The author declared no potential conflicts of interest with respect to the research, authorship, and/or publication of this article.

ETHICS

There are no ethical issues with the publication of this manuscript.

FINANCIAL DISCLOSURE

The authors declared that this study has received no financial support.

REFERENCES

Arief, I. S., Baidowi, A., & Ulfa, M. (2021). Thrust and torque analysis on propeller c4-40 with the addition of kort nozzle to pitch variation. *International Journal of Marine Engineering Innovation and Research, 6*(3). [CrossRef]

Baltazar, J., & De Campos, J. a. C. F. (2019). Potential flow modelling of ducted propellers with blunt trailing edge duct using a panel method. *ResearchGate*. https://www.researchgate.net/publication/349253122_Potential_Flow_Modelling_of_Ducted_Propellers_with_Blunt_Trailing_Edge_Duct_Using_a_Panel_Method.

Bhattacharyya, A., Neitzel, J. C., Steen, S., & Krasilnikov, V. (2015). Influence of flow transition on open and ducted propeller characteristics. *ResearchGate*. https://www.researchgate.net/publication/346880301_Influence_of_Flow_Transition_on_Open_and_Ducted_Propeller_Characteristics.

Bhattacharyya, A., Krasilnikov, V. I., & Steen, S. (2016). Scale effects on open water characteristics of a controllable pitch propeller working within different duct designs. *Ocean Engineering, 112*, 226–242. [CrossRef]

Bhattacharyya, A., Krasilnikov, V., & Steen, S. (2016b). A CFD-based scaling approach for ducted propellers. *Ocean Engineering, 123*, 116–130. [CrossRef]

Caldas, A., Meis, M., & Sarasquete, A. (2010). CFD validation of different propeller ducts on Open Water condition. In *13th Numerical Towing Tank Symposium*, Germany.

Celik, F., Dogrul, A., Arıkan, Y., (2011). Investigation of the optimum duct Geometry for A Passenger ferry. In: *Proceedings of the 9th Symposium on High-Speed Marine Vehicles*.

Celik, F., Guner, M., & Ekinci, S. (2010). An approach to the design of ducted propeller. *ScientaIranica Transaction B: Mechanical Engineering, 17*(5), 406–417.

Celik, I. B., Ghia, U., Roache, P. J., & Freitas, C. J. (2008). Procedure for estimation and reporting of uncertainty due to discretization in CFD applications. *Journal of Fluids Engineering-transactions of the Asme, 130*(7), Article 078001. [CrossRef]

Cosner, R., Oberkampf, B., Rumsey, C., Rahaim, C., & Shih, T. (2006). AIAA Committee on standards for computational fluid dynamics: status and plans. *44th AIAA Aerospace Sciences Meeting and Exhibit*. [CrossRef]

Elbatran, A. H., Kotb, M. A., Hassan, A. A., Ahmed, M. W. A. E., & Banawan, A. A. (2014). Stationary and low speed performance characteristics of open and ducted CPPs. *ResearchGate*. https://www.researchgate.net/publication/301777898_Stationary_and_Low_Speed_Performance_Characteristics_of_Open_and_Ducted_CPPs.

Funeno, I., Pouw, C., & Bosman, R. (2013). Measurements and computations for blade spindle torque of controllable pitch propellers in open water. In *Proceedings of the Third International Symposium on Marine Propulsors (SMP;Vol. 13)*.

Godjevac, M., Van Beek, T., Grimmelius, H. T., Tinga, T., & Stapersma, D. (2009). Prediction of fretting motion in a controllable pitch propeller during service. *Proceedings of the Institution of Mechanical Engineers, Part M: Journal of Engineering for the Maritime Environment, 223*(4), 541–560. [CrossRef]

Gong, J., Ding, J., & Wang, L. (2021). Propeller–duct interaction on the wake dynamics of a ducted propeller. *Physics of Fluids, 33*(7), Article 074102. [CrossRef]

Haimov, H., Vicario, J., & Del Corral, J. (2011). RANSE code application for ducted and endplate propellers in open water. In *Proceedings of the Second International Symposium on Marine Propulsors (pp. 1–9)*.

Heinke, H. J. (2011). Potsdam Propeller Test Case (PPTC), Open Water Tests with the Model Propeller, VP1304, *Second International Symposium on Marine Propulsors smp'11, Hamburg, Germany*, Report 3753.

Huisman, J., Garenaux, M., de Jager, A., & Janse, G. (2022). Validation of Cavitation Prediction of Ducted Propeller Design and Analysis Tools. *Seventh International Symposium on Marine Propulsors (SMP'22), Wuxi, China*.

International Towing Tank Conference. (1999). Recommended Procedures and Guidelines-CFD, General CFD Verification. *International Towing Tank Conference* https://www.ittc.info/media/8153/75-03-01-01.pdf.

Kajitani, H., Miyata, H., Ikehata, M., Tanaka, H., Adachi, H., Namimatsu, M., Ogiwara, S. (1983). *The Summary of the Cooperative Experiment on Wigley Parabolic Model in Japan the Executive Members 4 I*. https://apps.dtic.mil/sti/tr/pdf/ADP003037.pdf.

Jessup, S. (2009). *Measurements of controllable pitch propeller blade loads under cavitating conditions*. https://www.semanticscholar.org/paper/Measurements-of-Controllable-Pitch-Propeller-Blade-Jessup-Donnelly/b0ee4866632d2428b4d33c8ee166c8f852328737.

Kim, K. W., Paik, K. J., Lee, J. H., Song, S. S., Atlar, M., & Demirel, Y. K. (2021). A study on the efficient numerical analysis for the prediction of full-scale propeller performance using CFD. *Ocean Engineering, 240*, Article 109931. [CrossRef]

Kim, S., & Kinnas, S. A. (2022). A panel method for the prediction of unsteady performance of ducted propellers in ship behind condition. *Ocean Engineering, 246*, Article 110582. [CrossRef]

Liu, A., Dang, J., Xie, Q., & Hu, J. (2015). The effect of sheet cavitation on the blade spindle torque of a controllable pitch propeller. In *4th International Symposium on Marine Propulsors*.

Liu, X. L., & Wang, G. Q. (2006). A potential based panel method for prediction of steady performance of ducted propeller. *Journal of Ship Mechanics, 10*(6), 26–35.

Martelli, M., Figari, M., Altosole, M., & Vignolo, S. (2014). Controllable pitch propeller actuating mechanism, modelling and simulation. *Proceedings of the Institution of Mechanical Engineers, Part M: Journal of Engineering for the Maritime Environment, 228*(1), 29–43. [CrossRef]

Oosterveld, M. W. C. (1972). Ducted propeller systems suitable for tugs and pushboats. *International Shipbuilding Progress, 19*(219), 351–371. [CrossRef]

Pourmostafa, M., & Ghadimi, P. (2020). Applying boundary element method to simulate a high-skew Controllable Pitch Propeller with different hub diameters for preliminary design purposes. *Cogent Engineering, 7*(1), Article 1805857. [CrossRef]

Roache, P. J. (1994). Perspective: a method for uniform reporting of grid refinement studies. *Journal of Fluids Engineering-transactions of the Asme, 116*(3), 405–413. [CrossRef]

Siemens, DISW. (2021). *Star CCM+ Version 2020.3. User guide*. n.d. https://community.sw.siemens.com/s/question/0D54O000061xpUOSAY/simcenter-starccm-user-guide-tutorials-knowledge-base-and-tech-support

Tarbiat, S., Ghassemi, H., & Fadavie, M. (2014). Numerical prediction of hydromechanical behaviour of controllable pitch propeller. *International Journal of Rotating Machinery, 2014*, Article 180725. [CrossRef]

Yurtseven, A., & Aktay, K. (2023). The numerical investigation of spindle torque for a controllable pitch propeller in feathering maneuver. *Brodogradnja: Teorija I praksa brodogradnje I pomorske tehnike, 74*(2), 95–108. [CrossRef]

Zhang, Q., & Jaiman, R. K. (2019). Numerical analysis on the wake dynamics of a ducted propeller. *Ocean Engineering, 171*, 202–224. [CrossRef]

Zhang, Q., Jaiman, R. K., Ma, P., & Liu, J. (2020). Investigation on the performance of a ducted propeller in oblique flow. *Journal of Offshore Mechanics and Arctic Engineering, 142*(1), Article 011801. [CrossRef]

Zhang, T., &Barakos, G. N. (2021). High-fidelity numerical analysis and optimisation of ducted propeller aerodynamics and acoustics. *Aerospace Sci Technol 113*, Article 106708. [CrossRef]

Seatific, Vol. 3, Issue. 2, pp. 51–70, December 2023

Seatific Journal
https://seatific.yildiz.edu.tr
DOI: https://doi.org/10.14744/seatific.2023.0007

Research Article

A domestic waste heat recovery system: Mathematical model of a green kitchen module

Stefano Maria SPAGOCCI*

SMS Consulting, Cinisello Balsamo (MI), Italy

ARTICLE INFO

Article history
Received: March 20, 2023
Revised: July 27, 2023
Accepted: September 11, 2023

Key words:
Appliances; energy saving; phase change materials; sensible heat materials

ABSTRACT

A lumped parameter model of a domestic heat storage/recovery system is described. This is a typical green kitchen application, where the heat dissipated by kitchen appliances is stored in suitable materials by temperature rise and/or phase transitions. To this aim, sensible heat materials and phase change materials are considered. Based on the model, a number of design solutions are proposed, making use of fixed beds or shell-and-tube heat exchangers, where heat is stored in spheres or cylinders made up of (or encapsulating) suitable materials. The best solution (a PCM-based shell-and-tube exchanger) corresponds to ~50×50×25 cm, ~30 kg modules.

Cite this article as: Spagocci SM. A domestic waste heat recovery system: Mathematical model of a green kitchen module. Seatific 2023;3:2:51–70.

1. INTRODUCTION

The present environmental concerns, and the fact that the conventional energy sources are bound to be exhausted, make the search of alternative energy sources more urgent than ever. Energy saving is a form of alternative energy; in this context, waste heat recovery becomes particularly important. To appreciate the importance of this form of energy saving, one can consider the fact that in the UK alone 40 TWh per year could come from waste heat recovery in the industrial sector [MOXOFF, 2012a]. In this paper, the results obtained in a design study of heat storage/recovery systems (aimed at green kitchen applications) are described, together with the model employed to achieve them. In the green kitchen approach [MOXOFF, 2013a - Mukherjee, 2011], the thermal energy dissipated by various kitchen appliances is recovered by various means, typically for the production of hot water for domestic use.

There are various forms of waste heat recovery [Hussam et al., 2018]: regenerative and recuperative burners [Institute for Industrial Productivity, 2017 - BDF Industries, 2017] capture the waste heat from the combustion of hot flue gases, economizers [Thermtech, 2014] recover waste heat to be used for heating liquids, waste heat boilers [Ganapathy, 2015] are suitable to recover heat from exhaust gases and mainly used to produce steam for power generation, air preheaters [Yodrak et al., 2010] are employed for exhaust heat recovery. Heat exchangers [IPIECA, 2022] and heat pipes [JHCSS, 2017] are employed in such devices. The recovered heat can be employed to preheat the gases entering burners and/or furnaces, to produce electricity by steam or thermoelectric generators. In green kitchen applications the recovered waste heat comes from domestic appliances.

To have an idea of the potentialities of such technologies, one can consider the fact that savings of the order of 5-10% can be achieved by preheating gases in burners [Spirax Sarco, 2011], producing steam via a Rankine cycle can reach an efficiency of 22% [Stefanou, 2017], thermoelectric generators have a 2-5% efficiency but through the use of nanotechnologies efficiencies greater than 15% can be achieved [Caillat et al., 1999].

***Corresponding author.**
*E-mail address: scimodsim@gmail.com, stefanspag@gmail.com

In regenerative burners, the heat coming from the hot flue gases is first stored in a heat exchange medium such as aluminum oxide, then recovered by heating the cold gas through contact with the medium: this is an example of the utility of sensible heat materials in waste heat recovery. Sensible heat materials [Sarbu et al., 2018] store heat by increasing their temperature; in phase change material [Sarbu et al., 2018 - Ahmed et al., 2018], energy is mainly stored in the form of latent heat, although there can also be a temperature increase. Among sensible heat materials one can cite water, rock, sand and steel. Phase change materials can be classified as organic (paraffins and non-paraffins), inorganic (salt hydrates, low melting point metals), eutectic mixtures. At present, the cheapest and more performant phase change materials are paraffins [Sarbu et al., 2018].

In this paper, the lumped-parameter model employed is first described. To the best of the author's knowledge, this model substantially innovates the existing literature. On the base of the developed model, a number of solutions are proposed. The focus is on a thermal bus, with a refrigerator, an induction cook-top and a domestic oven connected in series. Whirlpool Europe presented a patent application [Mukherjee, 2011] concerning a green kitchen heat storage/recovery system, based on a water tank as the storage medium. The use of cylindrical modules, with cylindrical or spherical storage modules, was only proposed as an ancillary system, improving the water tank performance. The system described here, whose feasibility study was commissioned by Whirlpool Europe, substantially improves the solution proposed in the patent. In the main body of the paper, the formulae needed for practical use are only given; a full treatment is in Annexes A1-A7.

2. PROBLEM SETTING

In Table 1, some typical sensible heat materials (SHMs) and phase change materials (PCMs) are illustrated. The table shows that the energy storage density for PCMs is up to ~10 times larger than for SHMs. For appliance temperatures <50°C, the module charging process has to stop before the onset of fusion. In this case, PCMs only count for their specific heat. In this temperature range, SHMs may be more suitable than PCMs.

The first proposed approach is based on sensible heat materials [Dincer et al., 1997 - Sharma et al., 2005]. In this approach, the dissipated heat, carried by a fluid, heats the material. In the heat recovery phase, a cold fluid is put in touch with the material and heats up. If ρ_m is the material density, C its specific heat, ΔT the difference between the fluid and solid temperatures, then the material energy density is:

$$\rho_e=\rho_m \cdot C \cdot \Delta T \quad (1)$$

In Table 2, the thermophysical properties of typical SHMs are shown.

Phase change materials [Sharma et al., 2009] work similarly, except that most of the thermal energy is accumulated in the form of latent heat of fusion. During the phase transition, the material does not change its temperature. If ρ_m is the material density, ΔH the transition (fusion) enthalpy, the material energy density is:

$$\rho_e=\rho_m \cdot \Delta H \quad (2)$$

In Table 3, the thermophysical properties of common PCMs are shown.

In heat storage/recovery systems, the storage material is part of a heat exchanger so that, in the module charging phase, a hot thermo-vector fluid (heated by the thermal energy to recover) is able to transfer heat to the material. In the module discharging phase, a cold thermo-vector fluid gets heated, removing heat from the material.

In [MOXOFF, 2013a - Mukherjee, 2011], a possible design solution, based on a fixed bed (Fig. 1), was proposed. A fixed bed [Holdich, 2002] is a metal cylinder, filled with spheres of a suitable material and crossed by a thermo-vector fluid that exchanges heat with them. In the fixed bed regime, the viscous drag force does not prevail over gravity and the spheres are stuck in their position. Beyond the minimal fluidization velocity, the viscous drag force overcomes gravity and the spheres acquire a turbulent motion. One is then in the fluidized bed regime; the latter is unstable for spheres of diameter ≥1 cm [Holdich, 2002]. The diameter that had to be chosen falls in this range [MOXOFF, 2013b]; consequently, a fluidized bed solution was not considered.

In [MOXOFF, 2013a - Mukherjee, 2011] a possible design solution, based on a shell-and-tube heat exchanger [Mukherjee, 1998] (Fig. 2), was also proposed. Here it is only pointed out that the shell-and-tube heat exchanger has to be equipped with baffles, whose aim is described later. In [MOXOFF, 2013a], appliances are classified, according to their time behaviour, as discrete or continuous. As an example, one may consider a domestic oven and a refrigerator. Heat is recovered from a domestic oven when the appliance is turned off and its temperature is ~180-250°C [Zavattoni, 2012]. One then has a discrete process. A refrigerator, instead, dissipates energy continuously. A typical refrigerator is reported to dissipate 84 W at 40°C [Zavattoni, 2012].

Appliances can either dissipate at a nearly constant temperature (as in the case of a refrigerator or cook-top induction plane) or a variable temperature (as in the case of a domestic oven). The following module classification is then proposed:

- Constant Inlet Temperature Modules with SHMs (CITSHM),
- Constant Inlet Temperature Modules with PCMs (CITPCM),
- Variable Inlet Temperature Modules with SHMs (VITSHM),
- Variable Inlet Temperature Modules with PCMs (VITPCM).

Table 1. Heat storage characteristics of typical materials [Dincer, 1997 - Sharma et al., 2009]. ΔT = 15°C is assumed for sensible heat materials

Property	Rock	Water	Organic PCM	Inorganic PCM
Density (kg/m^3)	2240	1000	800	1600
Specific heat (kJ/kg.°K)	1.00	4.18	2.00	2.00
Latent heat (kJ/kg)	-	-	190	230
Mass per 10^6 J stored (kg)	67	16	5.30	4.35
Volume per 10^6 J stored (m^3)	30	16	6.60	2.70
Relative mass	15	4	1.25	1.00
Relative volume	11	6	2.50	1.00

PCM: Phase change materials

Table 2. Heat storage characteristics of typical sensible heat materials [Dincer, 1997 - Mardiana-Idayua et al., 2012]

Material	Water	Aluminum	Rock	Steatite	Steel
Density (kg/m^3)	1000	2700	2560	2680	7800
Specific heat (kJ/kg.°K)	4.18	0.90	0.96	1.07	0.57
Thermal conductivity (W/m.°K)	0.60	204	0.48	2.50	50

Table 3. Thermophysical properties of various phase change materials [Sharma et al., 2005 - Sharma et al., 2009]. The literature data are inconsistent and fragmentary. Where a parameter is available for only one phase, the value for the remaining phase was taken to coincide with the available value. Where a piece of data is missing for both phases, when possible, it was approximated with the average value for materials of the same category, when not possible, it was approximated with the typical values of Table 1. In the case of inconsistent data from different sources, the most pessimistic value was chosen. Materials with a transition temperature in the 20-100°C range were only considered. (l) = liquid state, (s) = solid state

Material	Fusion temperature (°C)	Fusion heat (kJ/kg)	Thermal conductivity (l) (W/m.°K)	Thermal conductivity (s) (W/m.°K)	Density (l) (kg/m^3)	Density (s) (kg/m^3)	Specific heat (l) (kJ/kg.°K)	Specific heat (s) (kJ/kg.°K)
Paraffin C16-C28	42	189.0	0.210	0.210	765	765	2.100	2.100
Paraffin C20-C33	48	189.0	0.210	0.210	769	769	2.100	2.100
N-Hexacosane	56	257.0	0.210	0.210	770	770	2.100	2.100
Paraffin C22-C45	58	189.0	0.210	0.210	795	795	2.100	2.100
Paraffin C23-C45	62	189.0	0.210	0.210	790	790	2.100	2.100
Paraffin wax	64	173.6	0.167	0.339	790	790	2.100	2.100
Paraffin C21-C50	66	189.0	0.210	0.210	830	830	2.100	2.100
Naphtalene	80	147.7	0.132	0.34	976	976	2.000	2.000
$Ba(OH)_2 . 8H_2O$	48	265.0	0.653	0.653	1937	1937	2.000	2.000
$Mg(NO_3)_2 . 6H_2O$	89	149.5	0.490	0.490	1550	1550	2.000	2.000
$Mg(NO_3)_2 . 6H_2O + NH_4NO_3$	52	125.5	0.494	0.494	1515	1515	2.000	2.000
Naphtalene + Benzoic acid	67	123.4	0.130	0.257	800	800	2.000	2.000
Lauric acid	42	178.0	0.147	0.147	870	870	1.600	1.600
Stearic acid	60	186.5	0.172	0.172	848	848	2.350	2.350
Palmitic acid	61	185.4	0.132	0.132	848	989	1.975	1.975
Neopentylglycol	48	139.0	0.360	0.360	1190	1190	2.760	2.760
Trimethylol ethane	82	174.0	0.510	0.510	1220	1220	2.750	2.00

3. MATHEMATICAL MODEL

3.1. System dimensioning

In order to be able to calculate the dimensions of the proposed heat storage/recovery systems, let us first introduce the energy size E_0, scaled by a factor f_d (whose aim is clarified in the following). The volume of material needed to achieve an energy size E_0 can then be calculated based on ρ_e, the storage density, Eq. (1) or (2). In particular, one has:

$$V_m = \frac{f_d \cdot E_0}{\rho_e} \quad (3)$$

Let us also introduce the porosity 1-ε_3, for a fixed bed and a shell-and-tube exchanger. In the former case, one has to use the result reported in the literature for the maximum

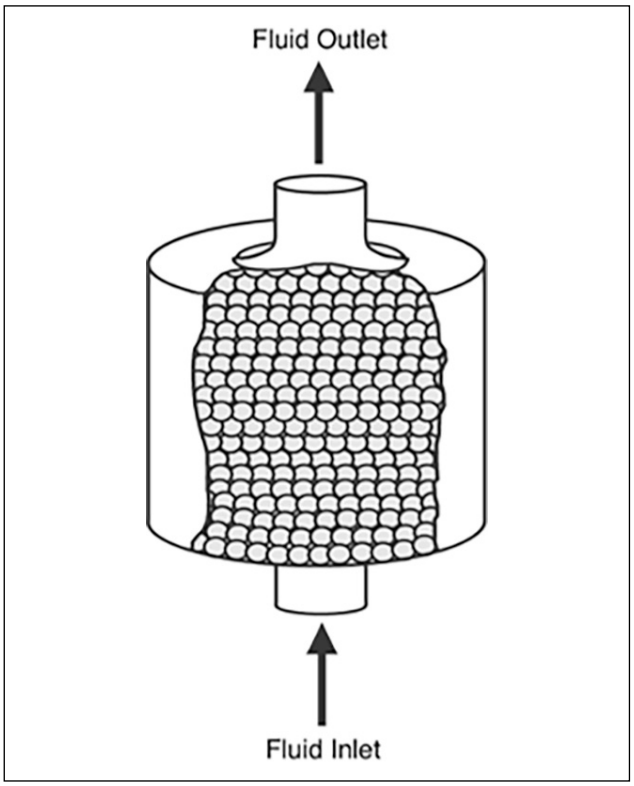

Figure 1. A heat storage/recovery module, based on a fixed bed. The spheres are filled with a phase change material (such as glycol) or made up of a sensible heat material (such as aluminium).

sphere packing density (face-centered cubic lattice [Hales et al., 2006]).

In particular, one has

$$\varepsilon_3 = \frac{\pi}{3\cdot\sqrt{2}} \approx 74\% \tag{4}$$

Provided this is economically feasible, spheres in the fixed bed could be packed according to Eq. (4), at least approximately. The random sphere packing density is instead ~64% [Song et al., 2008] so, cautiously, this figure was rather employed. For cylinder packing, ε_3 can be calculated analytically, under the hypothesis that each circle of radius ru is located at the center or edges of a square of size $4\cdot r_u$ and each cell contains two circles. One has to consider that, in shell-and-tube exchangers, an empirical rules states that for greater efficiency the tube pitch (minimum distance between the tubes) must be 1.25 times their diameter [Mukherjee, 1998]:

$$\varepsilon_3 = \frac{4\pi}{25} \approx 50\% \tag{5}$$

A porosity $1\text{-}\varepsilon_2$, characterizing the average velocity of the thermo-vector fluid in the fixed bed, can finally be defined and it turns out that:

$$\varepsilon_2 = \varepsilon_3 \tag{6}$$

as shown by the continuity equation [Sharma et al., 2005]. The module volume is then:

$$V_c = \frac{V_m}{\varepsilon_3} \tag{7}$$

Let us also define the shape factors a_c and a_u, for a cylindrical module of height h_c and the module or its storage units, respectively:

$$a_c = \frac{h_c}{r_c} \tag{8}$$

and:

$$a_u = \frac{h_c}{r_u} \tag{9}$$

One can then calculate N_u, the number of heat storage units, for spheres and cylinders. The calculation can be carried out by noticing that the total volume occupied by the storage units is given by $V_c\cdot\varepsilon_3$ and dividing this volume by the volume of a single storage unit. For spheres, one has:

$$N_u = \frac{\pi}{\sqrt{32}}\cdot\frac{a_u^3}{a_c^2} \tag{10}$$

for perfect packing (in the case of random packing, the coefficient is ~0.48). For cylinders:

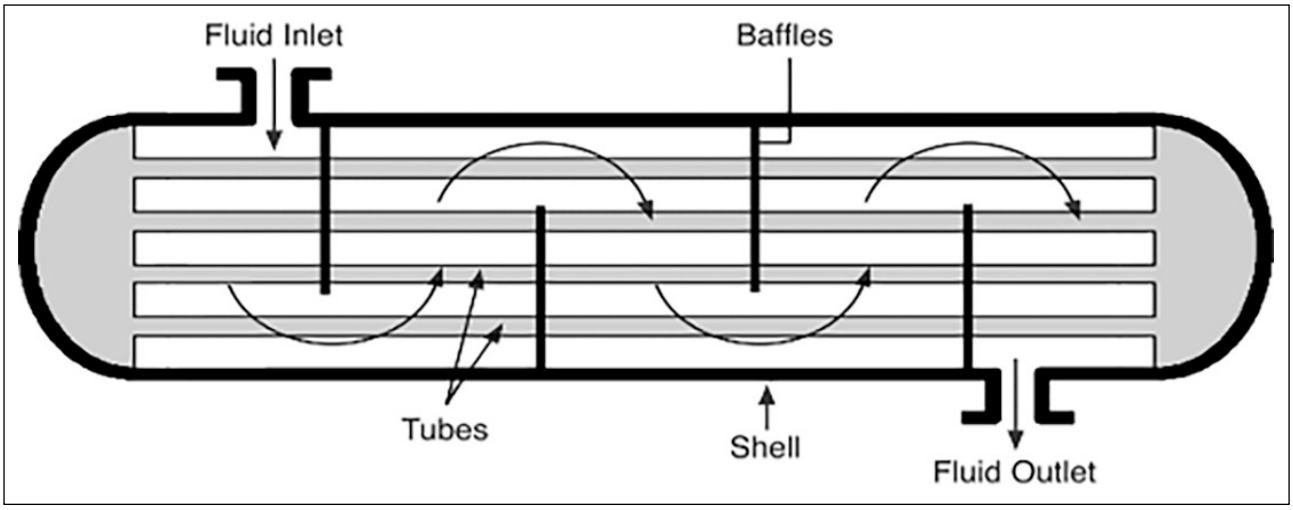

Figure 2. A heat storage/recovery module, based on a shell-and-tube heat exchanger. The spheres are filled with a phase change material (such as glycol) or made up of a sensible heat material (such as aluminium).

Table 4. The PCM-based fixed bed heat storage/recovery system. The system is made up of four thermally insulated modules. There are two parallel refrigerator modules, alternatively working in the charging and discharging mode. System diameter = 50 cm. Spherical heat storage unit diameter = 1 cm. Charging time = 18 min. Effective charge efficiency = 145%. Energy efficiency = 80%

	Compound	Height (cm)	Mass (kg)	Energy storage (MJ)	Air flow (l/s)	Number of units
Induction plane (18 min, 100 W @ 60°C)	Glycol	4.0	5.9	0.1	2.4	12633
Oven (18 min, 365 W @ 80°C)	Glycol	4.7	7.1	1.1	5.9	15220
Refrigerator (18 min, 84 W @ 40°C)	Glycol	2×3.9	2×5.9	2×0.1	2×4.0	2×12561
Total (549 W)		16.5	24.8	1.4	16.3	52975

Table 5. The PCM-based shell-and-tube heat storage/recovery system. The system is made up of four thermally insulated modules. There are two parallel refrigerator modules, alternatively working in the charging and discharging mode. System diameter = 50 cm. Cylindrical heat storage unit diameter = 0.5 cm. Charging time = 18 min. Effective charge efficiency = 122%. Energy efficiency = 76%

	Compound	Height (cm)	Mass (kg)	Energy storage (MJ)	Air flow (l/s)	Number of units
Induction plane (18 min, 100 W @ 60°C)	Glycol	5.7	6.7	0.1	2.4	5027
Oven (18 min, 365 W @ 80°C)	Glycol	5.6	6.6	1.1	5.9	5027
Refrigerator (18 min, 84 W @ 40°C)	Glycol	2×6.2	2×7.3	2×0.1	2×4.0	2×5027
Total (549 W)		23.9	27.9	1.4	16.3	20108

$$N_u = \frac{4\pi}{25} \cdot \frac{a_u^3}{a_c^2} \tag{11}$$

On the other hand, S_u, the total heat exchange area of the units, is easily determined by multiplying the exchange area of a storage unit by the number of units. For spheres:

$$S_u = \frac{\pi^2}{\sqrt{2}} \cdot a_u \cdot r_c^2 \tag{12}$$

and for cylinders:

$$S_u = \frac{8\pi^2}{25} \cdot \frac{a_u}{a_c} \cdot h_c \cdot r_c \tag{13}$$

For the best solutions, it was determined that $N_u \approx 20000$ (cylindrical storage modules) and $N_u \approx 50000$ (spherical storage modules). See Tables 4-7.

3.2. Thermal energy exchange

Let us then present the model devised for calculating the heat storage/recovery system features, which generalizes the results in [Bejan, 1978]. To this aim, let us first introduce the quantity:

$$\tau = \frac{M \cdot C}{\dot{m} \cdot C_p} \tag{14}$$

with dimensions of time, where M is the heat storage material mass, C its effective specific heat, $\dot{m}$ the mass flow rate of the thermo-vector fluid, C_p its specific heat. Let us then introduce θ (non-dimensional time) and y, given by:

$$\theta = \frac{t}{\tau} \tag{15}$$

$$y = 1 - exp(-NTU) \tag{16}$$

where NTU (the Number of Transfer Units) is a non-dimensional parameter, given by:

$$NTU = \frac{U \cdot S_u}{\dot{m} \cdot C_p} \tag{17}$$

In Eq. (17), U is the heat exchange coefficient. For our geometry and fluid, it turns out that NTU>>1. As a consequence of Eq. (16), one has y≈1. Also, in Annex A3 it is shown that NTU>>1 maximizes the system effectiveness. Therefore, this condition was imposed to our solutions. As for the temperature profile, one has:

$$T = T_\infty + (T_0 - T_\infty) \cdot exp(-\theta) + \Delta T(t) \tag{18}$$

with:

$$\Delta T(t) = exp(-\theta) \cdot \int_0^\theta ds \cdot exp(s) \cdot \Delta T_\infty(s) \tag{19}$$

$$\Delta T_\infty(t) = T_{in}(t) - T_\infty \tag{20}$$

In the previous equations:

- T is the material (fluid outlet) temperature,
- T_0 is the room temperature,
- $T_{in}(t)$ is the temperature of the thermo-vector fluid at the inlet,
- T_∞ is the asymptotic value of $T_{in}(t)$.

Let us observe that the material and, as explained, fluid outlet temperatures, for y≈1 are almost equal [Wall, 1977].

Table 6. The SHM-based fixed bed heat storage/recovery system. The system is made up of four thermally insulated modules. There are two parallel refrigerator modules, alternatively working in the charging and discharging mode. System diameter = 50 cm. Spherical heat storage unit diameter = 1 cm. Charging time = 18 min. Effective charge efficiency = 87%. Energy efficiency = 87%

	Compound	Height (cm)	Mass (kg)	Energy storage (MJ)	Air flow (l/s)	Number of units
Induction plane (18 min, 100 W @ 60°C)	Aluminium	5.5	18.2	0.1	2.4	17151
Oven (18 min, 365 W @ 80°C)	Aluminium	14.9	50.6	1.1	5.9	47763
Refrigerator (18 min, 84 W @ 40°C)	Aluminium	2×5.3	2×18.1	2×0.1	2×4.0	2×17053
Total (549 W)		31.0	105.0	1.4	16.3	99020

Table 7. The SHM-based shell-and-tube heat storage/recovery system. The system is made up of four thermally insulated modules. There are two parallel refrigerator modules, alternatively working in the charging and discharging mode. System diameter = 50 cm. Heat storage cylindrical unit diameter = 0.5 cm. Charging time = 18 min. Effective charge efficiency = 83%. Energy efficiency = 83%

	Compound	Height (cm)	Mass (kg)	Energy storage (MJ)	Air flow (l/s)	Number of units
Induction plane (18 min, 100 W @ 60 °C)	Aluminium	7.7	20.6	0.1	2.4	5027
Oven (18 min, 365 W @ 80 °C)	Aluminium	17.7	47.1	1.1	5.9	5027
Refrigerator (18 min, 84 W @ 40 °C)	Aluminium	2×8.5	2×22.6	2×0.1	2×4.0	2×5027
Total (549 W)		42.4	112.9	1.4	16.3	20108

T_∞ coincides with the appliance dissipation temperature, for constant temperature appliances. For variable temperature, it coincides with the asymptotic temperature of the fluid and the module. See Annexes for details.

As for the appliance temperatures, the relevant cases are both constant and exponentially decreasing dissipation temperatures [MOXOFF, 2013b]. In particular, the exponential law applies to convection oven cooling, where, as demonstrated in Annex A2, things work as if the oven dissipated at an effective and constant temperature. In all practically relevant cases, Eqs. (18) to (20) then reduce to [Bejan, 1978]:

$$T=T_\infty+(T_0-T_\infty)\cdot exp(-\theta) \quad (21)$$

where T describes both the fluid outlet and material temperature and T_∞, in the case of a domestic oven, must be interpreted as an effective temperature. Eq. (21) reveals that, for short charging times, both the outlet fluid and the material are at room temperature. Their temperature increases exponentially, until both reach the inlet fluid temperature. For long charging times, the heat transfer rate between the material and the fluid becomes negligible, since they approximately reach the same temperature.

By introducing the concept of exergy [Bjurström et al., 1985], defined as the maximum work that a system can do while reaching equilibrium with its environment, and exergetic efficiency, it is then possible to maximize the system exergetic efficiency (Annex A5) as a function of charge time. The thermodynamic optimization translates into an expression for T_{opt}, the optimal module charging temperature. In fact, such a temperature is approximately given by the geometric mean between the room and fluid inlet temperatures. In [Bjurström et al., 1985] it is stated that this geometric mean approximates the optimal charging temperature when the module temperature increase is negligible. As detailed in Annex A6, such an expression (at 5%) rather describes T_{opt} in the 20-100°C range, so that:

$$T_{opt}\approx\sqrt{T_0\cdot T_\infty} \quad (22)$$

Let us point out that, in the interval 20-100°C, the arithmetic and geometric means differ by ~1%. More accurately, in the 20-100°C range one has (Annex A6):

$$T_{opt}=0.64\cdot T_\infty+0.36\cdot T_0 \quad (23)$$

By inverting Eq. (23), one finds an expression for the system charging time:

$$T_{opt}=\frac{\tau}{f_d}\cdot log(\frac{T_\infty-T_0}{T_\infty-T_{opt}}) \quad (24)$$

where τ is given by Eq. (14), T_{opt} by Eq. (23) and the factor f_d was inserted. Let us notice that, by substituting Eq. (23) in Eq. (24), it is seen that $t_{opt}\approx\tau$ (provided f_d=1). For the optimal

configurations, then, θ≈1. As explained below, by over-dimensioning the module by the factor f_d, it is possible to achieve an apparent charging efficiency of more than 100%.

Since an infinitesimal fluid volume, entering the heat exchanger at T_∞ and transferring its thermal energy to the storage material, exits the system and suddenly reaches T_0 [Wall, 1977], it is possible to establish a relationship between the mass flow rate and the power transported by the fluid:

$$W=\dot{m}\cdot C_p\cdot(T_\infty-T_0) \tag{25}$$

This expression then allows to determine the volume throughput Φ, given W:

$$\Phi=\frac{W}{p_m\cdot C_p\cdot(T_\infty-T_0)} \tag{26}$$

Given Eq. (25) and:

$$E=M\cdot C\cdot(T_\infty-T_0) \tag{27}$$

(E=fd·E0) the system time constant, Eq. (16), can be re-written as:

$$\tau=\frac{E}{W} \tag{28}$$

From Eq. (24), then:

$$T_{opt}=\frac{E_0}{W}\cdot log(\frac{T_\infty-T_0}{T_\infty-T_{opt}}) \tag{29}$$

One also needs to calculate U, the thermal exchange coefficient. For fixed beds, the correlation in [Chauk et al., 1998] was employed:

$$N_u=\frac{U.(2.r_u)}{k_f}=1.80\cdot(Pr)^{1/3}\cdot(\mathrm{Re})^{1/2} \tag{30}$$

For the shell-and-tube exchangers [Fernandez et al., 2010]:

$$N_u=\frac{U.(2.r_u)}{k_f}=1.04\cdot(Pr)^{0.36}\cdot(\mathrm{Re})^{0.40} \tag{31}$$

In the previous equations, N_u is the Nusselt number, k_f the thermal conductivity of the fluid, Pr the Prandtl number [Dincer et al., 1997 - Fernandez et al., 2010]:

$$Pr=\frac{\mu_f\cdot C_p}{k_m} \tag{32}$$

where μ_f is the viscosity of the thermo-vector fluid, k_m is the thermal conductivity of the material and Re is the Reynolds number [Chauk et al., 1998 - Shah et al., 1998]:

$$\frac{\rho_m\cdot(1-\epsilon_3)\cdot(2\cdot r_u)\cdot v_f}{\mu_f} \tag{33}$$

where v_f is the thermo-vector fluid mean velocity. For Re>3000 one enters the turbulent regime [Shah et al., 1998]. In our case, Re<1200 [MOXOFF, 2012b]. The mean thermo-vector fluid velocity is:

$$v_f=\frac{\Phi}{f_p(1-\epsilon_2)\cdot\pi\cdot r_c^2} \tag{34}$$

where f_p is the ratio between baffle pitch and cylinder diameter (0.051, corresponding to a baffle pitch of 1 in and a cylinder diameter of 50 cm [MOXOFF, 2013b]).

In order to quantify the efficiency of green kitchen modules, let us introduce:

- the charge efficiency η_c, defined as the ratio between the stored energy and the maximum energy that could be stored in the system (its energy size E_0),
- the energetic efficiency η_e, defined as the ratio between the energy stored and the energy transported by the thermo-vector fluid.

As shown later, both indicators have to be considered, in order to quantify the system behaviour. In particular, one has:

$$\eta_c=\frac{M\cdot C\cdot(T-T_0)}{M\cdot C\cdot(T_\infty-T_0)}=1-\exp(-\theta) \tag{35}$$

$$\eta_e=\frac{M\cdot C\cdot(T-T_0)}{\mathrm{W}\cdot t}=\frac{\eta_c}{\theta}=\frac{1-\exp(-\theta)}{\theta} \tag{36}$$

Let us point out that ηc monotonically increases from 0 to 1, as t→∞. For finite charging times, then, η_c<1. In fact, ηc could be made ≈1, provided t→∞. In this case, however, η_e→0. In fact, η_e monotonically decreases from 1 to 0, as t→∞.

In the following, the model is applied to the previously classified module types. The reader may refer to the Annexes for details. As for model accuracy (Annex A3), one estimates a maximum temperature error of ~3%, with respect to their real space-time behaviour. As already noticed, the optimal charging time is t≈τ. For both continuous and discrete behaviour appliances, then, a charge and energetic efficiency of $1\text{-}e^{-1}$≈63% is predicted (provided the module is not over-dimensioned).

As shown in Annex A3, the model uses a number of approximations. Conditions on the Fourier (F_o≥0.04) and NTU (NTU≥3) numbers must then be satisfied. The above-mentioned conditions translate into each module having to be tall enough. In fact, see Eq. (A3.12), NTU is proportional to h_c. On the other hand, Eq. (A3.3), Fo is proportional to h_c-2. The coefficient in the F_o condition is two orders of magnitude lower than in the NTU condition and so, as verified, the former dominates. Given the module energy size (E_0) and base radius (r_c), the previously developed equations fix its height. The modules then have to be over-dimensioned by f_d, so as to make them tall enough and respect the F_o and NTU conditions.

4. MODULES

The charging process merely allows a limited charge efficiency. On the other hand, the choice of a factor f_d>1 increases efficiency. In fact, the energy accumulated into a module is given by $\eta_c\cdot E_0$. If one increases the energy size by making the module taller by a factor f_d, one can pretend to have the same energy size with an increased charge efficiency. As noticed above, in this paper it is assumed that $t_{opt}\approx\tau$. Therefore, see the comments to Eq. (24), one has $\theta=1/f_d+\theta_f$ where, as shown in Appendix A5, θ_f is the non-dimensional time taken by fusion to occur. The charging efficiency for a non-upscaled module must then be multiplied by fd, to give the effective charging efficiency.

Based on these facts, it is then possible to give expressions for the module efficiency. In particular, see Annex A4, an expression valid for all the previously defined module categories is:

$$\tilde{T}_\infty = T_\infty - k_1 \cdot (1 - e^{-1}) \cdot (T_\infty - T_0) \quad (37)$$

$$T = \tilde{T}_\infty + (T_0 - \tilde{T}_\infty) \cdot exp(-\theta) \quad (38)$$

$$\eta_c^{opt} = f_d \cdot (1 - k_2 \cdot exp(-\frac{1}{f_d})) \quad (39)$$

$$\eta_e^{opt} = f_d \cdot (1 - exp(-\frac{1}{f_d})) \quad (40)$$

In the previous equations, k1 is 0, unless for VITSHMs and VITPCMs, in which case it is 1. k_2 is 1, unless for CITPCMs and VITPCMs, in which case it is 1/2.

5. APPROXIMATIONS

In Annex A4, it is shown that the previous equations are approximations to the exact formulae. Using these approximate formulae, however, leads to a conservative design choice (to slightly overestimating module height, which can only increase thermal exchange efficiency, given the previously mentioned NTU conditions). Based on the results in Annex A3, the model is expected to reproduce the experimental results within ~3%. In Annex A4, it is equally shown that, for VITSHMs and VITPCMs, the efficiency expressions should be multiplied by correction factors ~1, ignoring which leads to slightly overestimating module height, with beneficial effects on thermal exchange efficiency.

The expression for the PCM module charging time, in principle, should be modified by adding the fusion time to the set 18 min. On the other hand, Table 3 shows that the fusion heats of interest are <514 MJ/m^3. Furthermore, Tables 4-7 show that transferred power is larger than 84·0.8=67 W. The storage units have 5 mm diameter and height <20 cm. A fusion process duration <30 sec, therefore negligible, is then calculated.

6. RESULTS

The mathematical model was simulated by an Excel spreadsheet. Using the model developed here, optimal configurations for both fixed beds and shell-and-tube heat exchangers, loaded with spherical or cylindrical heat storage units (made up of suitable heat storage materials), were calculated. The storage modules have an energy size of 1.4 MJ, approximately corresponding to the energy needed for heating water in a dish-washer cycle [MOXOFF, 2013a]. As for the thermo-vector fluid, air, with a maximum flow rate of 6 l/s per module, was chosen, as determined by structural and acoustical considerations (water would require lower flows, which would not pass through the heat exchanger [Zavattoni et al., 2014].

A domestic kitchen heat storage module was considered, coupled to a thermal bus that connects a refrigerator, an induction cook-top plane and a domestic oven. For the refrigerator, one must have two parallel heat storage modules [Mukherjee et al., 2011], since while one module is charging, the other is in the discharge phase. For discrete behaviour appliances, instead, a single module suffices. The cook-top induction plane charge time is ~18 min [Zavattoni et al., 2014]. The domestic oven charge time can be determined at will (within technological limits) by choosing a suitable air extraction pump. In the case of a refrigerator, the charge time depends on how much energy must be accumulated. Envisaging possible synchronization among the appliances, a common charge time of 18 min was then chosen [MOXOFF, 2012a - MOXOFF, 2013b]. The appliances considered were:

- A refrigerator, dissipation temperature: 40°C, dissipated power: 84 W, charging time: 18 min, stored energy: 0.1 MJ, air flow rate: 4.0 l/s.
- An induction cook plane, dissipation temperature: 60°C, dissipated power: 100 W, charging time: 18 min, stored energy: 0.1 MJ, air flow rate: 2.4 l/s.
- An oven, equivalent dissipation temperature: 80°C, real dissipation temperature range (as time proceeds): 20-100°C, charging time: 18 min, stored energy: 1.1 MJ, dissipated power: 365 W, air flow rate: 5.9 l/s.

In Tables 4-7, results for cylindrical modules with 50 cm diameter are shown. As for efficiencies and volume, the smallest factor needed for satisfying model approximations was chosen and efficiencies were calculated accordingly (and turned out to be ~80-150%, since the effective efficiency, due to the way it is defined, can be >100%). In order to rank the various solutions, a figure of merit, the power density (up to ~200 W/kg), was devised:

$$\rho_p = \frac{E \cdot \eta_c}{\rho_m \cdot V_m \cdot t_{opt}} \quad (41)$$

As for shell-and-tube heat exchangers, the following solutions were found:

- ~50×50×25 cm, ~30 kg (PCMs),
- ~50×50×40 cm, ~110 kg (SHMs).

On the other hand, fixed beds turned out to be ~30% shorter and ~10% lighter. Since module height is not critical, and fixed beds are harder and more expensive to build, the choice of election is PCM-based shell-and-tube heat exchangers.

7. DISCUSSION

As shown in Annex A3, a maximum error of ~3% is predicted, with respect to the real temperature behaviour of the system. A priori, one might worry about pressure drop in the heat exchangers. However (Annex A7), the maximum pressure drop is <0.5% of the atmospheric pressure and can then be neglected. Let us finally notice that both the fixed bed and the shell-and-tube exchanger have to be equipped with baffles. Baffles have different functions [Mukherjee, 1998]: they contribute to the structural stability, drive the flow by avoiding blind corners, make the flow orthogonal to the axis, improving the heat exchange rate. Simulation results imposed to devise a mechanism for increasing the mean area velocity, so as to increase the system NTUs. Baffles turned out to be the answer.

The model described here was conceived in order to fulfill the request, by Whirlpool Europe, to dimension a green kitchen system for which, to the best of the author's knowledge, no model existed in the literature. Experimental tests were

performed by Whirlpool Europe [Zavattoni et al., 2014] but no details were released in the open literature. Our exercise was meant to obtain a proof-of-concept, so that Whirlpool might decide whether to build and experiment a prototype. To the best of our knowledge, however, no prototype was built, therefore our model, although its approximations were demonstrated to be reasonable, was not validated experimentally.

8. CONCLUSION

The model is based on a lumped parameter approach, which makes it sufficiently simple and manageable. As previously stated, and shown in Appendix A3, a maximum error of ~3% is predicted, with respect to the real behaviour of the system. The model, however, could not be validated experimentally. Unfortunately, not all the possible heat storage materials could be considered, due to inconsistencies in literature data. However, ~20 SHMs and PCMs were considered, representing all the available material typologies. We acknowledge the existence of thermoplastic materials [Oguzhan et al., 2019], for which, however, we could not find useful data.

Our simulations allowed us to find a PCM-based and a SHM-based configuration, satisfying our specifications with the largest exergetic efficiency, namely ~50x50x25 cm, ~30 kg (PCM) and ~50x50x40 cm, ~110 kg (SHM). The PCM-based module is more compact and less heavy, so we tend to prefer it. Starting from the results achieved, future work might involve numerical optimization of the best configurations, using CFD software. Needless to say, the model would need experimental validation, which at the moment is lacking. In any case, the efficiencies calculated with a lumped parameter model are a lower estimate of those calculated with a 2D model [Taylor et al., 1991a - Taylor et al., 1991b]; the model, consequently, produces a conservative design. An interesting development might be an extension of the model to restaurant or industrial kitchens, especially in connection with a financial analysis.

NOMENCLATURE

ρ_m : *Material density (kg.m^{-3})*
C : *Material specific heat (J.K^{-1}.kg^{-1})*
ΔT : *Fluid minus solid temperature (K)*
ρ_e : *Material energy density (J.m^{-3})*
ΔH : *Material fusion enthalpy (J)*
V_m : *Material volume (m^3)*
E_0 : *Module energy size (J)*
f_d : *Module volume factor (n.d.)*
ε_3 : *1-ε3 is 3D porosity (n.d.)*
ε_2 : *1-ε2 is 2D porosity (n.d.)*
V_c : *Module volume (m^3)*
h_c : *Module height (m)*
a_c : *Module shape factor (n.d.)*
a_u : *Module unit shape factor (n.d.)*
r_c : *Module radius (m)*
r_u : *Module unit radius (m)*
N_u : *Total number of units (n.d.)*
S_u : *Total heat exchange area (m^2)*
M : *Material mass (kg)*
$\dot{m}$: *Fluid mass flow rate (kg.s^{-1})*
C_p : *Fluid specific heat (J.K-1.kg-1)*
θ : *Non-dimensional time (n.d.)*
NTU : *Number of Thermal Units (n.d.)*
y : *NTU-derived non-dimensional parameter (n.d.)*
U : *Heat exchange coefficient (W.m^{-2}.K^{-1})*
T_0 : *Room temperature (K)*
T_{in} : *Inlet fluid temperature (K)*
T_∞ : *Asymptotic value of T_{in} (K)*
T_{opt} : *Optimal module charging temperature (K)*
t_{opt} : *Optimal module charging time (s)*
W : *Power transported by the fluid (W)*
Φ : *Fluid volume throughput (m^3.s^{-1})*
E : *Energy deposed in the material (J)*
Nu : *Nusselt number (n.d.)*
Pr : *Prandtl number (n.d.)*
Re : *Reynolds number (n.d.)*
k_f : *Fluid thermal conductivity (W.m^{-1}.K^{-1})*
k_m : *Material thermal conductivity (W.m^{-1}.K^{-1})*
μ_f : *Fluid viscosity (N.s.m^{-2})*
v_f : *Fluid mean velocity (m/s)*
f_p : *Baffle pitch over heat module diameter (n.d.)*
η_c : *Module charging efficiency (n.d.)*
η_e : *Module energetic efficiency (n.d.)*
η_c^{opt} : *Optimum module charging efficiency (n.d.)*
η_e^{opt} : *Optimum module energetic efficiency (n.d.)*
ρ_p : *Module power density (J.m^{-3})*
t : *Time coordinate (s)*
F_o : *Fourier number (n.d.)*
f_e : *Module energetic efficiency correction factor (n.d.)*
f_c : *Module charging efficiency correction factor (n.d.)*
W_{ex} : *Power exchanged between material and fluid (W)*
$LMTD$: *Log Mean Temperature Difference (K)*
S : *Heat exchange area (m^2)*
T_f : *Fluid outlet temperature (K)*
T_s : *Solid material temperature (K)*
W_f : *Heat exchanged between material and fluid (J)*
W_s : *Power exchanged between material and fluid (J)*
P : *Heat exchanger wetted perimeter (m)*
x : *Distance coordinate (m)*
λ : *Spatial temperature decay constant (m)*
$\tilde{T}_\infty$: *Effective oven dissipation temperature (K)*

t_c : Module charging time (s)
dm : Infinitesimal mass entering the oven (kg)
σ : Oven thermal disturbance standard deviation (m)
α_p : Air thermal diffusivity ($m2.s^{-1}$)
l_o : Oven characteristic length (m)
t_o : Oven thermal disturbance characteristic time (s)
Bi : Biot number (n.d.)
α_m : Material thermal diffusivity ($m^2.s^{-1}$)
t_u : Module unit heat diffusion time scale (s)
τ_u : Module unit thermal equilibrium time scale (s)
KR : Ratio between material and fluid thermal conductivities (n.d.)
ε_{fit} : Error due to temperature fitted by an exponential (K)
ε_{nct} : Error due to non-constant temperature (K)
ε_{dyn} : Error due to material lagging behind fluid (K)
ε : Total temperature error (K)
ΔT_m : Temperature drop across the material (K)
T_f : Material fusion temperature (K)
θ_f : Material fusion duration (τ depending on C_l) (s)
$\theta^{(l)}_f$: Material fusion ending time (τ depending on C_l) (s)
$\theta^{(s)}_f$: Material fusion ending time (τ depending on C_s) (s)
C_s : Material solid specific heat ($J.K^{-1}.kg^{-1}$)
C_l : Material liquid specific heat (J.K-1.kg-1)
C_a : Material average specific heat ($J.K^{-1}.kg^{-1}$)
C_f : Material fusion specific heat ($J.K^{-1}.kg^{-1}$)
C_t : Material total specific heat ($J.K^{-1}.kg^{-1}$)
ξ_s : Material solid non-dimensional specific heat (n.d.)
ξ_l : Material liquid non-dimensional specific heat (n.d.)
ξ_a : Material average non-dimensional specific heat (n.d.)
ξ_f material fusion non-dimensional specific heat (n.d.)
ξ_t : Material total non-dimensional specific heat (n.d.)
θ^{opt} : Optimum module charging time (τ depending on C_l) (s)
E : System exergy (J)
U : System internal energy (J)
p_0 : Environmental pressure (Pa)
V : System volume (m^3)
S system entropy ($J.K^{-1}$)
W : Work performed by the system (J)
ΔS_{tot} : System plus environment entropy variation (J.K-1)
W_{dis} : Dissipated work (J)
η_{ex} : Exergetic efficiency (n.d.)
W_{max} : Maximum work performed by the system (J)
τ_∞ : A non-dimensional temperature (n.d.)
$<\theta_{opt}>$: Average value of θ_{opt} (s)
α : A function of $<\theta_{opt}>$ (n.d.)
T_c : Temperature at which the modulus charges (K)
θ_c : Non-dimensional Tc (τ depending on C_l) (n.d.)
Δp_{fb} : Fluidized bed pressure drop (Pa)
d_u : Module unit diameter (m)
Δp_{hh} : Heat exchanger pressure drop (Pa)
N_b : Number of heat exchanger baffles (n.d.)
$\tilde{N}_r$: Effective number of heat exchanger tube rows (n.d.)
f : Friction factor (n.d.)
d_c : Module diameter (m)
v_{mf} : Minimal fluidization velocity ($m.s^{-1}$)
g : Gravitational acceleration ($m.s^{-2}$)

ACKNOWLEDGEMENTS

I express my gratitude to dr. Paolo Ferrandi, dr. Chiara Riccobene and dr. Matteo Longoni (MOXOFF) for their invaluable help. My gratitude, also, to prof. Alfio Quarteroni (Politecnico di Milano) and dr. Ottavio Crivaro (MOXOFF) for their constant encouragement and for allowing and supporting the publication of this paper. I also gratefully acknowledge the contribution of dr. John Doyle (Whirlpool Europe).

DATA AVAILABILITY STATEMENT

The published publication includes all graphics and data collected or developed during the study.

CONFLICT OF INTEREST

The author declared no potential conflicts of interest with respect to the research, authorship, and/or publication of this article.

ETHICS

There are no ethical issues with the publication of this manuscript.

FINANCIAL DISCLOSURE

The authors declared that this study has received no financial support.

REFERENCES

Ahmed, A., & Lebedev, V.A. (2018). Thermal energy storage by using latent heat storage materials. *International Journal of Scientific & Engineering Research, 9*(5), 1442–1447.

BDF Industries (2017). *Regenerative and Recuperative Furnace*. www.bdfindustriesgroup.com/products/melting-furnace-rigen.

Bejan, A. (1978). Two thermodynamic optima in the design of sensible heat units for energy storage. *ASME Journal of Heat Transfer, 100*(4), 708–712. [CrossRef]

Biyikoglu, A. (2002). Optimization of a sensible heat cascade energy storage by lumped model. *Energy Conversion and Management, 43*(5), 617–637. [CrossRef]

Bjurström, H., & Carlsson, B. (1985). An exergy analysis of sensible and latent heat storage. *Heat Recovery Systems, 5*(3), 233–250. [CrossRef]

Caillat, T., Fleurial, J.- P., Snyder, G. J., Zoltan, A., Zoltan, D., & Borshchevsky, A. (1999). A new high efficiency segmented thermoelectric unicouple.

34th Intersociety Energy Conversion Engineering Conference, 2567–2570. [CrossRef]

Carvill, J. (2003). *Mechanical Engineer's Data Handbook*. Butterworth Heinemann.

Chauk, S. S., & Fan, L. S. (1998). Heat Transfer in Packed and Fluidized Beds. In: Rohsenow, W.M., Hartnett, J.R., & Cho, Y.I. (Eds.), *Handbook of Heat Transfer* (pp. 13.1-13.45). McGraw-Hill.

Dincer, I., & Cengel, Y. A. (2001). Energy, entropy and exergy concepts and their roles in thermal engineering. *Entropy, 3*(3), 116–149. [CrossRef]

Dincer, I., Dost, S., & Li, X. (1997). Performance analysis of sensible heat storage systems for thermal applications. *International Journal of Energy Research, 21*(12), 1157–1171. [CrossRef]

Fernandez, A. I., Martínez M., Segarra M., Martorell I., & Cabeza L. F. (2010). Selection of materials with potential in sensible thermal energy storage. *Solar Energy Materials and Solar Cells, 94*(10), 1723–1729. [CrossRef]

Ganapathy, V. (2015). *Steam Generators and Waste Heat Boilers for Process and Plant Engineers*. www.brazedplate.com. [CrossRef]

Hales, T. C., & Ferguson, S. P. (2006). A formulation of the Kepler conjecture. *Discrete & Computational Geometry, 36*(1), 21–69. [CrossRef]

Holdich, R. G. (2002). *Fundamentals of particle technology*. Midland Information Technology and Publishing.

Hussam, J., Khordehgah, N., Almahmoud, S., Delpech, B., Chauhan, A., & Tassou, S. A. (2018). Waste heat recovery technologies and applications. *Thermal Science and Engineering Progress, 6*, 268–289. [CrossRef]

Institute for Industrial Productivity (2017). *Regenerative Burners for Reheating Furnaces*. www.ietd.iipnetwork.org/content/regenerative-burners-reheating-furnaces.

IPIECA (2022). *Heat Exchangers*. www.ipieca.org/resources/energy-efficiency-solutions/heat-exchangers-2022.

JHCSS (2017). *Heat Pipes*. www.jhcss.com.au/products-1/thermal-management/heat-pipes-heat-exchangers.

Mardiana-Idayua, A., & Riffat, S. B. (2012). Review on heat recovery technologies for building applications. *Renewable and Sustainable Energy Reviews, 16*(2), 1241–1255. [CrossRef]

Mehrer, A., & Stolwijk, A. (2009). Heroes and Highlights in the History of Diffusion. *Diffusion Fundamentals*, 11(1), 1–32.

MOXOFF (2012a). *Accumulo delle potenze perse: studio delle tecnologie adatte a un immagazzinamento delle potenze dagli elettrodomestici* [unpublished technical report 4.1.3]. MOXOFF.

MOXOFF (2012b). *Accumulo termico: evidenza del suo funzionamento attraverso la modellizzazione e la prototipazione virtuale* [unpublished technical report 4.1.4]. MOXOFF.

MOXOFF (2013a). *Riutilizzo della potenza termica in eccesso: analisi di letteratura e selezione delle tecnologie più promettenti* [unpublished technical report 4.1.5]. MOXOFF.

MOXOFF (2013b). *Riutilizzo della potenza termica in eccesso: selezione del sistema migliore e analisi dell'efficienza* [unpublished technical report 4.1.6]. MOXOFF.

Mukherjee, R. (1998). Effectively design shell-and-tube heat exchangers. *Chemical Engineering Progress, 94*(2), 21–37.

Mukherjee, R., Singh, D., Grewal, R., Ranjan, S., Olivani, A., Alshourbagy, M., & Pannock, J. (2011). *Assembly of domestic appliances with a system for utilizing waste heat from refrigerator in a washing appliance* [unpublished European patent application 11189489.5]. European Patent Office.

Oguzhan, D., Marengo, M., & Bertola, V. (2019). Thermal performance of pulsating heat stripes built with plastic materials. *Journal of Heat Transfer, 141*(9), 1–8. [CrossRef]

Rosen, M. A., Hooper, F.C., & Barbaris, L. N. (1988). Exergy analysis for the evaluation of the performance of closed thermal energy storage systems. *Journal of Solar Energy Engineering, 110*(4), 255–261. [CrossRef]

Sarbu, I., & Sebarchievici, C. (2018). A comprehensive review of thermal energy storage. *Sustainability, 10*(191), 1–32. [CrossRef]

Shah, R. K., & Sekulic, D. P. (1998). Heat Exchangers. In: Rohsenow, W.M., Hartnett, J.R., Cho, Y.I. (Eds.), *Handbook of Heat Transfer* (pp. 17.1–17.169), McGraw-Hill.

Sharma, A., Tyagi, V. V., Chen, C. R., & Buddhi, D. (2009). Review on thermal energy storage with phase change materials and applications. *Renewable and Sustainable Energy Reviews, 13*(2), 318–345. [CrossRef]

Sharma, S. D., & Sagara, K. (2005). Latent heat storage materials and systems: A review. *International Journal of Green Energy, 2*(1), 1–56. [CrossRef]

Song, C., Wang, P., & Makse, H. A. (2008). A phase diagram for jammed matter. *Nature, 453*(7195), 629–632. [CrossRef]

Spirax Sarco (2011). *Miscellaneous Boiler Types, Economizers and Superheaters*. www.spiraxsarco.com/learn-about-steam/the-boiler-house/miscellaneous-boiler-types-economisers-and-superheaters.

Stefanou, M. R. (2017). Performance evaluation of an ORC unit integrated to a waste heat recovery system in a steel mill. *IV International Seminar on ORC Power Systems*, 535–542. [CrossRef]

Taylor, M. J., Krane, R. J., & Parsons, J. R. (1991a). Second law optimization of a sensible heat thermal energy storage system with a distributed storage element - Part I. *ASME Journal of Energy Resources Technology, 113*(1), 20–26. [CrossRef]

Taylor, M. J., Krane, R. J., & Parsons, J. R. (1991b). Second law optimization of a sensible heat thermal energy storage system with a distributed storage element - Part II. *ASME Journal of Energy Resources Technology, 113*(1), 27–32. [CrossRef]

Thermtech (2014). *Reducing energy costs with economizers*, www.thermtech.co.uk/reducing-energy-costs-with-economisers.

Wall, G. (1977). *Exergy - A Useful Concept within Resource Accounting* [unpublished technical report 77-42]. Chalmers University of Technology.

Yodrak, L., Rittidech, S., Poomsa-ad, N., & Meena, P. (2010). Waste heat recovery by heat pipe air-preheater to energy thrift from the furnace in a hot forging process. *American Journal of Applied Sciences, 7*(5), 675–681.

Yovanovich, M.M. (1998). Conduction and Thermal Contact Resistances. In: Rohsenow, W.M., Hartnett, J.R., Cho, Y.I. (Eds.), *Handbook of Heat Transfer* (pp. 3.1–3.73), McGraw-Hill.

Zavattoni, S. (2012). *Household Appliances: Waste Heat Assessment and Thermal Energy Storage Options* [unpublished technical report]. SUPSI.

Zavattoni, S., Garcia-Polanco, N., Capablo, J., & Doyle, J. P. (2014). Packed bed latent heat TES for home appliance waste heat storage - System dimensioning and CFD analysis. *International Conference on Home Appliance Technologies*. Available from: www.iapp-greenkitchen.eu.

ANNEX A1
HEAT STORAGE SYSTEM MODEL

Let us generalize the model of a heat/storage recovery system to a time-variable inlet temperature profile. In particular, the analysis assumes that a hot fluid enters an insulated vessel, where it interacts with a sensible heat material (SHM), supposed to have constant temperature, and heats it. Thermal energy can then be stored. Let us then express W_{ex}, the power exchanged between the material and the thermo-vector fluid, by using the Log Mean Temperature Difference (LMTD) formalism [Bejan, 1978]:

$$W_{ex} = U \cdot S \cdot LMTD \tag{A1.1}$$

$$LTMD = \frac{T_{\text{in}}(t) - T_f}{log(\frac{T_{\text{in}}(t) - T_s}{T_f - T_s})} \tag{A1.2}$$

where U is the heat transfer coefficient, S is the heat exchange area, T_f is the fluid outlet temperature, T_{in} (t) is the fluid inlet temperature (supposed to be varying in time) and T_s is the solid temperature.

The exchanged power, as seen from the fluid side, is given by:

$$W_f = W_{\text{ex}} = \dot{m} \cdot C_p \cdot (T_{\text{in}} - T_f(t)) \tag{A1.3}$$

where $\dot{m}$ is the fluid flow rate, C_p is its specific heat. The exchanged power, as seen from the solid side, is given by:

$$W_s = W_{ex} = \frac{M \cdot C \cdot dT_s}{dt} \tag{A1.4}$$

where M is the solid mass, C the solid specific heat.

Combining Eqs. (A1.1)-(A1.3):

$$T_f = y \cdot T_s + (1 - y) \cdot T_{\text{in}}(t) \tag{A1.5}$$

where y is a parameter characterizing heat transfer in the system. As shown in Annex A3, y≈1 to any practical purpose.

In particular:

$$y = 1 - exp(-NTU) \tag{A1.6}$$

where the parameter NTU (Number of Transfer Units) is a non-dimensional number [Bejan, 1978]:

$$NTU = \frac{U \cdot S}{\dot{m} \cdot C_p} \tag{A1.7}$$

In Annex A3, it is shown that the condition NTU→∞ is imposed to the system, so that:

$$T_f = T_s \tag{A1.8}$$

By combining Eqs. (A1.3)-(A1.5), one has the following differential equation:

$$\frac{\tau}{y} \cdot \dot{T}_f = -T_f + T_{\text{in}}(t) + \tau \cdot (\frac{1}{y} - 1) \cdot \dot{T_{\text{in}}}(t) \tag{A1.9}$$

where τ is given by Eq. (A1.10) and T_{in} is variable in time (for physical reasons, at infinity it must flatten to T_∞). Both the inlet and outlet temperatures, at t=0, are supposed to be room temperature (T_0). Given these conditions, the solution of the differential equation is an exponential, with:

$$\tau = \frac{M \cdot C}{\dot{m} \cdot C_p} \tag{A1.10}$$

where the coefficients added to the exponential and multiplying it are functions of time:

$$T_f = T_\infty + (T_0 - T_\infty) \cdot exp(-y \cdot \theta) + \Delta T_f(t) \tag{A1.11}$$

$$\Delta T_f(t) = exp(-y \cdot \theta) \cdot \int_0^{y \cdot \theta} ds \cdot exp(s) \cdot (\Delta T_\infty(s) + \tau \cdot (\frac{1}{y} - 1) \cdot \dot{T}_{\text{in}}(s)) \tag{A1.12}$$

and:

$$\Delta T_\infty(t) = T_{\text{in}}(t) - T_\infty \tag{A1.13}$$

As for the solid, by combining Eqs. (A1.3) to (A1.5), one has:

$$\frac{\tau}{y} \cdot \dot{T}_s = -T_s + T_{\text{in}}(t) \tag{A1.14}$$

where the same fluid temperature hypotheses as above are assumed. In particular:

$$T_s = T_\infty + (T_0 - T_\infty) \cdot exp(-y \cdot \theta) + \Delta T_s(t) \tag{A1.15}$$

$$\Delta T_s(t) = exp(-y \cdot \theta) \cdot \int_0^{y \cdot \theta} ds \cdot exp(s) \cdot \Delta T_\infty(s) \tag{A1.16}$$

These solutions can be unified and simplified under hypothesis that NTU→∞:

$$T = T_\infty + (T_0 - T_\infty) \cdot exp(-\theta) + \Delta T(t) \tag{A1.17}$$

$$\Delta T(t) = exp(-\theta) \cdot \int_0^{\theta} ds \cdot exp(s) \cdot \Delta T_\infty(s) \tag{A1.18}$$

$$\Delta T_\infty(t) = T_{\text{in}}(t) - T_\infty \tag{A1.19}$$

In the previous equations, T is the common temperature to the outlet fluid and solid. Of special interest is the case NTU→∞ and $T_{in}(t)=T_\infty$ (constant inlet temperature):

$$T = T_\infty + (T_0 - T_\infty) \cdot exp(-\theta) \tag{A1.20}$$

For any practical purpose, the previous equation is applicable to all the systems described here. In the previous equations, the non-dimensional time is defined as:

$$\theta = \frac{t}{\tau} \tag{A1.21}$$

Finally, let us calculate the temperature distribution inside the exchanger:

$$dW_{ex} = U \cdot (T_f - T_s) \cdot P \cdot dx \tag{A1.22}$$

$$dW_f = dW_{ex} = -\dot{m} \cdot C_p \cdot \partial_x (T_f - T_s) \cdot dx \tag{A1.23}$$

where P is the wetted perimeter:

$$\partial_x (T_f - T_s) = -(T_f - T_s)/\lambda \tag{A1.24}$$

where h_c is the cylindrical module height. In the previous equation:

$$\lambda = \frac{h_c}{NTU} \tag{A1.25}$$

According to the boundary conditions, at x=0 the fluid temperature must be T_∞ at any time. The fluid temperature at x=h_c must be established, at any time, by Eq. (A1.20) or its various generalizations. In this case, Eq. (1.24) gives:

$$T_f(x,t) = T_\infty + (T - T_\infty) \cdot \frac{(1-\exp(-\frac{x}{\lambda}))}{(1-\exp(-\frac{h_c}{\lambda}))} \tag{A1.26}$$

Alternatively, provided Eq. (A1.20) holds, the temperature profile is:

$$T_f(x,t) = T_\infty + (T_0 - T_\infty) \cdot exp(-\frac{t}{\tau}) \cdot \frac{(1-exp(-\frac{x}{\lambda}))}{(1-exp(-\frac{h_c}{\lambda}))} \tag{A1.27}$$

According to Eqs. (A1.26) and (A1.27) if, as in our configurations, one has NTU>>1, then λ→0 and the fluid temperature is nearly constant inside the exchanger. Finally, it has to be noticed that the previous calculations are valid for cylindrical units. However, under the hypothesis that the spherical units are piled up in cylinders with base diameter equal to their diameter, it is easy to show that the previous calculation are still valid, as long as h_c is replaced by:

$$\frac{4}{3} \cdot h_c \tag{A1.28}$$

ANNEX A2
DOMESTIC OVEN MODEL

Let us develop a mathematical model for a heat storage/recovery system, coupled to a domestic oven. Later it will be shown that the temperature of an oven whose thermal energy in excess of T_0 is removed by sucking hot air from its cavity and replacing it with cold air is given by:

$$T_{\text{in}}(t) = T_\infty + (T_0 - T_\infty) \cdot exp(-\theta) \tag{A2.1}$$

By combining Eqs. (A1.17)-(A1.19) with Eq. (A2.1), one has, for the fluid and solid outlet temperature:

$$T = T_0 + (T_\infty - T_0) \cdot \theta \cdot exp(-\theta) \tag{A2.2}$$

Inspection of the previous equation shows that it only makes sense to charge the module until θ=1. Beyond this time, in fact, the material would be giving heat to the thermo-vector fluid. One would also like to have:

$$E = M \cdot C \cdot \Delta T \tag{A2.3}$$

$$W = \dot{m} \cdot C_p \cdot \Delta T \tag{A2.4}$$

where E is the energy deposed in the module, W is the average power transported by the fluid, ΔT is a suitable temperature difference. Considering the situation at θ=1 and using Eqs. (A2.1) and (A2.2), one shows that Eqs. (A2.3) and (A2.4) apply, with:

$$\Delta T = \widetilde{T_\infty} - T_0 \tag{A2.5}$$

where $\widetilde{T_\infty}$ is the temperature at θ=1. One then has:

$$\widetilde{T_\infty} = T_\infty - k \cdot (T_\infty - T_0) \tag{A2.6}$$

$$k = 1 - e^{-1} \approx 0.63 \tag{A2.7}$$

In the previous equations:

$$\theta = \frac{t}{\tau} \tag{A2.8}$$

$$\tau = \frac{M \cdot C}{\dot{m} \cdot C_p} \tag{A2.9}$$

where M is the solid mass, C the solid specific heat, C_p the fluid specific heat, $\dot{m}$ the fluid flow rate.

It is possible to prove that the monotonically increasing part of Eq. (A2.2) can be approximated by an exponential rise, having an effective asymptotic temperature given by Eqs. (A2.6) and (A2.7). In order to demonstrate this, let us first observe that the above-mentioned curve portion can be fitted by:

$$T = \widetilde{T_\infty} + (T_0 - \widetilde{T_\infty}) \cdot exp(-e \cdot \theta) \tag{A2.10}$$

In fact, if one tries to fit Eq. (A2.2) with Eq. (A2.10), with a time constant:

$$\theta' = a \cdot \theta \tag{A2.11}$$

it turns out that:

$$\theta \cdot exp(-\theta) \approx (1-k) \cdot (1 - exp(-a \cdot \theta)) \tag{A2.12}$$

and, taking the limit for θ → 0:

$$a = \frac{1}{1-k} = e \approx 2.72 \tag{A2.13}$$

The previous results are suggested by the physics of the problem. They were double-checked through a least square fit, performed with Mathematica, by sampling the function on 10^5 equally spaced points. The result was:

$$\begin{aligned} k &\approx 0.59 \\ a &\approx 2.67 \end{aligned} \tag{A2.14}$$

The parameter values suggested by the physics of the problem were adopted, so that:

$$\begin{aligned} k &= 1 - \frac{1}{e} \approx 0.63 \\ a &= e \approx 2.72 \end{aligned} \tag{A2.15}$$

By employing Mathematica, a fitting error of 1.3%, with T_∞=180 °C, T_0=20 °C, was calculated. These are the typical temperatures for a domestic oven [R. Mereu, personal communication, 2013] and the effective temperature, then, turned out to be ~80 °C. Due to error propagation, correction factors are needed for the charge and energy efficiencies of the system, with respect to the expressions coming from Eq. (A2.10). Such correction factors were calculated with Mathematica and:

$$\eta_c = (1 - exp(-\theta')) \cdot (1 + 0.37 \cdot \theta - 0.30 \cdot \theta^2) \tag{A2.16}$$

and:

$$\eta_e = \frac{(1-exp(-\theta\prime))}{\theta\prime} \cdot (1 + 0.70 \cdot \theta) \quad \text{(A2.17)}$$

$$\theta' = e \cdot \theta \quad \text{(A2.18)}$$

Let us now give an expression for the module charging time, t_c. In this respect, let us observe that Eq. (A2.10) can be rewritten as:

$$T = \widetilde{T_\infty} + (T_0 - \widetilde{T_\infty}) \cdot exp(-\frac{t}{t_c}) \quad \text{(A2.19)}$$

with, see Eqs. (A2.3) and (A2.4):

$$t_c = \frac{E}{e \cdot W} \quad \text{(A2.20)}$$

Let us finally give a proof of the validity of Eq. (A2.1). The first question one might ask is how much thermal energy can be extracted from the hot air in the oven chamber and how much from its metallic structure. It was estimated [R. Mereu, personal communication, 2013] that ~1.1 MJ can be extracted by cooling the oven structure. On the other hand, cooling a 48 l (40x40x30 cm) chamber (from 180 to 20 °C), one can merely extract ~0.01 MJ (if one assumes, for air, a density of 1.2 kg/m^3 and a specific heat of 1 kJ/(kg·°C) [Carvill, 2003].

The model to be used for describing the oven structure cooling is the same as the one developed in Annex A1. Eq. (A2.1) therefore applies, provided the approximations used to derive it are applicable. It only remains to be checked that the characteristic time for making the oven structure temperature uniform is much smaller than the time-scale involved (18 min). Let us then observe that [Mehrer et al., 2009] a temperature disturbance spreads as a Gaussian, having a standard deviation:

$$\sigma(t) = \sqrt{2 \cdot \alpha_p \cdot t} \quad \text{(A2.21)}$$

where α_p is the thermal diffusivity. If one then supposes that such a temperature disturbance reaches the whole oven when $3 \cdot \sigma = l_o$, where l_o is its characteristic length, the time t_o at which this happens is:

$$t_o = \frac{l_o^2}{18 \cdot \alpha_p} \quad \text{(A2.22)}$$

Applying Eq. (A2.22) with $\alpha p = 4.10\text{-}6$ m^2/s (for a typical steel [Carvill, 2003]) and supposing that the structure is cooled by air from both its inner and outer sides so that, if the structure characteristic dimension is ~10 cm, then $l_0 \approx 5$ cm, the time-scale for heat diffusion turns out to be ~35 sec. Since one imposes a heat extraction time of 18 min, the characteristic time for uniforming temperature in the chamber is ~3% of the heat extraction time. One can then assume a uniform temperature distribution in the oven structure, as required by the approximations described in Annex A3.

ANNEX A3
MODEL APPROXIMATIONS

In Annex A1, two approximations were tacitly introduced:

- The material is able to follow the fluid time dynamics,
- The temperature of the material is constant through it.

As shown below, it turns out that these hypotheses can be translated into conditions on two non-dimensional numbers (Fo and NTU). In order to quantify the errors due to these approximations, let us define the Biot number (a non-dimensional radius) [Yovanovich, 1998]:

$$Bi = \frac{U \cdot r_u}{k_m} \quad \text{(A3.1)}$$

where U is the heat transfer coefficient, r_u is the storage unit radius, k_m is the material thermal conductivity. The heat storage unit can be considered as a point-like object if the Biot number is [Yovanovich, 1998]:

$$Bi < 0.20 \quad \text{(A3.2)}$$

but the discussion that follows shows that, for the systems proposed here, Bi≈0.45. The proposed lumped parameter approach would then seem not to be applicable. However, in the following it will be shown that condition (A3.2), in this case, is too drastic. The lumped parameter formalism indeed makes sense, provided the errors committed by applying it are kept under control.

In order to deal with axial diffusion, let us then introduce the Fourier number [Yovanovich, 1998]:

$$Fo = \frac{\alpha_m \cdot t}{h_c^2} \quad \text{(A3.3)}$$

where α_m is the thermal diffusivity of the material, t is a suitable time, h_c the module height and let us suppose that a heat wave starts from both sides of the cylinder, traveling towards its interior.

It is well-known [Mehrer et al., 2009] that the wave spreads as a Gaussian, with:

$$\sigma(t) = \sqrt{2 \cdot \alpha_m \cdot t} \quad \text{(A3.4)}$$

It can then be assumed that the temperature disturbance has reached the whole cylinder when $3 \cdot \sigma = \frac{1}{2} \cdot h_c$. This happens at a time:

$$t_u = \frac{h_c^2}{72 \cdot \alpha_m} \quad \text{(A3.5)}$$

In the following, it will be required that, although the body cannot be considered as a point-like object, the material and dimensions of the cylindrical units are such that the heat diffusion time-scale (as expressed by the Fourier number) is negligible with respect to the characteristic module cooling time.

In particular, in Annex A1 it is shown that the storage units get heated exponentially, with:

$$\tau = \frac{M \cdot C}{\dot{m} \cdot C_p} \quad \text{(A3.6)}$$

where M is the material mass, C the material specific heat, $\dot{m}$ the mass flow rate, Cp the fluid specific heat. It was then imposed that:

$$t_u \leq \frac{\tau}{3} \tag{A3.7}$$

(where the factor 3 is due to the exponential nature of the process) from which, by employing Eq. (A3.3) and (A3.5), it follows that:

$$Fo(\tau) \geq 0.04 \tag{A3.8}$$

Let us come to radial diffusion. In this respect, it can be noticed that if Eq. (A3.8) is satisfied for axial heat diffusion, it is satisfied for radial diffusion, as well, since in the cylindrical heat storage units one has $r_u<h_c$. However, there is one more condition to be satisfied. As previously mentioned, in fact, a lumped parameter solution is unacceptable for Bi>0.20. Nevertheless, such a solution can be employed if (as when justifying approximations) accuracy is not an issue [Yovanovich, 1998]. By using the lumped parameter solution, it can be shown that the heat storage unit reaches radial thermal equilibrium after [Yovanovich, 1998]:

$$\tau_u \approx \frac{1}{Bi} \cdot \frac{r_u^2}{\alpha_m} \tag{A3.9}$$

The material is then able to follow the time dynamics of the fluid if its time dynamics is fast enough, as compared to the thermal module time scale:

$$\tau_u \ll \tau \tag{A3.10}$$

It is easy to show that the previous equation can be rewritten as [Bejan, 1978]:

$$NTU \gg 1 \tag{A3.11}$$

and:

$$NTU = \frac{U \cdot S}{\dot{m} \cdot C_p} \tag{A3.12}$$

where U is the heat exchange coefficient, S is the heat exchange surface. Let us point out that Eq. (A3.11) is arrived at by employing, Eq. (A3.9), the definition [Yovanovich, 1998]:

$$\alpha_m = \frac{k_m}{\rho_m \cdot C} \tag{A3.13}$$

(where ρ_m is the material density) and Eqs. (A3.2) and (A3.6) for the Biot number and time constant.

Let us observe that conditions (A3.10) and (A3.11) are equivalent and the latter involves the NTU parameter. On the other hand, NTU depends on the exchange surface rather than on cylinder dimensions separately. The radial condition, then, applies to axial heat diffusion, as well.

One then can guarantee that the material is able to follow the time dynamics of the fluid by imposing Eq. (A3.8) and:

$$NTU \geq 3 \tag{A3.14}$$

where the condition given by Eq. (A3.14) is imposed since the parameter enters the error equations under an exponential. This gives an acceptable error, as shown later.

Let us finally evaluate the temperature errors related to model approximations. In particular, one has the following error sources:

- the temperature time-profile is just fitted by an exponential and not exponential (ε_{fit}),
- the temperature is not constant throughout the material (ε_{nct}),
- the material is not able to follow the fluid time dynamics (ε_{dyn}).

Temperature errors, here, are meant to be infinite-norm errors, i.e. maximum errors over the space and time domains, with respect to the real behaviour. The total model error was estimated by summing the various error terms in quadrature:

$$\epsilon = \sqrt{\epsilon_{fit}^2 + \epsilon_{nct}^2 + \epsilon_{dyn}^2} \tag{A3.15}$$

Let us first estimate the error due to fitting the oven temperature profile, Annex A2. The value of ε_{fit} is, of course, null for constant inlet temperature. Its value for a domestic oven was estimated, with Mathematica, to be 1.3%. Let us then estimate ε_{nct}. The temperature drop across the material ΔT_m can be calculated from W (the power transferred to the material), ΔT (the difference between the fluid inlet and room temperatures), η_e (the energy efficiency). In particular [Sharma et al., 2009]:

$$\Delta T_m \approx \frac{W}{U \cdot S} = \frac{\dot{m} \cdot C_p \cdot \Delta T \cdot \eta_e}{U \cdot S} = \frac{\Delta T \cdot \eta_e}{NTU} \tag{A3.16}$$

Let us assume $\varepsilon_{nct} \approx \frac{1}{2} \cdot \Delta T_m / T_\infty$ where T_∞ approximates the average temperature in the material, as shown by integrating Eq. (A1.27) with NTU->∞ (in practice, NTU≥3). One can then estimate the error.

In particular, one has:

$$\epsilon_{nct} \approx \frac{\Delta T \cdot \eta_e}{2 \cdot NTU \cdot T_\infty} \tag{A3.17}$$

By assuming $\Delta T \leq 60$ °C, $\eta_e \leq 0.9$, NTU=3 and $T_\infty \geq 40$ °C (313 °K) [MOXOFF, 2012b], one has ε_{nct}=2.9%. Let us then estimate εdyn, the error committed by having a finite NTU or, equivalently, y≠1. This is due to the fact that the material is not fully able to follow the fluid temperature variation. By using Eq. (A1.11), ε_{dyn} can be estimated by calculating dT/dy, then multiplying by dy≈1-y ($dy \approx e^{-NTU}$) and dividing by the average temperature:

$$\epsilon_{dyn}(t) = \frac{\Delta T}{T_\infty} \cdot (y \cdot \theta) \cdot exp(-y \cdot \theta) \cdot \frac{exp(-NTU)}{1 - exp(-NTU)} \tag{A3.18}$$

The previous expression reaches its maximum for y·θ=1. For NTU>>1:

$$\epsilon_{dyn} \approx \frac{\Delta T}{T_\infty} \cdot exp(-(1 + NTU)) \tag{A3.19}$$

By assuming that NTU=3, $\Delta T \leq 60$ °C, $T_\infty \geq 40$ °C (313 °K) [MOXOFF, 2012b], one obtains ε_{nct}=0.4%.

By applying the above-mentioned equations, it is then possible to estimate the maximum space/time error, with

respect to the real behaviour. In particular, by combining the previous results one can estimate that ε=3.2% for appliances dissipating at a time-variable temperature (ovens) and ε=2.9% for appliances dissipating at a time-constant temperature (refrigerators and cook-top planes). Given the approximate nature of the previous considerations, one can then state that the error is ~3% for any appliance type.

ANNEX A4
MODEL EXTENSION TO PCMS

Let us now extend the previous model to PCMs (phase change materials), as opposed to SHMs (sensible heat materials). For the fluid outlet and solid temperature (in the paper, it was shown that they nearly coincide), one has:

$$T = T_\infty + (T_0 - T_\infty) \cdot exp(-\theta) \quad \text{(A4.1)}$$

The previous equation holds for $T<T_f$, where T_f is the fusion temperature. During PCM fusion, one has:

$$T = T_f \quad \text{(A4.2)}$$

and, after fusion:

$$T = T_\infty + (T_f - T_\infty) \cdot exp(-(\theta - \theta_f - \theta_f^{(l)})) \quad \text{(A4.3)}$$

where θ_f is the time taken for fusion (normalized to the solid specific heat), $\theta^{(l/s)}_f$ is the fusion ending time (normalized to the liquid/solid specific heat). θ is also normalized to the liquid time constant. One then has to modify the SHM efficiency formulae accordingly. In order to achieve this, let us introduce an average specific heat:

$$C_a = \frac{C_s \cdot T_f - T_0}{T_\infty - T_0} + \frac{C_l \cdot T_\infty - T_f}{T_\infty - T_0} \quad \text{(A4.4)}$$

where C_s is the specific heat of the material in the solid state and C_l its specific heat in the liquid state. Let us notice that, provided $C_s \approx C_l$:

$$C_a \approx C_s \approx C_l \quad \text{(A4.5)}$$

One also has to introduce an effective specific heat that takes fusion into account:

$$C_e = C_a + C_f \quad \text{(A4.6)}$$

and:

$$C_f = \frac{\Delta H}{T_\infty - T_0} \quad \text{(A4.7)}$$

where C_f is the fusion equivalent specific heat and ΔH is the fusion enthalpy. The charge efficiency is then given by:

$$\eta_c = \frac{C_s \cdot (T_f - T_0) + \Delta H + C_l \cdot (T - T_f)}{C_e \cdot (T_\infty - T_0)} \quad \text{(A4.8)}$$

$$\eta_c = 1 - \xi_l \cdot exp(+\theta_f + \theta_f^{(l)} - \theta_f^{(s)}) \cdot exp(-\theta) \quad \text{(A4.9)}$$

The previous expression is obtained since, as shown by Eq. (A1.20):

$$\frac{T_\infty - T_f}{T_\infty - T_0} = exp(-\theta_f^{(s)}) \quad \text{(A4.10)}$$

In the previous equations, the following definition was employed:

$$\xi_i = \frac{C_i}{C_e} \quad \text{(A4.11)}$$

where i=a,s,l,f and:

$$\xi_a + \xi_t = 1 \quad \text{(A4.12)}$$

Under hypothesis (A4.5), then:

$$\eta_c = 1 - (1 - \xi_f) \cdot exp(+\theta_f) \cdot exp(-\theta) \quad \text{(A4.13)}$$

As for the energy efficiency, by repeating the steps leading to Eq. (A4.9):

$$\eta_e = \frac{1 - \xi_l \cdot exp(+\theta_f + \theta_f^{(l)} - \theta_f^{(s)}) \cdot exp(-\theta)}{\xi_l \cdot \theta} \quad \text{(A4.14)}$$

Under hypothesis (A4.5):

$$\eta_e = \frac{1 - (1 - \xi_f) \cdot exp(+\theta_f) \cdot exp(-\theta)}{(1 - \xi_f) \cdot \theta} \quad \text{(A4.15)}$$

Later in this Annex, it will be demonstrated that over-dimensioning the modules by a factor fd, so as to make the effective charge efficiency larger and allow modules to respect the conditions derived in Annex A3, is a convenient choice. The charge time is then $\tau \approx 1/f_d$, to which the fusion duration must be added. From now on, hypothesis (A4.5) will be adopted and the fusion duration (normalized to the liquid time constant) will be taken as

$$\theta_f = \frac{M \cdot \Delta H}{\eta_e^{opt} \cdot W \cdot \tau} = \frac{M \cdot \Delta H}{\eta_e^{opt} \cdot \dot{m} \cdot C_p \cdot \Delta T \cdot \tau} = \frac{\xi_f}{1 - \xi_f} \cdot \frac{1}{\eta_e^{opt}} \quad \text{(A4.16)}$$

where M is the material mass, ΔH the fusion enthalpy, W is the power transported by the fluid, C_p is the fluid specific heat, $\Delta T = T_\infty - T_0$. The optimum charge time is then given by:

$$\theta_{opt} = \frac{\xi_f}{1 - \xi_f} \cdot \frac{1}{\eta_e^{opt}} + \frac{1}{f_d} \quad \text{(A4.17)}$$

In the previous equation, the factor $1/f_d$ is due to the fact that τ is proportional to M, Eq. (A1.10), and the optimum charging time is calculated for a material mass M/fd, the mass the material would have, were the module not over-dimensioned.

Choosing $f_d>1$ increases efficiency. In fact, the energy accumulated into a module is $\eta_c \cdot E_0$. If one increases the energy size and makes the module larger by f_d, one can pretend to have the same energy size and an increased charge efficiency. Let us calculate the optimal charge efficiency. This quantity is obtained by multiplying Eq. (A4.13) by f_d and then employing Eq. (A4.16) and (A4.17):

$$\eta_c^{opt} = f_d \cdot (1 - (1 - \xi_f) \cdot exp(-\frac{1}{f_d})) \quad \text{(A4.18)}$$

The optimal system energy efficiency is then calculated by substituting Eq. (A4.16) and (A4.17) in Eq. (A4.15):

$$\eta_e^{opt} = \frac{\eta_c^{opt}}{f_d \cdot (1-\xi_f) \cdot \theta_{opt}} = f_d \cdot (1 - exp(-\frac{1}{f_d})) \quad \text{(A4.19)}$$

Let us point out that the PCMs considered in this study are such that, at ~10%:

$$\xi_l \approx \xi_s \approx \xi_f \approx \xi_a \approx \frac{1}{2} \quad \text{(A4.20)}$$

It was verified that, by using such an approximation, a conservative design criterion is actually employed, in that the module height is only slightly over-estimated (which can only increase the heat exchange efficiency). Finally, let us notice that the charge efficiency formulae for SMSs can be obtained by assuming a null value for ξ_f in Eqs. (A4.18) and (A4.19). This justifies Eqs. (37) to (40) of the main text.

ANNEX A5
EXERGETIC EFFICIENCY

Eq. (A1.20) shows that for t→∞ the fluid inlet temperature is equal to its outlet temperature. As a consequence of this, Annex A1, the charge efficiency tends to one but the energy efficiency tends to zero, since the only thing that the fluid does, for t→∞, is dissipating energy without transferring heat to the material. It is then intuitive that there must be an optimum point, beyond which it makes little sense to keep charging the heat storage module. In order to determine such a point, one has to calculate (and maximize) the exergetic efficiency of the system, i.e. the ratio between the potential work that is dissipated by the system and the maximum work the system can do while approaching equilibrium with its environment. This potential work has been named exergy [Wall, 1977].

The exergy of a system is:

$$E = U + p_o \cdot V - T_0 \cdot S \quad \text{(A5.1)}$$

where U is the internal energy of the system, T_0 is the environment temperature, p_0 is its pressure, V is the system volume, S is the system entropy. It is important to notice that Eq. (A5.1), by employing the first principle of thermodynamics, can be written as:

$$E = (p_o - p) \cdot V - (T_0 - T) \cdot S \quad \text{(A5.2)}$$

This shows that the exergy of a system in equilibrium with its environment is zero.

The importance of the exergy concept can be fully appreciated by observing that, if W is the work performed by the system, one has [Wall, 1977]:

$$W = E - T_0 \cdot \Delta S_{tot} \quad \text{(A5.3)}$$

where ΔS_{tot} is the total (i.e. system plus environment) entropy variation. Since the total entropy variation can only be positive (or null for reversible processes), Eq. (A5.3) leads to:

$$W \leq E \quad \text{(A5.4)}$$

An immediate consequence of Eq. (A5.3) is that the dissipated potential work is:

$$W_{dis} = T_0 \cdot \Delta S_{tot} \quad \text{(A5.5)}$$

The exergetic efficiency is then [Oguzhan et al., 2019 - Rosen et al., 1988]:

$$\eta_{ex} = \frac{W}{W_{max}} = \frac{E - W_{dis}}{E} = 1 - \frac{W_{dis}}{E} \quad \text{(A5.6)}$$

where W_{max}=E, Eq. (A5.4). For calculating this quantity, one has to determine:

$$\frac{W_{dis}}{E} \quad \text{(A5.7)}$$

Let us then start with appliances dissipating at a constant temperature, under y→1 (see Annex A1), and look at W_{dis} and the entropy variation ΔS_{tot}. The entropy variation includes [Bejan, 1978 - Rosen et al., 1988]:

- the fluid going from temperature T_∞ to T_0, at constant pressure,
- the environment receiving heat at temperature T_0, coming from the internal energy of the fluid (from T to T_0),
- the material going from temperature T_0 to temperature T.

It was verified that fusion, if present, gives a negligible contribution to W_{dis}. By using Eq. (A5.5), then, one has [Bejan, 1978]:

$$\frac{W_{dis}}{T_0} = -\dot{m} \cdot c_p \cdot t \cdot log(\frac{T_\infty}{T_0}) + \dot{m} \cdot c_p \cdot (\int_0^t ds \cdot (\frac{T - T_0}{T_0}) + M \cdot C \cdot log(\frac{T}{T_0}) \quad \text{(A5.8)}$$

where $\dot{m}$ is the fluid mass flow rate, C_p its specific heat, M the material mass, C its specific heat. As for exergy, one has to use of Eq. (A5.1), considering that the system that does work is the (non-expanding) fluid while it passes T to T_0.

By calculating E with reference to the (p_0,T_0) state one has [Bejan, 1978]:

$$\frac{E}{T_0} = \dot{m} \cdot c_p \cdot t \cdot (\frac{T_\infty - T_0}{T_0} - log(\frac{T_\infty}{T_0})) \quad \text{(A5.9)}$$

Let us then introduce the non-dimensional time and temperature [Bejan, 1978]:

$$\theta = \frac{\dot{m} \cdot c_p \cdot t}{M \cdot C} \quad \text{(A5.10)}$$

and:

$$\tau_\infty = \frac{T_\infty - T_0}{T_0} \quad \text{(A5.11)}$$

The exergetic efficiency, by using Eqs. (A1.7), (A1.20) and (A1.21), can then be expressed in the following way [Bejan, 1978]:

$$\eta_{ex} = \frac{1}{\theta \cdot (\tau_\infty - log(1+\tau_\infty))} \cdot (\tau_\infty \cdot (1 - exp(-\theta)) - log(1 + \tau_\infty \cdot (1 - exp(-\theta)))) \quad \text{(A5.12)}$$

This is the function to be maximized. In particular, for a given $\tau\infty$ (a given appliance at room temperature), one has to find a non-dimensional time θ_{opt} that maximizes the exergetic efficiency. This is the time beyond which there is no point in charging a module. As for the case of non-constant appliance inlet temperatures, e.g. a domestic oven, in Annex A2 it was shown that these appliances can be treated as if they dissipated heat at an effective constant temperature. Eq. (A5.12) can then be applied. As for systems with y≠1, Eq. (5.12) still applies, provided θ is just replaced by y·θ [Bejan, 1978]. Finally, let us notice that the optimum system exergetic efficiency is only a weak function of the appliance temperature. Its value turned out to be ~40%, for any appliance type and temperature.

ANNEX A6
SYSTEM OPTIMIZATION

To the best of the author's knowledge, according the thermal engineering literature [Bejan, 1978 - Bjurström et al., 1985] the thermodynamic optimization of a heat storage/recovery system cannot be performed analytically. In this Annex, it is demonstrated that a semi-analytical optimization can indeed be performed and, as a matter of fact, gives surprisingly simple results.

The thermodynamic module optimization was performed with Mathematica and turned out to be a lengthy exercise. Due to space limitations, here it is only possible to summarize the optimization steps. The author, upon request, can supply further details and the Mathematica script employed. The semi-analytical optimization process included the following steps:

- the derivative (FD) of the exergetic efficiency with respect to θ, fixing room temperature (RT) at 20 °C, was calculated,
- FD was developed in a Taylor series in τ_∞ and θ_{opt}, around their mean values,
- the mean value of τ_∞ was estimated as the τ_∞ at the mean value of the appliance dissipation temperature range (70 °C [MOXOFF, 2012b]),
- the mean value of θ_{opt} was estimated by graphically determining the θ for which the exergetic efficiency was maximum at 70 °C,
- the equation FD=0 was solved by series, replacing FD with its Taylor approximation at increasing τ_∞ and θ_{opt} orders,
- for each order, the values of FD on a suitable space-time grid were plotted. The minimum τ_∞ and θ_{opt} orders for which FD saturate were taken to represent the real solution,
- θ_{opt} and T_{opt}, were calculated as the analytical solution to the equation FD=0, as determined by Mathematica,
- ·rather than redoing the calculations for RT≠20 °C, it was verified that, for -40 °C<RT<40 °C, the solution varies by less than 1 °C.

The solution for the optimum module charge temperature, T_{opt}, obtained with the above-mentioned method, is:

$$T_{opt} = 0.70 \cdot T_\infty + 0.30 \cdot T_0 \tag{A6.1}$$

The fact that the coefficients of the polynomial add up to one was explained with the analytical developments that follow. In particular, it was found that the same results as the above-mentioned Taylor approach can be arrived at with simple analytical considerations. In fact, from Eq. (A1.20):

$$\theta_{opt} = log(\frac{T_\infty - T_0}{T_\infty - T_{opt}}) \tag{A6.2}$$

If one replaces the adimensional temperature θ_{opt} with its average value $<\theta_{opt}>$, the following expression is obtained:

$$T_{opt} = (1-\alpha) \cdot T_\infty + \alpha \cdot T_0 \tag{A6.3}$$

$$\alpha = exp(-<\theta_{opt}>) \tag{A6.4}$$

Besides re-deriving Eq. (A6.1), it is then also possible to explain the fact that its coefficients add up to one, as shown by Eq. (A6.3). The values of $<\theta_{opt}>$ and α can then be determined as detailed above. It turns out that $<\theta_{opt}>$=1.2 and α=0.30, in agreement with Eq. (A6.1). The procedure leading to Eq. (A6.1), anyway, shows that Eqs. (A6.3) and (A6.4) are exact solutions and not merely first order approximations.

One can also use Eq. (A6.3) without knowing α by assuming, as a first approximation, that α=½. By Taylor approximation, then, it easy to show that the arithmetic mean can be approximated with the geometric mean. For T<100 °C, at 5%:

$$T_{opt} \approx \sqrt{T_0 \cdot T_\infty} \tag{A6.5}$$

The temperature for which θ=1, T_c, is seen to be slightly different from T_{opt}:

$$T_c = T_{opt} + \partial_\theta T_{opt}(\theta_{opt}) \cdot (\theta_c - \theta_{opt}) = T_{opt} + (T_\infty - T_0) \cdot \alpha \cdot (1 + log(\alpha)) \tag{A6.6}$$

where Eqs. (A6.3)-(A6.4) were employed. By further applying Eq. (A6.3), one has:

$$T_c = (1-\tilde{\alpha}) \cdot T_\infty + \tilde{\alpha} \cdot T_0 \tag{A6.7}$$

where:

$$\tilde{\alpha} = -\alpha \cdot log(\alpha) \tag{A6.8}$$

Putting α=0.30 in Eqs. (A6.7) and (A6.8), one obtains:

$$T_c = 0.64 \cdot T_\infty + 0.36 \cdot T_0 \tag{A6.9}$$

Finally, let us notice that the assumption θ=1 simplifies calculations. Furthermore, it was verified that, at least in the 20-100 °C range, Eqs. (A6.1) and (A6.9) differ by 1.4%, at worst. Eq. (A6.9) is the result reported in the paper (where, with a slight notational abuse, Tc was renominated as T_{opt}).

ANNEX A7
PRESSURE DROP - MINIMUM FLUIDIZATION

Let us calculate the pressure drop experienced by the fluid and the fixed bed fluidization velocity. The concept

of minimal fluidization velocity originates from the fact that, beyond such a velocity, one has a fluidized bed, with an unstable behaviour (formation of channels where the fluid does not interact) for particle diameters ≥1 cm [Holdich, 2002]. Let us first consider a fixed bed. The pressure drop, for a laminar fixed bed with circular baffles, is indeed given by [Holdich, 2002]:

$$\Delta p_{fb} = 180 \cdot \frac{\epsilon_3^2}{(1-\epsilon_3)^3} \cdot \frac{\mu_f \cdot v_f \cdot h_c}{d_u^2} \quad \text{(A7.1)}$$

where ε_3 is the sphere packing density, μ_f the fluid velocity, v_f the average interstitial fluid velocity, h_c the bed height and d_u the unit diameter. The pressure drop is a monotonically increasing function of the sphere packing density and ε_3=0.74, the maximum possible value [Holdich, 2002], was assumed, so as to be on the safe side. By assuming d_u=1 cm, h_c≤20 cm, v_f≤2.3 m/s [MOXOFF, 2012b], a maximum pressure drop ~5 mbar (μ_f=1.8·10-5 kg/m·s [Biyikoglu, 2002]) is calculated. The pressure drop is then ~0.5% of the atmospheric pressure, at worst.

Let us come to the shell-and-tube exchanger. The expression for the pressure drop of the heat exchanger [Shah et al., 1998] is made up additive terms. It was verified that the terms describing baffle influence are dominating and:

$$\Delta p_{hh} = N_b \cdot (2 + 0.6 \cdot \widetilde{N_r}) \cdot \frac{\rho_f \cdot v_f^2}{2} + 4 \cdot f \cdot \widetilde{N_r} \cdot (N_b - 1) \cdot \frac{\rho_f \cdot v_f^2}{2} \quad \text{(A7.2)}$$

where N_b is the number of baffles $\widetilde{N_r}$ is an effective number of tube rows, Eq. (A7.3), ρ_f the fluid density, v_f the interstitial fluid velocity, f the friction factor (one has ≤0.3 for Re≥120 [Fernandez et al., 2010]). In Eq. (A7.2), $\widetilde{N_r}$ is given by [Shah et al., 1998]:

$$\widetilde{N_r} = \frac{0.05 \cdot d_c}{d_u} \quad \text{(A7.3)}$$

where d_c is the cylindrical module diameter and d_u is the unit diameter.

Eq. (A7.3) was derived from [Shah et al., 1998] under the hypothesis that the baffle cut (cylinder diameter minus baffle height) be 0.05 times the cylinder diameter and the tube pitch (the minimum distance between tubes) be 1.25 times the cylinder diameter [MOXOFF, 2012b]. Since one has d_c=50, d_u=5 mm [MOXOFF, 2012b], then $\widetilde{N_r}$=5. Assuming N_b=8 and v_f=2.3 m/s [MOXOFF, 2012b], Eq. (A7.3), with ρ_f =1.2 kg/m3 [Biyikoglu, 2002], gives a pressure drop of ~3 mbar or ~0.3% of the atmospheric pressure, at worst.

Let us finally come to the minimal fluidization velocity for a fixed or fluidized bed. This quantity is given by [Holdich, 2002]:

$$v_{mf} = \frac{1}{180} \cdot \frac{(1-\epsilon_3)^3}{\epsilon_3} \cdot \rho_m \cdot g \cdot \frac{d_u^2}{\mu_f} \quad \text{(A7.4)}$$

where ρ_m is the material density, g is the gravitational acceleration. Let us notice that the minimum fluidization velocity is a monotonically decreasing function of the sphere packing density, so that ε_3=0.74, the maximum possible value [Hales et al., 2006], was cautiously assumed. Since, for any material, ρ_m>765 kg/m^3 (see Tab.3) and g=9.8 m/s^2, one then has v_{mf}>5.5 m/s. Since from model simulations one gets v_f<2.3 m/s [MOXOFF, 2012b], the packed bed works out of the minimum fluidization regime and is therefore a fixed bed, as previously stated.

Seatific Journal
https://seatific.yildiz.edu.tr
DOI: https://doi.org/10.14744/seatific.2023.0008

Research Article

Numerical investigation of the resistance and static drift condition of the autosub submarine

Sare Nur ÇIPLAKKAYA*, Yasemin ARIKAN ÖZDEN

Department of Naval Architecture and Marine Engineering, Faculty of Naval Architecture and Maritime, Yildiz Technical University, Istanbul, Türkiye

ARTICLE INFO

Article history
Received: June 13, 2023
Revised: September 3, 2023
Accepted: September 25, 2023

Keywords:
Autosub submarine; CFD; maneuvering; resistance; static drift

ABSTRACT

This study involves the force and moment calculations using the scaled and full-scale geometries of the Autosub submarine. The scale factor of the submarine is used as 1.346 according to the model size used in the experiments. Computational fluid dynamics calculations have been performed using RANS equations and the k-ω turbulence model. The resistance analyses have been conducted for speeds ranging from 0 to 2 m/s. Static drift analyses have been conducted between the range of 0° to 10° degrees drift angles at 2 degrees intervals. A mesh independence study has been carried out to determine the adequate mesh density. The mesh structure has been determined in the analyses for 6 degrees of drift angle and this mesh structure is used for other drift angles, and the results have been compared with experimental results from the open literature. Full-scale resistance analyses have been conducted, and the calculated resistance forces have been compared with the experimental and empirical data. The force and moment values obtained from static drift and resistance analyses are found to be consistent with experimental results presented in the literature.

Cite this article as: Çıplakkaya SN, Arıkan Özden Y. Numerical investigation of the resistance and static drift condition of the autosub submarine. Seatific 2023;3:2:71–84.

1. INTRODUCTION

One of the factors that determine the design of submarines is their maneuvering performance. During the process of determining maneuvering performance, it is crucial to calculate the maneuvering coefficients that represent the hydrodynamic effects. Obtaining the hydrodynamic coefficients which are part of the equations of motion is one of the most important parts for the maneuvering calculations (Cardenas et al., 2019). Computational fluid dynamics, empirical, and experimental methods are used to obtain the hydrodynamic characteristics of submarines. Hydrodynamic coefficients are usually obtained through experimental or numerical simulations. Experiments enable the direct determination of coefficients by making measurements, but due to the high cost and difficulty of experiments, numerical simulations are becoming increasingly popular. There are three main conditions at submarine's motion; acceleration, cruise and rotating at constant angular velocity. These three conditions should be investigated in order to obtain the maneuvering characteristics. The hydrodynamic forces due to acceleration effects

***Corresponding author.**
*E-mail address: yarikan@yildiz.edu.tr

are calculated through planar motion mechanism (PMM) experiments. The hydrodynamic forces and moments which occur at cruise are determined by towing tank tests while the angular velocity effects are carried out by rotating arm experiments (Efremov et al., 2019). Ship model testing experiments have different methods of calculating the hydrodynamic coefficients. For each method, the calculation methods differ. PMM is a hydrodynamic test system which allows to impose static drift and dynamic oscillating motions to a surface ship or submarine model. On the other hand, the rotating arm test, which is a different test setup, is used to obtain coefficients while the model is rotating with a constant angular velocity. To measure straight motion values such as longitudinal and lateral forces, the towing tank test are conducted. Thus, coefficients for drag, pitch or yaw angle are measured. Since in towing tank tests linear movements are obtained, measurements related to angular velocity cannot be obtained. This is what separates PMM test from the rotating arm test. The use of these test setups have a very important place in obtaining the hydrodynamic coefficients needed while designing a submarine (Saeidinezhad et al., 2015).

In this study, the Autosub underwater vehicle (AUV) is used which is a submarine developed by the British National Oceanography Centre. This submarine is commonly used by oceanographers for scientific research. The Autosub submarine is capable of staying underwater for extended periods of time and measures the physical, chemical, and biological properties of the underwater environment through various sensors. It is used for a variety of missions, such as exploring various geological features like underwater volcanoes, mountains, and canyons by measuring factors such as ocean temperature, salinity, and water quality. Additionally, it is used to examine and monitor underwater biological life. Furthermore, it is also used to investigate human-induced pollution and natural disasters, such as studying the effects of oil spills or tsunamis. Due to its ability to stay underwater for extended periods of time, the Autosub submarine has become an important tool in ocean sciences and has been used in numerous studies in this field.

The Autosub submarine is also a good validation tool used for submarine maneuvering studies since there are comprehensive model test results shared in the open literature. Model tests for the Autosub submarine have been performed on a model scaled by the scaling factor of 1.346 by Kimber & Marshfield (1993) at the HASLAR facility (270 m × 12.2 m × 5.5 m deep). Further tests were performed by Fallows (2004) on a 2.5 m scale model of the Autosub submarine at the Solent University Towing Tank (60 m × 3.7 m × 1.8 m deep). Experimental results in the open literature for the Autosub submarine are presented for submarines of different scale. Resistance results are presented for the full scale submarine while the PMM and rotating arm results are presented in non-dimensional form by the use of the scaled submarine model. The cruise speed of the Autosub is 2 m/s at full-scale. Kimber & Marshfield (1993) used in the scaled model a velocity magnitude of 2.69 m/s to obtain the same turbulence specification. Static drift tests are conducted at ±0 degree to ±10 degrees with an increment of 2 degrees (Kimber & Marshfield, 1993). Fallows (2004) in his PhD thesis shares a description of the experiments conducted in Southampton Institute Towing Tank. The full scale sea trials have been described in his study and experimental results have been shared (Fallows, 2004).

Pioneering studies for experimental studies concerning UWV's date back to the DARPA Suboff project where comprehensive model experiments are conducted. The DARPA Suboff Submarine is designed and recommended as a benchmark submarine model by Groves et al. (1989). The stability and control characteristics of the DARPA Suboff submarine model have been presented by Roddy (1990). There is a very large literature concerning the experimental and numerical investigation for the resistance prediction of underwater vehicles. Studies where the resistance of the generic forms like DARPA Suboff, BB2 Joubert, C-Scout are obtained experimentally (Crook, 1990; Roddy, 1990; Liu & Huang ,1998; Carrica et al., 2016; Thomas et al., 2003; Thomas et al., 2003; Mackay, M., 1988) and numerically (Bull, 1996; Anckermann, 2008; Fell, 2009; McDonald & Whitfield, 1996; Alin et al., 2010; Chase & Carrica, 2013; Carrica et al., 2019) can be mentioned as pioneering studies.

The estimation of the maneuvering characteristics of an underwater vehicle is a challenging problem with various methods developed to solve this problem (Kırıkbaş et al., 2021a, 2021b). Literature concerning the numerical determination of the hydrodynamic derivatives for maneuvering models date back to Davidson &Ship (Davidson & Schiff, 1946). After Abkowitz (1964) who extended higher order terms for surface ships, Gertler& Hagen (1967) introduced the first model for submerged body. With the increase of computational power, computational fluid dynamics calculations have spread. Toxopeus & Vaz (2009) have carried out a study where the DARPA Suboff submarine model is used to investigate numerically the flow at different drift angles around the bare hull configuration. They used their own computational fluid dynamics code by implementing different turbulence models and conducted a verification and validation study (Toxopeus & Vaz, 2009). In another study Vaz et al. (2010) calculated the maneuvering forces and moments of the DARPA SUBOFF AFF-1 and AFF-8 configurations for 0° and 18° drift angles by using two viscous-flow solvers. The influence of different turbulence models namely, RANS (Reynolds-Averaged-Navier-Stokes) and DDES (Delayed-Detached-Eddy-Simulation) methods on the calculation of forces and moments were investigated (Vaz et al., 2010). Other studies where the static drift characteristics of the DARPA Suboff Submarine are investigated are Duman et al. (2018) where the static drift simulations of DARPA Suboff bare hull form have been carried out to

calculate the hydrodynamic forces and moment acting on the hull in the horizontal plane (Duman et al., 2021). Atik (2021) who investigated the suitable solution mesh and turbulence model for the DARPA SUBOFF submarine AFF-1 hull form by performing static drift test simulations (Atik, 2021). Kahramanoglu (2023) who has examined the scale effects on the horizontal maneuvering derivatives for three different scales for the fully appended DARPA Suboff submarine (Kahramanoglu, 2023).

Maneuvering studies on the Autosub submarine using computational fluid dynamics calculations are as follows. By providing a comprehensive understanding of complex systems, Fallows (2004) outlined an approach to enhance the performance of UWV systems that are already in use. He used Taguchi experimental methods and made complementary sets of measurements in the laboratory on the full scale Autosub submarine. His study presented a method for developing a propulsion system for an AUV, such as the Autosub submarine. He presented about the generic attributes of these systems and their requirements.

Wu et al. in their study aimed to reduce the total resistance of the Autosub submarine. For this purpose, simulations of microbubbles were carried out. When the bubbles passed close to the hull of the submarine, it caused a decrease in the density of the fluid and turbulence viscosity. It has been shown that a 50% improvement in the total resistance was achieved in submarines (Wu et al., 2006).

In the study of Philips et al., the focus has been on evaluating the hull resistance of three different Autosub submarines, each designed with distinct shapes and sizes. The objective was to calculate the resistance experienced by these vehicles during their underwater missions. By utilizing CFD, the researchers were able to simulate the fluid flow around the Autosub submarine bodies and to accurately calculate the resistance values. The calculated resistance values were then compared with available experimental data obtained from physical tests and measurements. The results showed a favorable level of agreement between the calculated and experimental resistance values, indicating the reliability and accuracy of the CFD method (Phillips et al., 2007).

Using steady-state computational fluid dynamics (CFD), Phillips et al. effectively replicated experiments which are known as rotating arm test and towing tank test to obtain steady-state hydrodynamic derivatives for a torpedo-style Autosub underwater vehicle (AUV). The predictions demonstrated excellent agreement in estimating sway forces, although there was a slight overestimation in induced drag and yaw moments. In addition, numerical methods accurately obtained the dynamic stability limits of the submarine, in close agreement with the experimental measurements (Phillips et al., 2010).

In another study Phillips et al. calculated the resistance and hydrodynamic coefficients of the Autosub model, the CFD method used for steady-state conditions was used to successfully reproduce horizontal towing tank and rotating arm experiments for a torpedo-style Autosub, and steady-state hydrodynamic derivatives were derived. While there was a very good match for the prediction of the sideways force, the induced resistance and yaw moment were found to be slightly higher than obtained. (Phillips et al., 2011). In the study of Joung et al. an Autosub concept design model was created and subjected to analysis using a commercial CFD program to evaluate its resistance characteristics. The CFD analysis provided measurements of pressure and velocity distribution around the submarine, as well as resistance measurements. Additionally, the analyses were expanded to investigate the effects of adjusting the sail and communication transducer positions, as well as the angle of attack of the propulsion nozzle, in order to optimize the Autosub's design and minimize the resistance. The CFD results were validated by comparing the results with the ITTC 1957 correlation line. The study demonstrated that CFD can effectively estimate the total resistance of complex-shaped submarines. To expedite convergence, an automated mesh generation technique incorporating boundary layer inclusion was employed. Significant reductions in convergence time were achieved by examining object function and changing time of per iteration. It has been shown by sensitivity analysis that the angle of attack of the nozzle has a significant effect on the resistance value (Joung et al., 2012).

Aslan in his master thesis investigated the hydrodynamic coefficients of the DARPA Suboff and the Autosub submarine by means of static drift and rotating arm calculations. CFD calculations were performed and a good agreement between numerical and experimental results was achieved (Aslan, 2013). Can in his master thesis calculated the static drag coefficients of the DARPA Suboff submarine and the Autosub underwater vehicle. In this research, the computational fluid dynamics (CFD) method was employed, and data regarding the static drift and rotating arm calculations were made. Steady and unsteady rotating arm calculations were performed. The obtained hydrodynamic coefficients values were compared with the results of the experiments presented in the open literature, and the maximum error rate was presented as 10% (Can, 2014).

In this study the Autosub 3 geometry is used. The full-scale submarine has a length of 7 meter, a diameter of 0.9 meter and a speed range of 1 to 2 m/s. The aim of this study is to investigate the resistance and the static drift conditions of the Autosub submarine through CFD analysis. The yaw moments, sway forces and surge forces are investigated. Static drift conditions for different angles of attack are calculated for the scaled and resistance for different forward speed are obtained for the full-scale model of the Autosub. A mesh independency and a validation study has been done to determine an adequate mesh structure.

This study has been done with the use of the computational fluid dynamics software Simcenter STAR-CCM+ which is a commercial software based on finite volume method to

calculate the transport of physical quantities on a discretized mesh. For modelling the fluid flow the Navier–Stokes equations are solved in each of the cells. The steady hydrodynamic analyses have been done at different drift angles by using the software. A mesh independency study has been done to determine the mesh structure that will be used in the analyses with 0,2,4,6,8 and 10 degrees of static drift angle. The case for 6 degrees drift angle has been selected for the mesh independency study. Five different mesh structure has been generated with different mesh element sizes. The result of these five analyses has been compared with the experimental results given in Phillips et al. (2007). As a result of this mesh independence study the mesh size that gives the results compatible with the experimental results has been selected. This selected mesh structure has been used while computing the other analyses.

2.METHODOLOGY

2.1. Coordinate System

In axes known as body-fixed, the origin is positioned to be at the center of gravity of the submarine. The X-axis shows the nose of the submarine. The y-axis is drawn towards the starboard side, while the z-axis is towards the downside of the submarine. The body-fixed axes are used as above and the space-fixed axes are presented in Figure 1 (Zhao et al., 2022).

2.2. Motion Parameters

The primary motion parameters of a submarine consist of the linear velocity U and the angular velocity Ω while investigating in a coordinate system which is body-fixed. The velocity components of the submarine are lettered as linear velocity and angular velocity, respectively, as u and p in the x-axis, v and q in the y-axis, and w and r in the z-axis, as seen in Figure 1. These velocity magnitudes are the components of the linear U velocity and the angular ω velocity of the submarine. It can be calculated with the help of the submarine speed and the angles of the submarine (Zhao et al., 2022).

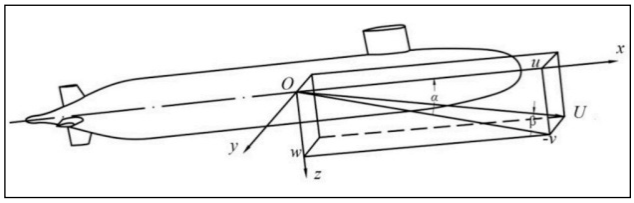

Figure 1. The coordinate systems (Zhao et al., 2022).

Equation 1 shows how the transformation mentioned above is applied.

$$u = Ucos\beta cos\alpha, v = -Usin\beta, w = Ucos\beta sin\alpha \quad (1)$$

$$u' = \frac{u}{U} = cos\beta cos\alpha, v' = \frac{v}{U} = sin\beta, w' = \frac{w}{U} = cos\beta sin\alpha$$

Equation (2) displays the values of the three components of angular velocity (p, q, and r) when the sail is positioned horizontally on the bottom.

$$p = sin\Omega\alpha, q = -\Omega cos\alpha sin\psi, r = -\Omega cos\alpha cos\psi \quad (2)$$

$$p' = \frac{pL}{U}, q' = \frac{qL}{U} = sin\beta, r' = \frac{rL}{U}$$

Equation (3) provides the values of the three components of angular velocity (p, q, and r) when the sail is positioned vertically on the starboard side.

$$p = -\Omega sin\beta, q = \Omega cos\beta cos\psi, r = -\Omega cos\beta sin\psi \quad (3)$$

$$p' = \frac{pL}{U}, q' = \frac{qL}{U} = sin\beta, r' = \frac{rL}{U}$$

A submarine gets subjected to many different forces during operation. These forces are lift force, weight force, drag force, propeller thrust and inertia forces. Test rigs generally measure 6 force components. These forces are labeled as X, Y, Z forces and K, M, N moments on the x, y, z axes, respectively. As is known from fluid mechanics, one of the forces that produce hydrodynamic effects are viscous forces. The measurements in the tests made provide the hydrodynamic forces resulting from the viscous effects and thus the coefficients to be obtained. The movements of the submarine are shown in Figure 2 along with their names (Zhao et al., 2022).

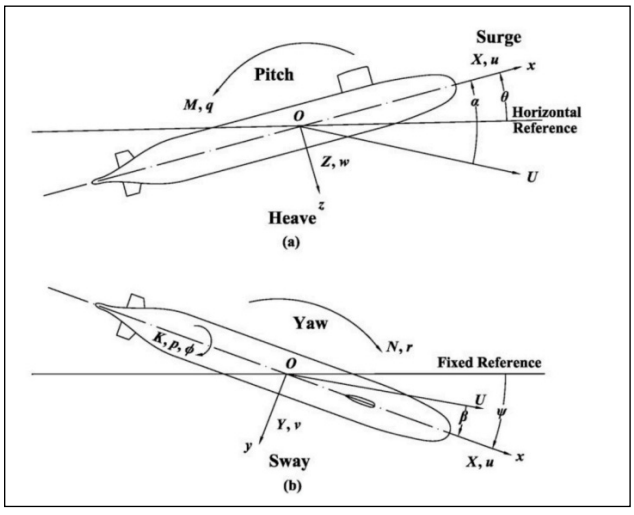

Figure 2. The motion of a submarine: (a) vertical plane; (b) horizontal plane (Zhao et al., 2022).

2.3. Maneuverability equations

Newton's second law can be used to derive equations of motion. The equations of motion with six degrees of freedom can be obtained as follows.

$$m[\dot{u} - vr + wq - x_G(q^2 + r^2) + y_G(pq - \dot{r}) + z_G(pr + \dot{q})] = F_x \quad (4)$$

$$m[\dot{v} - wp + ur - y_G(r^2 + p^2) + z_G(qr - \dot{p}) + x_G(qp + \dot{r})] = F_y \quad (5)$$

$$m[\dot{w} - uq + vp - z_G(p^2 + q^2) + x_G(rp - \dot{q}) + y_G(rp + \dot{p})] = F_z \quad (6)$$

$$I_x\dot{p} + (I_z - I_y)qr - I_{xz}(\dot{r} + pq) + I_{yz}(r^2 - q^2) + I_{xy}(pr - \dot{q}) + m[y_G(\dot{w} - uq + vp) - z_G(\dot{v} - wp + ur)] = M_x \quad (7)$$

$$I_y\dot{q} + (I_x - I_z)rp - I_{yx}(\dot{p} + qr) + I_{zx}(p^2 - r^2) + I_{yz}(qp - \dot{r}) + m[z_G(\dot{u} - vr + wq) - x_G(\dot{w} - uq + vp)] = M_y \quad (8)$$

$$I_z\dot{r} + (I_y - I_x)pq - I_{zy}(\dot{q} + rp) + I_{xy}(q^2 - p^2) + I_{zx}(rq - \dot{p}) + m[x_G(\dot{v} - wp + ur) - y_G(\dot{u} - vr + wq)] = M_z \quad (9)$$

The velocities that the submarine has during its operation are affected by the rotational velocities. These effects are expressed by the nonlinear parts of the equations. However, the assumption made in this study is that these effects are negligible. This means that the results do not take into account the resistance of cross-flows and unsteady viscous effects (Zhao et al., 2022). When the equations are arranged in line with this approach, the following equations are obtained.

Surge:

$$\frac{\rho}{2}l^4\left[X'_{qq}q^2 + X'_{rr}r^2 + X'_{rp}rp\right] + \frac{\rho}{2}l^3\left[X'_{\dot{u}}\dot{u} + X'_{vr}vr + X'_{wq}wq\right] + \frac{\rho}{2}l^2\left[X'_{uu}u^2 + X'_{vv}v^2 + X'_{ww}w^2\right] + \frac{\rho}{2}l^2u^2\left[X'_{\delta e\delta e}\delta e^2 + X'_{\delta r\delta r}\delta r^2 + X'_{\delta a\delta a}\delta a^2\right] - (W - B)\sin\theta = X \quad (10)$$

Sway:

$$\frac{\rho}{2}l^4\left[Y'_{\dot{r}}\dot{r} + Y'_{\dot{p}}\dot{p} + Y'_{p|p|}p|p| + Y'_{pq}pq + Y'_{qr}qr\right] + \frac{\rho}{2}l^3\left[Y'_{\dot{v}}\dot{v} + Y'_{vq}vq + Y'_{wp}wp + Y'_{wr}wr\right] + \frac{\rho}{2}l^3\left[Y'_{r}ur + Y'_{|r|\delta r}|r|\delta r + Y'_{v|r|}\frac{v}{|v|}\left(v^2 - w^2\right)^{\frac{1}{2}}|r|\right] + \frac{\rho}{2}l^2\left[Y'_{v}uv + Y'_{v|v|}v\left(v^2 - w^2\right)^{\frac{1}{2}}\right] + \frac{\rho}{2}l^2\left[Y'_{vw}vw + Y'_{\delta r}u^2\delta r^2\right] + (W - B)\cos\theta\sin\phi = Y \quad (11)$$

Heave:

$$\frac{\rho}{2}l^4\left[Z'_{\dot{q}}\dot{q} + Z'_{pp}pp^2 + Z'_{rr}rr^2 + Z'_{rp}rp\right] + \frac{\rho}{2}l^3\left[Z'_{\dot{w}}\dot{w} + Z'_{vp}vp + Z'_{vr}vr\right] + \frac{\rho}{2}l^3\left[Z'_{q}uq + Z'_{|q|\delta e}u|q|\delta e + Z'_{w|q|}\frac{w}{|w|}\left(v^2 + w^2\right)^{\frac{1}{2}}|q|\right] + \frac{\rho}{2}l^2\left[Z'_{w}uw + Z'_{w|w|}w\left(v^2 + w^2\right)^{\frac{1}{2}}\right] + \frac{\rho}{2}l^2\left[Z'_{|w|}u|w| + Z'_{ww}\left|w\left(v^2 + w^2\right)^{\frac{1}{2}}\right|\right] + \frac{\rho}{2}l^2\left[Z'_{vv}v^2 + Z'_{\delta e}u^2\delta e + Z'_{\delta a}u^2\delta a\right] + (W - B)\cos\theta\cos\phi = Z \quad (12)$$

Roll:

$$\frac{\rho}{2}l^5\left[K'_{\dot{p}}\dot{p} + K'_{\dot{r}}\dot{r} + K'_{p|p|}p|p| + K'_{pq}pq + K'_{qr}qr\right] + \frac{\rho}{2}l^4\left[K'_{\dot{v}}\dot{v} + K'_{r}ur + K'_{p}up\right] + \frac{\rho}{2}l^4\left[K'_{vq}vq + K'_{wp}wp + K'_{wr}wr\right] + \frac{\rho}{2}l^3\left[K'_{v}uv + K'_{v|v|}v\left(v^2 + w^2\right)^{\frac{1}{2}}\right] + \frac{\rho}{2}l^3\left[K'_{vw}vw + K'_{\delta r}u^2\delta r + K'_{\delta a}u^2\delta a\right] + \left(y_G W - y_B B\right)\cos\theta\sin\phi = K \quad (13)$$

Pitch:

$$\frac{\rho}{2}l^5\left[M'_{\dot{q}}\dot{q} + M'_{pp}pp^2 + M'_{rr}rr^2 + + M'_{rp}rp + M'_{q|q|}q|q|\right] + \frac{\rho}{2}l^4\left[M'_{\dot{w}}\dot{w} + M'_{vp}vp + M'_{vr}vr\right] + \frac{\rho}{2}l^4\left[M'_{q}uq + M'_{|q|\delta e}u|q|\delta e + M'_{w|q|}\frac{w}{|w|}\left(v^2 + w^2\right)^{\frac{1}{2}}|q|\right] + \frac{\rho}{2}l^3\left[M'_{w}uw + M'_{w|w|}w\left(v^2 + w^2\right)^{\frac{1}{2}}\right] - \frac{\rho}{2}l^3\left[M'_{|w|}u|w| + M'_{ww}\left|w\left(v^2 + w^2\right)^{\frac{1}{2}}\right|\right] + \frac{\rho}{2}l^3\left[M'_{vv}v^2 + M'_{\delta e}u^2\delta e + M'_{\delta a}u^2\delta a\right] - \left(x_G W - x_B B\right)\cos\theta\cos\phi - \left(z_G W - z_B B\right)\sin\theta = M \quad (14)$$

Yaw:

$$\frac{\rho}{2}l^5\left[N'_{\dot{r}}\dot{r} + N'_{\dot{p}}\dot{p} + N'_{r|r|}r|r| + N'_{pq}pq + N'_{qr}qr\right] + \frac{\rho}{2}l^4\left[N'_{\dot{v}}\dot{v} + N'_{vq}vq + N'_{wp}wp + N'_{wr}wr\right] + \frac{\rho}{2}l^4\left[N'_{r}ur + N'_{p}up + N'_{|r|\delta r}u|r|\delta r + N'_{v|r|}\left|\left(v^2 + w^2\right)^{\frac{1}{2}}r\right|\right] + \frac{\rho}{2}l^3\left[N'_{v}uv + N'_{v|v|}\left|v\left(v^2 + w^2\right)^{\frac{1}{2}}\right|\right] + \frac{\rho}{2}l^3\left[N'_{vw}vw + N'_{\delta r}u^2\delta r\right] + \left(x_G W - x_B B\right)\cos\theta\sin\phi - \left(y_G W - y_B B\right)\sin\theta = N \quad (15)$$

Sway force and yaw moment acting on a model can be measured by drift experiments which can be done with a submarine model. Gaining a yaw moment and sway velocity to the model creates a force and moment. The rate coefficients Y_v and N_v can be obtained with the help of the velocity versus force graphs obtained as a result of these tests repeated at different sway velocities.

2.4. The Reynolds-Averaged Navier-Stokes (RANS) Equations

ANSYS FLUENT is utilized to model the fluid dynamics surrounding Autosub, employing the incompressible and isothermal Reynolds Averaged Navier-Stokes (RANS) equations (17). This computational approach aimed to ascertain the Cartesian flow field (ui = u, v, w) and pressure (p) of the water surrounding the hull of an Autonomous Underwater Vehicle (AUV).

$$\frac{\partial \underline{U}_i}{\partial x_i} = 0 \quad (16)$$

$$\frac{\partial \underline{U}_i \underline{U}_j}{\partial x_j} = -\frac{1}{\rho}\frac{\partial P}{\partial x_i} + \frac{\partial}{\partial x_j}\left\{\nu\left(\frac{\partial U_i}{\partial x_j} + \frac{\partial U_j}{\partial x_i}\right)\right\} - \frac{\partial \overline{u_i' u_j'}}{\partial x_j} + f_i \quad (17)$$

The k-ω model is one of the most preferred turbulence models. In this problem, the "k-ω SST" model was used. The k-ω SST model employs the vortex viscosity approach to model the boundary layer, ensuring a more accurate inclusion of shear forces in the equations. Atik (2021) in her study where she investigated the static drift performance of the DARPA Suboff submarine AFF-1 configuration, stated that all turbulence models gave close results at small angles, while after 8 degrees of drift angle the SST k-ω turbulence model gave the closest results.

2.5. Presentation of Forces and Moments

To convert the acquired forces and moments into non-dimensional values, the equations 18-19 as outlined in the SNAME (1950) proposal are used. The X, Y, and Z axis resistive forces are made non-dimensional by applying the following formula.

$$X', Y', Z' = \frac{X,Y,Z}{\frac{1}{2}\rho V_0^2 L_0^2} \quad (18)$$

K, M, N are the moments that occur around the X, Y, Z axis, respectively. To make non- dimensionalization of these moments, the following formula is used.

$$K', M', N' = \frac{K,M,N}{\frac{1}{2}\rho V_0^2 L_0^3} \quad (19)$$

3. GEOMETRY OF BODIES

The Autosub autonomous submarine model has evolved from the past to the present with the advancement of technology. The National Oceanography Centre (NOC) in Wormley initiated a program to develop scientific applications for autonomous underwater vehicles. The Autosub submarine vehicle, which has multiple geometries tailored to different purposes, was designed according to its usage. The Autosub submarine has an approximate length of 7 meters and a diameter of 0.9 meters. The Autosub submarine model to be used in this study has a scale factor of 1.346. The geometric characteristics of the Autosub submarine model are provided in Table 1 (Can, 2014). The image of the created Autosub model can be seen in Figure 3 and Figure 4.

Table 1. Geometric Properties of the Autosub Model (Can, 2014)

Description	Abbreviation	Value
Length overall	L_{OA}	5.2 m
Diameter	D	0.669 m
Nose Length	L_N	1.022 m
Nose shape		Elliptic
Body Length	L_B	2.020 m
Body Cross Section Area	S_B	0.352 m^2
Aft Body Length	L_{AFT}	1.799 m
CG Distance from Nose	CG_N	2.310 m
Tail Span	B_T(Tip to Tip)	0.854 m
Tail Tip Chord Length	c	0.200 m
Sweep Angle (Leading Edge)	degrees	14.40°
Sweep Angle (Trailing Edge)	degrees	0°
Tail Airfoil		NACA0015

4. NUMERICAL CALCULATIONS

4.1 Mesh Independence Study

The aim of the mesh independence study is to create a mesh structure that would provide calculations with a reasonable level of error in terms of the conducted analyses and, at the same time, minimize the number of elements to reduce the computational cost. In line with this objective, a mesh independence study is carried out. Since experimental data for the Autosub submarine vehicle are available, the numerical results are validated with the experimental results.

4.1.1 Domain & Boundary Conditions

The dimensions of the cylindrical geometry created for the domain are as shown in Figure 5. The domain is created

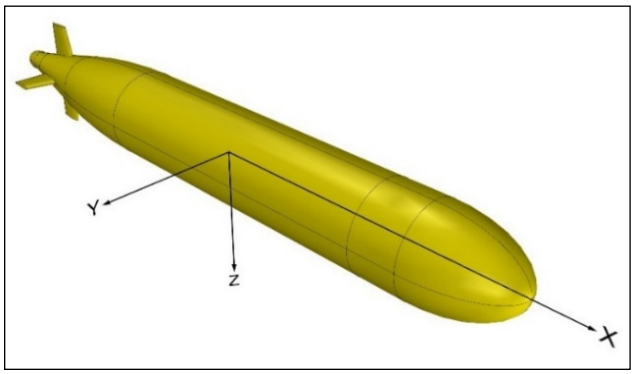

Figure 4. Autosub Geometry Perspective View.

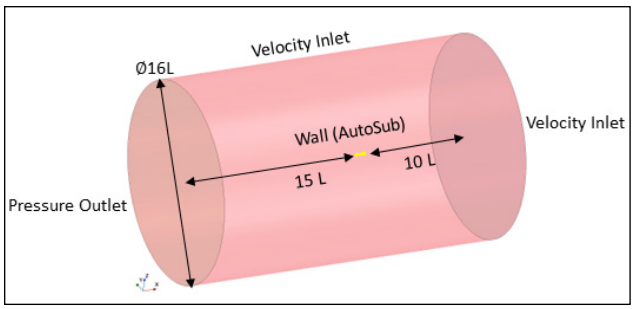

Figure 5. Boundary Conditions for the Static Drift Tests on Star CCM+

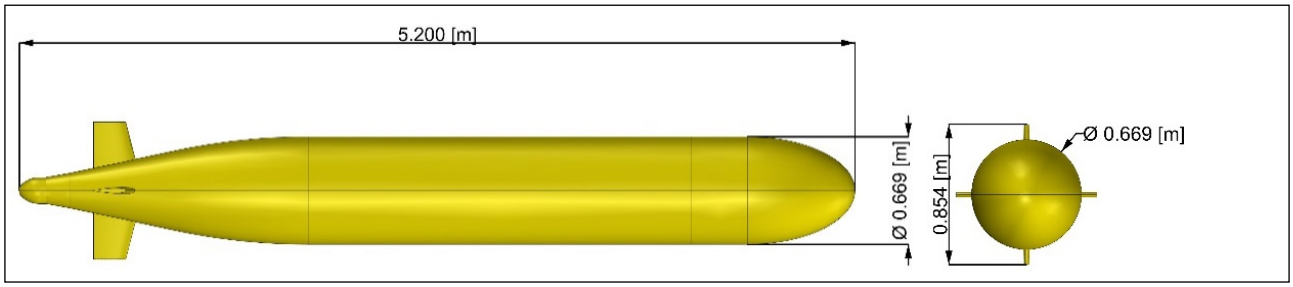

Figure 3. Autosub Geometry Top View and Back View.

with a size that is 10 times the length of the submarine at the front and 15 times at the back. In addition, the diameter of the cylinder is determined to be 16 times the length of the submarine. Velocity inlet is defined on the front surface and side surfaces of the cylindrical volume. On the back surface, a pressure outlet boundary condition is defined with a pressure value of 0 Pa. For each drift angle, a velocity vector is determined and assigned to the velocity inlet surfaces.

4.1.2 Physical Model

Steady-State RANS equations are used in all calculations. Viscous effects within the boundary layer are obtained using wall functions in the conducted analyses. In the analyses the k-ω SST turbulence model is used, the first layer thickness is created to satisfy the condition $30 < y^{+} < 300$.

To obtain the desired wall distance y+ the Equation (20) is used to calculate the thickness of the first layer.

$$\Delta y = L\Delta y^{+}\sqrt{80}R_n^{-13/14} \tag{20}$$

The calculation of the layer thickness is determined based on the Reynolds number, as given in Equation (21) (Phillips et al., 2007). A total number of 10 layers are created. The boundary layer for a blunt body can be estimated using the following equation:

$$\delta = 0.035LR_n^{-1/7} \tag{21}$$

4.1.3. Mesh Structure

In this study, five different mesh densities with varying element counts are created. Figure 6 show the volume meshes of the Autosub submarine. The element size follows an increase ratio of $\sqrt{2}$, as recommended by the ITTC (International Towing Tank Conference) guidelines. (ITTC Resistance Committee, 2017).

It can be observed that the mesh is refined near the Autosub model. This refinement aims to better solve the flow region in close proximity to the model, ensuring more accurate analysis in that area.

4.1.4 Uncertainty Study

The method that known as (GCI) Grid Convergence Index has been used on verification of the grid structure. The uncertainty analysis has been conducted for the scenario with 6-degrees drift angle. The velocity vector is calculated

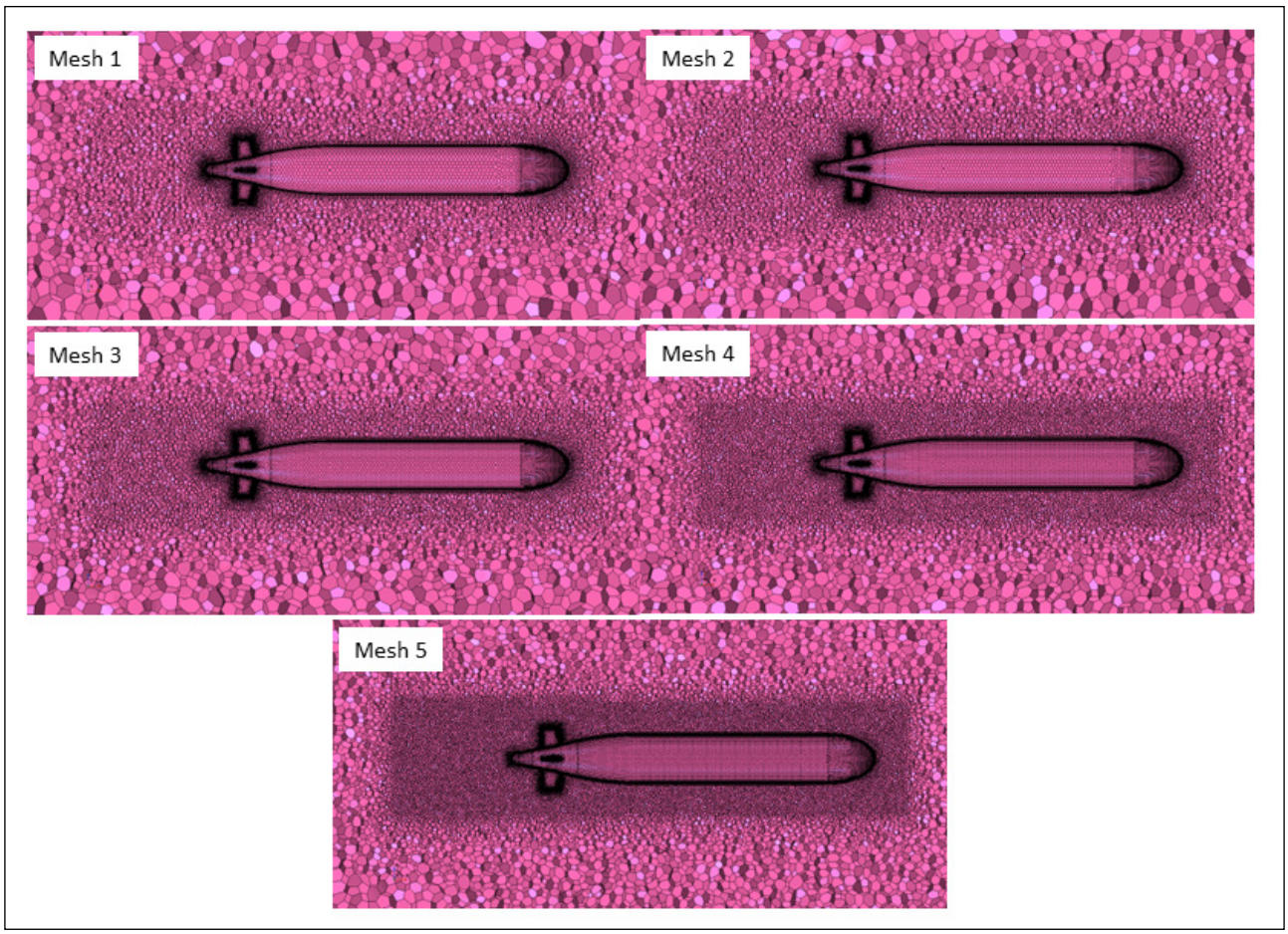

Figure 6. Mesh Structures.

Table 2. Static Drift Results for 6 degrees drift angle

6 Degrees Static Drift Results							
	Cell Number	**Y**	**Y'**	**N**	**N'**	**Error (%) Y'**	**Error (%) N'**
EXP	-	298,9826	0,003062	274,0047	0,000540	-	-
Mesh 1	794489	324,8269	0,003326	310,7741	0,000612	8,6440	13,4193
Mesh 2	1170857	319,5991	0,003273	308,1391	0,000607	6,8956	12,4576
Mesh 3	1841095	305,4607	0,003128	303,9573	0,000599	2,1667	10,9314
Mesh 4	2952064	301,7904	0,003090	302,1399	0,000595	0,9391	10,2682
Mesh 5	5639856	300,4577	0,003077	300,3557	0,000591	0,4934	9,6169

based on this angle. Table 2 presents the element count, results and deviations according to experimental results for different mesh densities. The analyses are conducted on a Windows operating system using a 4-core processor. The connection between the forces at 6 degrees of static drift and the mesh structure can be seen in Figure 7. Figure 8 shows the connection of the moments at 6 degrees of static drift with the mesh structure.

Roache (1994) presented the Grid Convergence Index (GCI) method in his study. While there are many different methods, this method focuses on mesh refinement, which is one of the important areas in CFD studies. This method, which is presented to reduce the complexity in grid refinement studies, has been used in many different studies and has been accepted by researchers. The mentioned method was edited by Celik et al. (2008) and presented again. In this study this edited method of GCI has been used as follows. Mesh size can be found by Equation (22).

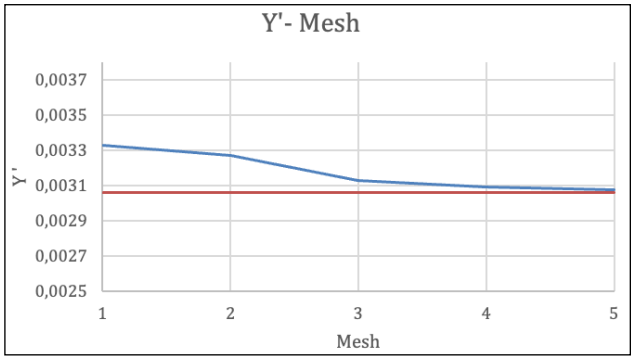

Figure 7. Sway Force Y' for drift angle 6 degrees.

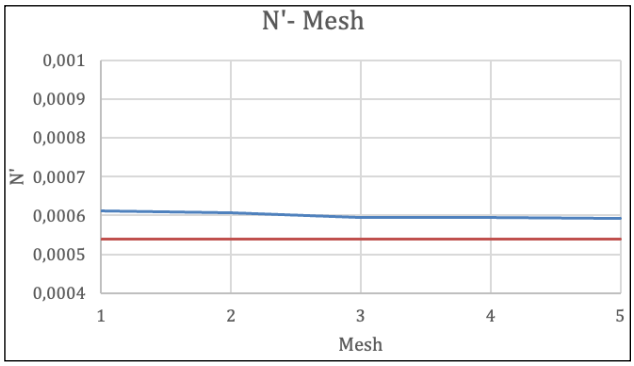

Figure 8. Yaw Moment N' for drift angle 6 degrees.

$$h = \left[\frac{1}{N}\Sigma_{i=1}^{N}(\Delta V_i)\right]^{\frac{1}{3}} \tag{22}$$

N is the number of cells and V_i is the volume of i th cell.

Grid refinement factor can be found with Equation (23). h_1, h_2 and h_3 is calculated with the help of Equation (22) for fine, medium and coarse grids, respectively.

$$r_{21} = \frac{h_2}{h_1} \; ; \; r_{32} = \frac{h_3}{h_2} \tag{23}$$

After calculating the refinement factors between fine and medium; medium and coarse, we can calculate the apparent order which is p in Equation (24).

$$p = \frac{1}{ln\ ln\ (r_{21})}\left|ln\ ln\ \left|\frac{\varepsilon_{32}}{\varepsilon_{21}}\right| + q(p)\right| \tag{24}$$

$$q(p) = ln\ ln\left(\frac{r_{21}^{p} - s}{r_{32}^{p} - s}\right) \tag{25}$$

$$s = 1 * sgn\left(\frac{\varepsilon_{32}}{\varepsilon_{21}}\right) \tag{26}$$

$$\varepsilon_{32} = \phi_3 - \phi_2 \; ; \; \varepsilon_{21} = \phi_2 - \phi_1 \tag{27}$$

ϕ_k is the solution of k th grid. That can be selected as a scalar value from a solution such as a sway force. ε_{21} and ε_{32} have been calculated with the help of the Equation (27) and these parameters used to calculation of s in Equation (26). The negative value of s means oscillatory convergence. The apparent order, p, has been calculated with the help of Equation (24) and (25). As can be seen in equation (24) there is a function related to p, which is $q(p)$, in equation p. For this reason, an initial estimate was made while calculating p, and p was found iteratively.

$$R = \frac{\varepsilon_{21}}{\varepsilon_{32}} \quad (28)$$

The convergence factor R can be obtained with the help of Equation (28).

$$\phi_{ext}^{21} = \frac{\left(r_{21}^{p}\phi_1 - \phi_2\right)}{r_{21}^{p} - 1} \quad (29)$$

ϕ_{ext}^{21} in Equation (29) is extrapolated scalar value of selected ϕ.

$$e_a^{21} = \left|\frac{\phi_1 - \phi_2}{\phi_1}\right| \quad (30)$$

Table 3. Spatial Uncertainty

	Sway Force (Y) [N]	Yaw Moment (N) [N-m]
N_1	5639856	
N_2	2952064	
N_3	1841095	
N_4	117085	
N_5	794489	
r_{21}	1,2433	
r_{32}	1,1605	
ϕ_1	300,4577	300,3557
ϕ_2	301,7904	302,1399
ϕ_3	305,4607	303,9573
p	5,5636	1,7453
R	0,3631	0,9817
ϕ_{ext}^{21}	299,8925	296,4963
e_a^{21}	0,44%	0,59%
e_{ext}^{21}	0,19%	1,3%
GCI_{mesh5}^{21}	0,24%	1,6%

$$e_{ext}^{21} = \left|\frac{\phi_{ext}^{21} - \phi_1}{\phi_{ext}^{21}}\right| \quad (31)$$

e_a^{21} is the approximate error while e_{ext}^{21} is extrapolated error.

$$GCI_{fine}^{21} = \frac{1.25 * e_a^{21}}{r_{21}^{p} - 1} \quad (32)$$

The Grid Convergence Index (GCI) can be found with Equation (32).

Uncertainty analysis results are given in Table 3. When the data in Table 2 and Figures 7 and 8 are examined, it is seen that the error rate stabilized after Mesh 4. The number of cells, which directly affects the computational cost, increases approximately 1.9 times between Mesh 4 and Mesh 5. The solution time is significant in terms of computational cost, since the selected mesh will be used in the analyses which will be done in the next part of the study. Considering the capacity of the computer used, the change in the error rate was ignored and Mesh 4 was chosen.

5. RESISTANCE ANALYSES

The full-scale geometry of the 7m length submarine is used in the resistance analyses. The mesh sizes used in the resistance analyses are the same as those obtained from the Mesh 4 mesh structure in the mesh independence study conducted for static drift analyses. The flow volume is recreated to be proportional to the full-scale size. As a result, there is an increase in the number of meshes. Four different analyses are conducted at speeds of 0.5, 1.0, 1.5, and 2.0 m/s. The results of these analyses can be seen in the Table 4 and Figure 9. The velocity distribution around the Autosub geometry can be seen in Figure 10.

As can be seen in Table 4, the empirical results presented by Phillips et al. (2007) do not match with the test results performed by Fallows (2004). In the experiment conducted by Fallows (2004), the 2.5 m. length model was drawn from the water surface at a depth of 2.6 diameter. This means that the submarine is close to the water surface and produces waves (Phillips et al., 2009). In addition, a model

Table 4. Resistance Results

Velocity (m/s)	EXP (Fallows)	EXP (Kimber)	Empirical (Phillips et al.)	CFX (Phillips et al.)	CFD	Error % Empirical	Error % CFX
0,5	10,337	-	9,003	8,943	9,175	1,912	2,589
0,75	-	-	18,061		-		
1	18,023	-	30,663	31,959	31,873	3,941	-0,270
1,25	58,064	-	45,886		-		
1,5	100,017	-	64,242	67,926	67,328	4,801	-0,881
1,75	-	-	84,898		-		
2	-	126,6494	108,228	115,531	114,376	5,683	-1,001

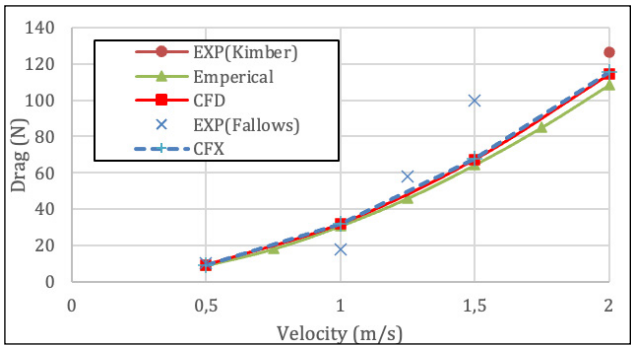

Figure 9. Comparisons of resistance predictions for Autosub (Phillips et al., 2007).

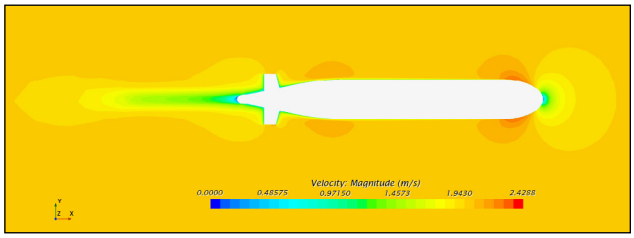

Figure 10. Velocity Magnitude for Resistance.

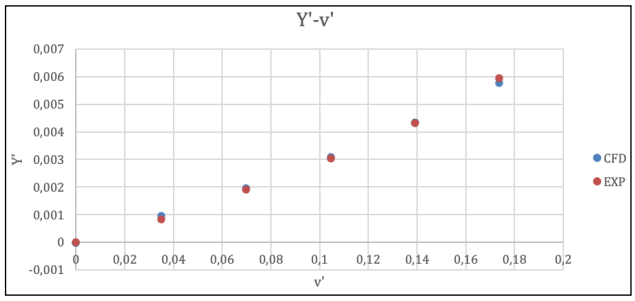

Figure 11. Variation of Sway Force (Y') with Sway Velocity (v').

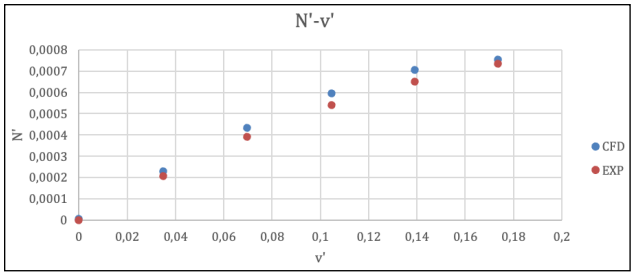

Figure 12. Variation of Yaw Moment (N') with Sway Velocity (v').

with a length of 2.5 meters was used in the experiment. As the speed increases, the increase in the margin of error supports that the factor causing this difference is the wave resistance. In the thesis published by Fallows, these problems related to the test setup were mentioned. Another cause of error is the presence of a large mounting post on the test setup. The forces caused by this structure affected the test results. These reasons are the causes for the difference between experimental results (Fallows, 2004), CFD results and empirical results. On the other hand, the CFD result for 2m/s agrees with the experimental results from Kimber&Marshfield (1993) with an error rate of %10. Also, the CFD results have error rates less than %6 with the empirical results (Phillips et al., 2007). In addition to these the results match with the CFX solution made by Phillips et al. (2007) with an error rate of less than %2,6.

6. STATIC DRIFT ANALYSES

Six further analyses are performed for the static drift condition at angles of 0, 2, 4, 6, 8, and 10 degrees, with a velocity of 2.69 m/s. The obtained results are compared with the experimental data from Kimber&Marshfield (1993). Static drift results are presented in Table 5. The hydrodynamic sway force Y' and yaw moment N' are presented in Figure 11 and 12.

Figures 13, 14, 15, and 16 show the results obtained from the CFD analysis. The highest and lowest values in the obtained results differ by changing the static drift angle. However, to provide a comparative result, the velocity and pressure range are limited to a single value for each figure.

Figure 13 shows the flow field around the submarine. It is seen that the characteristic of the flow around the submarine changes as the static drift angle increases.

Table 5. Static Drift Results

AoA	v' (Sway Velocity)	Y'	N'	Y'(EXP)	N'(EXP)	Error (%) Y'	Error (%) N'
0	0	-1,2E-05	5,85E-06	0	0	-	-
2	0,0348995	0,00095	0,000231	0,000836	0,000206	13,65061	12,14809
4	0,0697565	0,001969	0,000433	0,001913	0,000391	2,928268	10,677273
6	0,1045285	0,00309	0,000595	0,003032	0,00054	1,910778	10,268147
8	0,1391731	0,004343	0,000707	0,004305	0,000652	0,877556	8,4381988
10	0,1736482	0,005769	0,000756	0,005931	0,000734	-2,73295	2,8820465

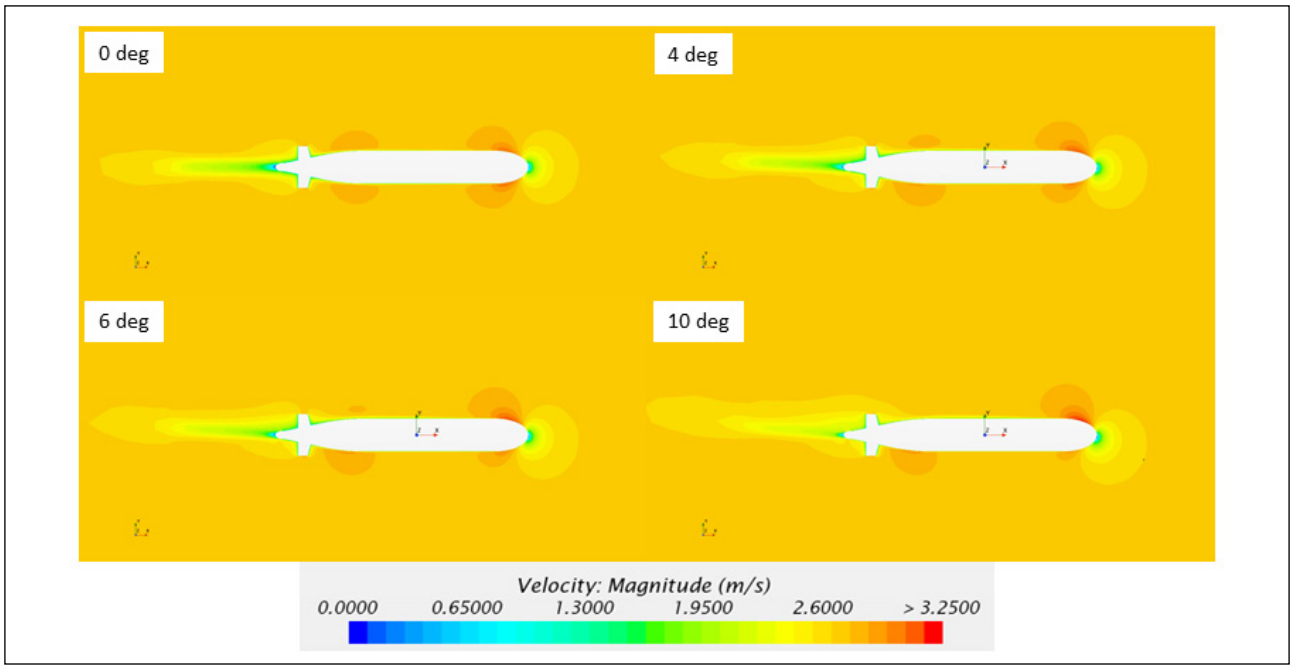

Figure 13. Velocity Distribution Around the Submarine.

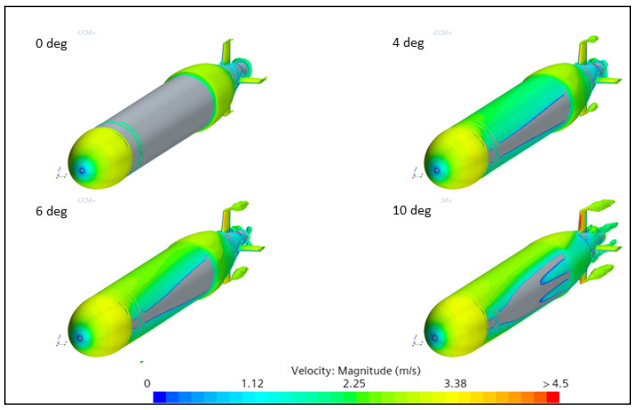

Figure 14. Q Criteria = 5 Surfaces Around the Submarine.

Surfaces with a Q-Criteria value equal to 5 were obtained. The velocity distribution on these surfaces is shown in Figure 14. The Q-Criteria value allows us to examine the wake behind the submarine. As can be seen, as the angle increases, the maximum velocity obtained increase, and the angle of the wake and length of the wake also increases.

Figure 15 shows the streamline drawn from the submarine surfaces. When the submarine is subjected to a static drift angle, a rotational flow is observed around it. As this angle increases, it is seen in the figures that the streamlines in the rear part of the submarine are more complex and have higher velocity.

Figure 16 shows the fins in the aft body of the submarine. The pressure distribution over these fins changes as the angle changes. As the angle increases, the region of

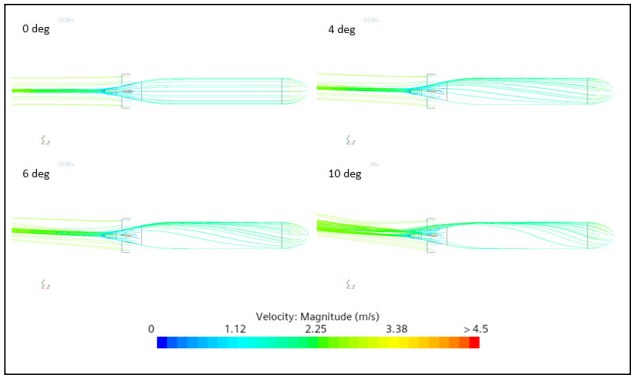

Figure 15. Streamlines Around the Submarine.

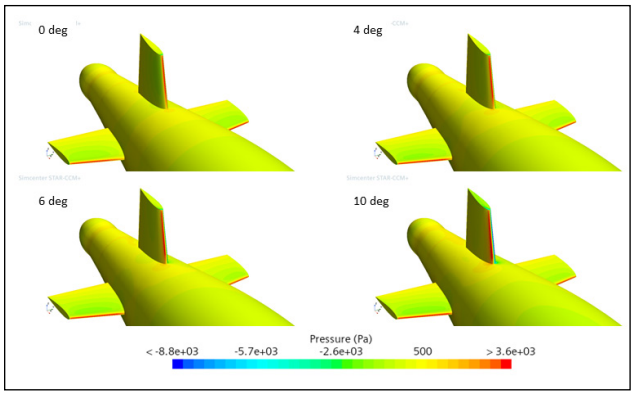

Figure 16. Pressure Distribution on Aft Body of Submarine.

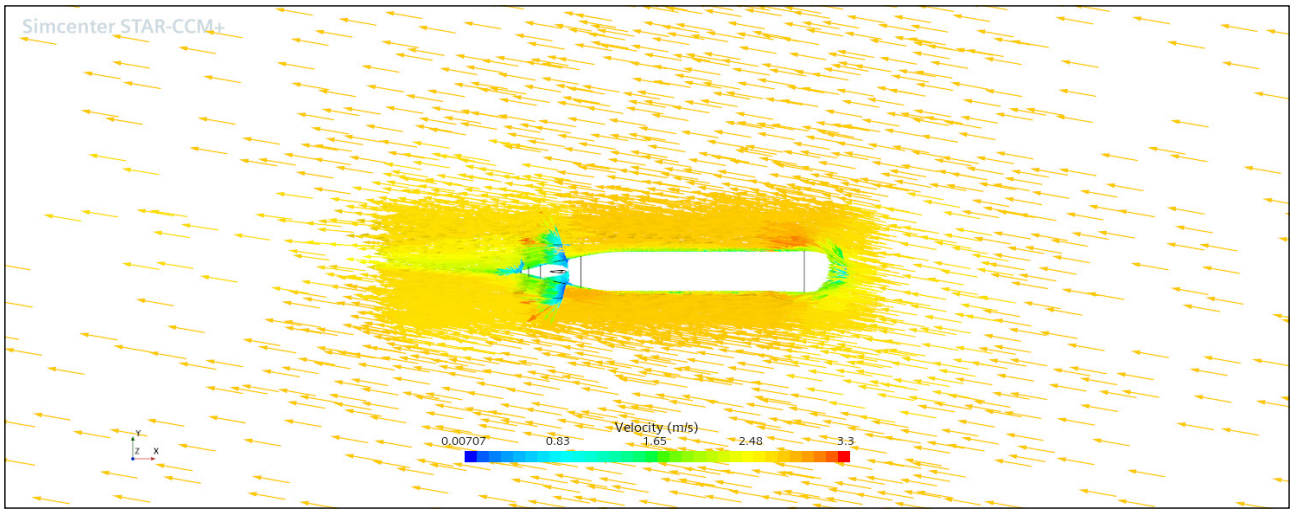

Figure 17. Vector Field Around the Submarine.

maximum pressure on the fin is displaced. This causes an increase in the force created by the fins as the angle increases. This effect is one of the reasons why the yaw moment increases as the angle increases.

The vector field around the submarine is shown in Figure 17. In this image given for the 10-degree static drift condition, the angle of the flow acting on the submarine is clearly seen. The resulting sway force and yaw moment are caused by the flow of the body acting at a certain angle. It is seen that it reaches 3.3 m/s in the cross section of this image performed at a speed of 2.69 m/s. These velocity zones affect the pressure zones around the submarine, causing sway force and yaw moment to occur.

When comparing the force and moment values obtained through CFD with experimental results, it is observed that the error rates vary between -5% and 10% (Table 5). The results (Figure 11 and Figure 12) presented show that the sway forces and yaw moments obtained from the analyze give independent results from the mesh structure and are in consistency with the experimental results presented in the literature. As a result, an analysis method that can be used in future studies has been presented.

7. CONCLUSIONS

This study involves the force and moment calculations of the Autosub submarine using model and full-scale geometries. The RANS equations and two-equation turbulence models are employed in the calculations. Static drift analyses are conducted for angles of 0, 2, 4, 6, 8, and 10 degrees. The calculations are performed at a cruising speed of 2.69 m/s using a scale factor of 1.346. To determine the optimum mesh structure, a mesh independence study is carried out at 6 degrees static drift angle. The error rates of the experimental results and the calculated values in the analysis are used in the mesh independence study. After determining the optimum mesh structure with the help of the uncertainty analyses and the mesh independence study, the analyses are completed for other angles and compared with the experimental results.

Full-scale resistance analyses are conducted using the same mesh sizes. Resistance analyses are performed for the 7m full-scale geometry at velocities of 0.5, 1.0, 1.5, and 2.0 m/s. The calculated resistance forces are compared with the experimental results. There are two experimental results for resistance presented in the open literature. In the first presented by Kimber&Marshall (1993) a resistance value for 2 m/s is available, while Fallows (2004) presented the resistance values for a larger range. The experimental results of Fallows cover speeds ranging from 0 to 5 m/s for different model depths so that the wave resistance is also included in the values. So, there is a deviation from the experimental results comparing to CFD, empirical and also experimental result obtained before by Kimber&Marshall (1993). The cause of this deviation is also discussed by Phillips et al. (2007). The CFD results of the present study appear to be in good agreement with the CFD results presented by Phillips et al. (2007), as well as the experimental results by Kimber & Marshall (1993), with an error rate of 2.6% and 10%, respectively.

The static drift analyses are conducted for different drift angles and a good agreement is seen with the experimental results conducted by Kimber&Marshall (1993). While the deviation from the experimental results is lesser in the sway forces more deviation is seen for the yaw moment. However, the deviation is in an acceptable level since 10 % of deviation is seen.

The force and moment values obtained from the static drift and resistance analyses are found to be consistent with the experimental and empirical results available in the literature with an error ratio of %0.8-%13.5 and %1.9-%5.6, respectively.

It is seen that the pure sway forces and pure yaw moments can be obtained with high accuracy with CFD methods. The mesh independence study and the validation study show that the numerical results are consistent with the experimental results. This shows that the method used in this study can be used for the predictions of hydrodynamic coefficients for static drift condition. In future studies the method will be used for derived geometries of the Autosub submarine for different L/B ratios.

DATA AVAILABILITY STATEMENT

The published publication includes all graphics and data collected or developed during the study.

CONFLICT OF INTEREST

The author declared no potential conflicts of interest with respect to the research, authorship, and/or publication of this article.

ETHICS

There are no ethical issues with the publication of this manuscript.

FINANCIAL DISCLOSURE

The authors declared that this study has received no financial support.

REFERENCES

Abkowitz, M. A. (1964). *Lectures on Ship Hydrodynamics Steering and Maneuverability Technical Report. Hydro and Aerodynamic Laboratory, Lyngby, Denmark*. Technical Report Hy-5.

Ackermann, S. (2008). *Prediction of Suboff Hydrodynamics using ANSYS CFX Software. Launceston.* National Centre of Maritime Engineering and Hydrodynamics.

Alin, N., Bensow, R., Fureby, C., & Huuva, T. (2010). Current Capabilities of DES and LES for Submarines at Straight Course. *Journal of Ship Research, 54*, 184–196.

Arslan, S. (2013). Su altı araçları için yeni geliştirilen hidrodinamik modelleme yöntemleri kullanılarak otonom bir su altı aracının hidrodinamik karakteristiğinin incelenmesi. [Master Thesis]. Istanbul Technical University.

Atik, H. (2021). Türbülans modellerinin DARPA SUBOFF statik sürükleme testi üzerinden incelenmesi. *Gazi Üniversitesi Mühendislik-Mimarlık Fakültesi Dergisi, 3,* 1509–1522. [CrossRef]

Bull, P. (1996). *The validation of CFD predictions of nominal wake for the SUBOFF fully appended geometry.* 21st Symposium on Naval Hydrodynamics, Trondheim, Norway, 1061–1076.

Can, M. (2014). *Numerical simulation of hydrodynamic planar motion mechanism test for underwater vehicles* [Master Thesis]. The Graduate School of Natural and Applied Sciences of Middle East Technical University.

Cardenas, P., & de Barros, E. A. (2019). Estimation of AUV Hydrodynamic Coefficients Using Analytical and System Identification Approaches. *IEEE Journal of Oceanic Engineering, 1–20.*

Carrica, P. M., Kerkvliet, M., Quadvlieg, F., & Martin, J. E. (2016). *CFD Simulations and Experiments of a Maneuvering Generic Submarine and Prognosis for Simulation of Near Surface Operation.* 31st Symp. Nav. Hydrodyn. (ONR), Monterey, CA, 11–16.

Carrica, P. M., Kim, Y., & Martin, J. E. (2019). Near-surface self propulsion of a generic submarine in calm water and waves. *Ocean Engineering, 183,* 87–105. [CrossRef]

Celik, I., Ghina, U., Roache, P., Fretias, C.J., & Raad, H.C.P.E. (2008). Procedure for estimation and reporting of uncertainty due to discretization in CFD applications. *Journal of Fluids Engineering, 130*(7), Article 078001. [CrossRef]

Chase, N., & Carrica, P. M. (2013). Submarine propeller computations and application to self-Propulsion of DARPA suboff, *Ocean Engineering, 60,* 68–80. [CrossRef]

Crook, L.B. (1990). *Resistance for DARPA SUBOFF as Represented by Model 5470.* DTRC/SHD-1298-07.

Davidson, K. S. M., & Schiff, L. I. (1946). Turning and course keeping qualities. *Trans Soc Nav Archit Mar Eng*, 54.

Duman, S., Sezen, S., & Bal, S. (2018). *Propeller Effects on Maneuvering of a Submerged Body. A. Yücel Odabaşı Colloquium Series 3 rd International Meeting - Progress in Propeller Cavitation and its Consequences: Experimental and Computational Methods for Predictions.* 15th – 16th November, Istanbul, Turkey.

Efremov, D. V., & Milanov, E. M. (2019). Hydrodynamics of DARPA SUBOFF submarine at shallowly immersion conditions. In: TransNav: *International Journal on Marine Navigation and Safety of Sea Transportation, 13*, 2. [CrossRef]

Fallows, C. D. (2004). Characterization of the propulsion system of autonomous underwater vehicles. [Doctorial dissertation]. University of Southampton.

Fell, B. J. (2009). *Structured Mesh Optimization and CFD Simulation of the Fully Appended DARPA Suboff Model* [Master Thesis]. University of Tasmania, National Centre for Maritime Engineering and Hydrodynamics.

Gertler, M., Hagen, G. (1967). *Standard equations of motion for submarine simulation.* Technical Report AD653861, [CrossRef]

Groves, N.C., Huang, T.T., & Chang, M.S. (1989). *Geometric Characteristics of Darpa Suboff Models, David Taylor Research Center, Ship Hydromechanics* Department, Report Number DTRC/SHD-1298-01.

ITTC Resistance Committee. (2017). *Uncertainty analysis in CFD Verification and validation methodology and procedures.* ITTC - Recomm. Proced. Guidel., p. 1–13.

Joung TH., Sammut, K., He, F., & Lee, SK. (2012). Shape optimization of an autonomous underwater vehicle with a ducted propeller using computational fluid dynamics analysis. *International Journal of Naval Architecture and Ocean Engineering, 4,* 44–56. [CrossRef]

Kahramanoglu, E. (2023). Numerical investigation of the scale effect on the horizontal maneuvering derivatives of an underwater vehicle. *Ocean Enginering, 272*, Article 113883. [CrossRef]

Kırıkbaş, O, Kınacı, Ö. K., & Bal, Ş. (2021a). Sualtı araçlarının manevra karakteristiklerinin değerlendirilmesi-i: manevra analizlerinde kullanılan yaklaşımlar. *GMO Journal of Ship and Marine Technology, 219,* 6–58.

Kırıkbaş, O, Kınacı, Ö. K., & Bal, Ş. (2021b). Su altı araçlarının manevra karakteristiklerinin değerlendirilmesi-ii: akışkan sınırlarının etkileri. *GMO Journal of Ship and Marine Technology, 220*, 135–174. [CrossRef]

Kimber, N., & Marshfield, W. (1993). *Design and testing of control surfaces for the autosub demonstrator test vehicle*. Technical report, DRA Haslar.

Liu, H., & Huang, T. (1998). *Summary of DARPA SUBOFF experimental program data.* Report No. CRDKNSWC/HD-1298-11. [CrossRef]

Mackay, M. (1988). *Flow Visualization Experiments with Submarine Models in a Wind Tunnel, Defence Research Establishment Atlantic*. Technical Memorandum 88/204.

McDonald, H., Whitfield, D. (1996). *Self-propelled maneuvering underwater vehicles.* 21st Symposium on Naval Hydrodynamics, Trondheim.

Phillips, A., Furlong, M., &Turnock, S.R. (2007). *The use of Computational Fluid Dynamics to Determine the Dynamic Stability of an Autonomous Underwater Vehicle.* file:///Users/kareyayincilik11/Downloads/The_use_of_Computational_Fluid_Dynamics_to_Determi%20(1).pdf [CrossRef]

Phillips, A., Furlong, M., & Turnock, S.R. (2010). *Virtual planar motion mechanism tests of the autonomous underwater vehicle autosub*. STG-Conference / Lectureday "CFD in Ship Design", 2007.

Phillips, A., Furlong, M., & Turnock, S. R. (2011). The use of computational fluid dynamics to aid cost-effective hydrodynamic design of autonomous underwater vehicles. *Sage Journals, 224*(4), 239–254. [CrossRef]

Roache, P. J. (1998). Verification of codes and calculations. *AIAA Journal, 36(5),* 696–702. [CrossRef]

Roddy, R.F. (1990). *Investigation of the Stability and Control Characteristics of Several Configurations of the DARPA SUBOFF Model (DTRC 5470) from Captive-Model Experiments.* DTRC/SHD-1298-08.

Saeidinezhad, A., Dehghan, A. A., & Manshadi, M. D. (2015). Experimental investigation of hydrodynamic characteristics of a submersible vehicle model with a non-axisymmetric nose in pitch maneuver. *Ocean Engineering, 100,* 26–34. [CrossRef]

SNAME. (1950). *Nomenclature for treating the motion of a submerged body through a fluid* (Technical and Research Bulletin No. 1–5). SNAME.

Thomas, R. (2003). *Performance evaluation of the propulsion system for the autonomous underwater vehicle C-scout* [Unpublished Master Thesis]. Faculty of Engineering and Applied Science Memorial University of Newfoundland.

Thomas, R., Bose, N., & Williams, D. (2003). Propulsive Performance of the Autonomous Underwater Vehicle C-Scout. OCEANS 2003, San Diego, ABD.

Toxopeus, S., & Vaz, G. (2009). *Calculation of Current or Maneuvering Forces using a Viscous-Flow Solver. In Proceedings of OMAE2009*, Honolulu, Hawaii, USA. [CrossRef]

Vaz, G., Toxopeus, S., & Holmes, S. (2010). *Calculation of Maneuvering Forces on Submarines Using Two Viscous-Flow Solvers'*, OMAE 2010, Shanghai, China. [CrossRef]

Zhao, B., Yun, Y., Hu, F., Sun, J., Wu, D., & Huang, B. (2022). Hydrodynamic coefficients of the DARPA SUBOFF AFF-8 in rotating arm maneuver: Part I: Test technology and validation. *Ocean Engineering, 266*, Article 113148. [CrossRef]

Wu, C. S., He, S. I., Zhu, D. X., & Min, G. (2006). Numerical simulation of microbubble flow around an axisymmetric body. *Journal of Hydrodynamics, 18*(3), 217–222. [CrossRef]

Seatific, Vol. 3, Issue. 2, pp. 85–88, December 2023

Seatific Journal
https://seatific.yildiz.edu.tr
DOI: https://doi.org/10.14744/seatific.2023.0009

Seatific

Research Article

"Force Majeure", extension of time clauses and the prevention principle in shipbuilding contracts

Zoran TASIC*

Legal Department of Global Offshore Engineering, Split, Croatia

ARTICLE INFO

Article history
Received: January 23, 2023
Revised: December 02, 2023
Accepted: December 12, 2023

Key words:
Shipbuilding contract; delivery; force majeure; extension of time; prevention principle; causation; notices; shipyard; buyer

ABSTRACT

Under English law, it is entirely up to the contract parties to agree on "force majeure" events that are beyond the builder's control. Under an old English law principle known as the "prevention principle", no party to a contract should be allowed to benefit from its own failure to perform. In the context of shipbuilding contracts, this principle should give protection to a shipyard in the case of delays in the delivery of a vessel that are caused by the buyer's defaults. It is the builder's fundamental duty to deliver the vessel to the buyer on the delivery date set out in the shipbuilding contract. If the builder demands to be released from that duty, it will have to follow certain requirements imposed by English law.

Cite this article as: Tasic Z. "Force Majeure", extension of time clauses and the prevention principle in shipbuilding contracts. Seatific 2023;3:2:85–88.

1. INTRODUCTION

One of the most common disputes arising under shipbuilding contracts relates to delays in the delivery of a vessel.

The fundamental obligation of each shipyard is to deliver within the contract time a vessel in a condition that complies with the contract. Subject to certain conditions, set out in this article, the fixed contract time or delivery date can be postponed, suspended or extended only for the following reasons:

- The occurrence of one or more of the events set out in the shipbuilding contract as "force majeure" events that have actually caused a delay in construction and/or delivery of the vessel; and/or
- The application of the extension of time clauses set out in the shipbuilding contract; and/or
- The application of the prevention principle.

Since the shipyard's fundamental obligation is to deliver the vessel on the delivery date set out in the shipbuilding contract, the burden of proof that the shipyard is entitled to be exempted from such contractual liability, for any of the above reasons, lies with the shipyard.

English law governs most international shipbuilding contracts. Disputes arising from such contracts are usually referred to LMAA arbitration in London. This is because English law and so-called "legal London" are the most common choice of law in international shipbuilding contracts.

The shipbuilding contract under English law is a complex sales agreement with elements of a building contract (Stocznia Gdanska S.A. v. Latvian Shipping Co. and Others, 1998).

2. "FORCE MAJEURE"

Unlike European continental laws, English law does not recognise "force majeure" as a doctrine of law. "Force majeure" provisions are normally included in a clause

*Corresponding author.
*E-mail address: zorantasic2907@gmail.com

of the shipbuilding contract governing situations in which the shipyard would not be liable for delays in the construction and/or delivery of the vessel and it would be entitled to extend the period of construction and the agreed date of delivery.

It is entirely up to the shipyard and the buyer to agree upon the events that are beyond the shipyard's control and that could not be foreseen or anticipated before or at the time the contract is executed and which might cause delays in the construction and/or delivery of a vessel.

Such events normally include war or warlike events, terrorist attacks, riots, the imposition of embargoes, actions by the government with jurisdiction over the shipyard prohibiting or preventing the shipyard from proceeding with its business activities, extraordinary weather conditions, strikes, lockouts, explosions, fires, disruptions of power supplies, defects in materials and equipment, etc.

However, the shipyard will have to prove that the "force majeure" event has actually caused delays in the construction and/or delivery of the vessel (Jerram Halkus Construction Ltd v. Fenice Investments Inc., 2011).

3. EXTENSION OF TIME CLAUSES

Examples of extension of time clauses (permissible delays) in a shipbuilding contract:[1]

- The buyer's late payment of the contract price:

"*The Builder has the right to extend the Delivery Date of the Vessel for the same number of days equal to the delay in the payment of any Instalment, or a part of thereof.*" This is a good example of automatic extension without the need to show or argue causation between the buyer's delay and the extended delivery date of the vessel.

- Buyer's modifications:

"*If the dispute (about the Buyer's modifications) is resolved in favour of the Builder, any time lost due to the dispute shall be deemed a permissible delay.*"

Or

"*Any time lost in achieving an agreement regarding any modifications, deletions or additions (including the consequences of the same) … shall be deemed as permissible delay under this Contract.*"

- Buyer's supplies:

"*Should the Buyer fail to deliver any of the Buyer's Supplies within the time designated, the Delivery Date shall be automatically extended for a period of such delay in delivery.*"

Extensions of time are rarely or never as automatic as they seem as they are usually subject to certain conditions: primarily, causation and notice to the buyer, save for the suspension of construction and the extension of the delivery date due to delays in payment of the contract price.

4. CAUSATION

It is always a question of fact whether a relevant event has caused or is likely to cause delay to the works beyond the completion date. Causation is not always easy to prove and very often shipbuilding experts are involved to assist the arbitrators, or commercial judges, as the case may be, to determine whether the shipyard's claim for extension stands.

In Adyard Abu Dhabi LLC v. SD Marine Services (2011), the Court has considered whether the changes in design of the vessel demanded by the buyer caused the delay in delivery as alleged by the shipyard. It was established that the construction of the vessel was already before that in delay and the shipyard was not entitled to additional time because the alleged demands did not cause delay in delivery. What has caused delay in delivery was concurrent delay in the vessel's construction caused by the shipyard.[2]

It is a difficult task for the shipyard to demonstrate the impact of a delay on the delivery date. It should bear in mind that it is usually easier for the buyer to reject the shipyard's claim for permissible delay than for the shipyard to support its case.

5. NOTICE OF DELAY

It is common practice for every buyer to expect the shipyard to advise him of any new, extended delivery date. Shipbuilding contracts normally require the shipyard to notify the buyer in writing of the occurrence of such an event, within a number of days of the occurrence of the event. The shipyard is required to indicate the likely duration thereof. The shipyard should notify the buyer when the event or events have ceased to exist, and about the number of days of delay in the vessel's delivery caused by the occurrence of the event. The shipyard should also set out a new delivery date (BIMCO, n.d.).

However, if the shipyard demands that the contractual delivery date be extended, postponed or suspended due to the occurrence of a "force majeure" event, it will have to prove that such an event is the cause of the delay in the construction and/or delivery of the vessel. It will need to prove that the alleged event is in the critical path of construction and/or delivery of the vessel for a number of days beyond the agreed delivery date. In addition, the shipyard will need to prove that it has done all it can to avoid or minimise the actual delay in the delivery of the vessel.

Such a written notice to the buyer is a condition precedent to the application of the extension of time provisions in the shipbuilding contract.

In this context, the buyer has the right to know when the vessel will be delivered. The buyer is also entitled, where appropriate, to reject the shipyard's notice of delay. The rejection of the shipyard's notice of delay is very common. In such circumstances, the question of whether or not the

[1] https://www.bimco.org/Contracts-and-clauses/BIMCO-Contracts/NEWBUILDCON#

[2] https://www.bailii.org/ew/cases/EWHC/Comm/2011/848.html adyard-abu-dhabi-v-sds-marine-services/.

notice itself and the shipyard's claim for an extension of time are valid should be referred to arbitration in London.

By sending a written notice of delay to the buyer, the shipyard seeks to reserve its right to exclude or limit its liability for delays in the construction and/or delivery of the vessel.

However, sending a notice of delay is not enough for the shipyard to exclude or limit its liability for delays in the construction and/or delivery of the vessel. The application of extension of time provisions is normally subject to the provision of a notice by the shipyard to the buyer of the shipyard's intention to claim an extension of the delivery date.

In the above said Adyard Abu Dhabi LLC v SD Marine Services (2011), the shipyard failed to send a notice to the buyer claiming an extension of time due to the buyer's alleged acts of prevention. It was noted that "*a shipyard seeking extra time must be sure to give notices where these are contractually required*". In this case, the shipyard's claim for an extension of time failed due to its failure to give a notice of delay pursuant to the terms of the shipbuilding contract.[3]

In Zhousan Jinhaiwan Shipyard Co. v Golden Exquisite and Others (2014), delays caused by the buyer were governed by extension of time clauses in the form of permissible delays, providing the shipyard send a notice at the commencement and at the end of such delays. Since the shipyard failed to send such a notice it lost the right to claim delays allegedly caused by the buyer. Judge Leggatt stated: "*Delays in construction are prima facie the responsibility of the Builder, unless they are excused by a provision of the contract. The basic default position under the contract, in other words, is that delay is 'non-permissible' unless a term of the contract classifies it as permissible (or, in the case of excluded delays, deems it not to be delay at all)*".

The notice of delay should be given to the buyer even if it is not initially clear whether there is an impact on the delivery date. This will provide useful evidence in any future arbitration. Otherwise, the shipyard faces the risk that it would not be allowed to rely on extension of time provisions and the prevention principle will not be applicable.

Regardless of whether or not the extension of a delivery date is automatic, every court would expect a shipyard to advise its buyer of any new, extended contractual delivery date.

6. THE PREVENTION PRINCIPLE

"Prevention" means the action of stopping something from happening.

Lord Ellenborough CJ nicely set out the prevention principle in the case of Rode v Farr (1817, pp. 124–125):[4]

If the buyer has by its own wrongdoing prevented the shipyard from tendering the vessel for delivery on a contractual delivery date, the buyer should not be entitled to claim liquidated damages or cancel the shipbuilding contract and claim a refund, interest and damages. This is because in such a case the contractual date of delivery becomes "time at large".

"Time at large" is, subject to contract, a matter of law that replaces the contractual delivery date by an implied obligation to deliver the vessel within a reasonable period of time "in the light of all relevant circumstances" (Shawton Engineering v. DGP International Ltd., 2005).

In the case of Multiplex Constructions UK Ltd. v. Honeywell Control Systems Ltd. (2007), the court held:

If the buyer interferes with the work so as to delay its completion, this is an act of prevention and the contractor is no longer bound by the strict requirements of the contract as to time; for example, the instruction of variations to the work can amount to an act of prevention.

The ultimate consequence: no liquidated damages and time for the completion of the vessel's construction becomes time at large.

7. EXTENSION OF TIME CLAUSES AND THE PREVENTION PRINCIPLE

The application of the prevention principle can be excluded by the inclusion of extension of time provisions in the shipbuilding contract either in the form of permissible delays allowing the shipyard to extend the delivery date or in the form of provisions adjusting the date of completion in the event of modifications to the technical specification.

This was confirmed in the case of Multiplex v. Honeywell (2007). The prevention principle does not apply if the contract provides for an extension of time in respect of the relevant events. In addition: "Acts of prevention by an employer do not set time at large if the contract provides for an extension of time in respect of those events."

There is no need for the application of the prevention principle if the contract already protects the shipyard.

This is because the shipyard is entitled to rely on such provisions only where it can prove that the project was not already in a critical delay before the buyer's delaying conduct occurred.

The shipyard should be able to prove that without prevention by the buyer it is still possible to complete the vessel by the agreed date in spite of the shipyard's own delays.

In the case of Jerram Halkus Construction Ltd. v. Fenice Investments Inc. (2011), Judge Coulson expressed his views as follows:

… for the prevention principle to apply, the contractor must be able to demonstrate that the employer's acts or omissions have prevented the contractor from achieving an earlier completion date and that, if that earlier completion date would not have been achieved anyway, because of concurrent delays caused by the contractor's own default, the prevention principle will not apply.

[3] Ibid.

[4] Lord Ellenborough C.J. said, "In this case, as to this proviso, it would be contrary to a universal principle of law that a party shall never take advantage of his own wrong."

Even if the buyer's acts of prevention were concurrent with the delays caused by the shipyard's own default, the prevention principle will not apply.

Concurrent delay is "a period of project overrun which is caused by two or more effective causes of delay which are of approximately equal causative potency" (Marrin, 2012).

In the case of North Midland Building Limited v. Cyden Homes Ltd. (2018), the contractor raised an interesting argument. The parties included a provision in their contract pursuant to which any delay caused by a Relevant Event (caused by the employer) which is concurrent with another delay for which the contractor is responsible shall not be taken into account.

Although the contractual provision on concurrent delay was clear, and although the shipyard partly caused the delay, it still argued that the prevention principle was a matter of legal policy which should operate to the benefit of the contractor and set aside the clause to which it had agreed in the contract.

The Court of Appeal rejected that argument because (inter alia) "the prevention principle is not an overriding rule of public or legal policy" and the contract contained a clear provision as to what happens in the event of concurrent delay (North Midland Building Ltd v Cyden Homes Ltd., 2018).

8. CONCLUSION

As stated at the beginning of this article, the shipyard would be in breach of contract if it fails to tender for delivery the vessel that complies with the shipbuilding contract within the contract time.

The consequences of such a breach may be that the shipyard would be required to pay liquidated damages to the buyer as compensation for loss caused by the late delivery. Another consequence might be the termination of the contract by the buyer and the buyer's claim for the refund of the pre-delivery instalments, together with interest thereon, and, sometimes, damages.

In order to avoid liabilities for delays in performing their shipbuilding contracts, many shipyards, as well as their suppliers, claim the application of extension of time provisions (permissible delays) in their shipbuilding contracts.

If shipyards wish to rely on extension of time clauses in their shipbuilding contracts, they should ensure that they have a very strict documentary policy in place, a system of prompt notifications to the buyer, a system of recording relevant events that are causing or may cause delays in the construction and/or delivery of the vessel, and critical path diagrams.

DATA AVAILABILITY STATEMENT

The published publication includes all graphics and data collected or developed during the study.

CONFLICT OF INTEREST

The author declared no potential conflicts of interest with respect to the research, authorship, and/or publication of this article.

ETHICS

There are no ethical issues with the publication of this manuscript.

FINANCIAL DISCLOSURE

The authors declared that this study has received no financial support.

REFERENCES

Adyard Abu Dhabi v. SDS Marine Services. (2011). EWHC 848 (Comm). https://www.bailii.org/ew/cases/EWHC/Comm/2011/848.html.

BIMCO. (n.d.). *Contracts*/NEWBUILDCON. Retrieved from https://www.bimco.org/Contracts-and-clauses.

Jerram Halkus Construction Ltd v. Fenice Investments Inc. (2011). EWHC 1935 (TCC). https://www.bailii.org/ew/cases/EWHC/TCC/2011/1935.html.

Marrin, J. (2012, December 12). Concurrent delay revisited. Paper No. 179 presented at the *Society of Construction Law*. London, UK.

Multiplex Constructions UK Ltd. v. Honeywell Control Systems Ltd. (2007). Adj. L.R. 03/06, EWHC 447 (TCC). https://www.isurv.com/directory_record/4329/no_2.

North Midland Building Ltd v Cyden Homes Ltd. (2018). EWCA Civ 1744. https://www.fenwickelliott.com/research-insight/newsletters/dispatch/archive/ .

Rede v. Farr. (1817). 6 M. & S. 121. 105 ER 1188.

Shawton Engineering v DGP International Ltd. (2005). AII ER (D) 241, CA; CILL 2306 CA. https://www.isurv.com/directory_record/4509/.

Stocznia Gdanska S. A. v. Latvian Shipping Co. and Others. (1998). House of Lords judgment. www.publications.parliament/uk.

Zhousan Jinhaiwan Shipyard Co. v Golden Exquisite and Others. (2015). Lloyd's Rep. 283. https://www.i-law.com/ilaw/doc/view.htm?id=352316.

Seatific, Vol. 3, Issue. 2, pp. 89–110, December 2023

Seatific Journal
https://seatific.yildiz.edu.tr
DOI: https://doi.org/10.14744/seatific.2023.0010

Seatific

Review Article

Smart materials finishing and insulation solutions applied to the interior design of a cruise ship cabin

Angela Denise PERI*

Department of Architecture and Design (DAD),University of Genoa, Genoa, Italy

ARTICLE INFO

Article history
Received: November 09, 2023
Revised: December 11, 2023
Accepted: December 16, 2023

Key words:
Cruise Ship Design; smart materials; thermo-acoustic insulation; humidity control, self-cleaning materials; self-healing materials; air purification systems

ABSTRACT

A cruise ship cabin can be outlined using a complex bill of materials, components and sub-assemblies properly interconnected, considering its functional nature as a whole. In this regard, modern scientific achievements have allowed the development of so-called smart materials. The research activity has started with a scoping review of the currently constituent finishing, as well as insulation materials installed on-board. The assessment of smart and high-performance solutions is aimed of optimizing thickness, weight, noise and vibrations parametres. Actual cases under analysis related to finishing materials include performance paints and inks, fabrics with antibacterial and water-repellent properties which, together with a protective action, can generate electricity if exposed to light. Some polymeric fibres can thermally modify their sensitivity to humidity and allow for better adaptability and reversible shrinkage, self-healing surfaces regenerate after the occurrence of a crack. Active safety, failure prevention, and comfort criteria on board passenger ships are the main focus of many of the technological applications under investigation. It is necessary for them to evaluate the compatibility with the marine environment, durability, and compliance with the rules.

Cite this article as: Peri AD. Smart materials finishing and insulation solutions applied to the interior design of a cruise ship cabin. Seatific 2023;3:2:89–110.

1. INTRODUCTION

The current scoping review activity, connected to the doctoral thesis currently under development, is focused on the interior design of cruise ships, which have the common denominator of implementing high-performance (Wang, Tang, 2022) and smart materials which could increase the overall comfort performance, energy optimization and compliance with safety classification rules.

The suggested taxonomy (Goldade et al., 2015) includes, without any formal disconnection, currently used and potential applicable achievements, with an integration of innovative technologies intrinsically linked to the designed and molecular-controlled substance constitution (Bengisu, Ferrara, 2018) as in the case of smart materials. The simultaneous presence is determined by the design need to integrate the new paradigm with a knowledge that has been diachronically consolidated (Peijnenburg et al., 2021). The regulatory framework currently in use in the field of design will introduce the most common insulation materials. High performance and smart materials solutions principles are described, along with a list of tests used to assess their properties and possible, future applications on board.

2. THE ROLE OF ACOUSTIC AND THERMAL INSULATION IN THE SHIPBUILDING INDUSTRY

Typical noises and vibrational stresses associated with cruise ships are generated by the rushing of water against the hull and related to the operational profile of engines, propellers,

***Corresponding author.**
*E-mail address: angela.denise.peri@edu.unige.it

machinery and air conditioning, as well as sounds generated by onboard activities. These are transferred throughout the structure and spread towards the accommodation areas. Acoustic insulation applications (Adam, 2016) have significant impact in reducing noise levels, minimizing reverberation, eliminating echoes, and improving speech clarity. A proper thermal insulation (Lakatos, 2022), on the other hand, is performed to control and maintain the design temperature within the ship's interior spaces that is, minimizing the transfer of heat between the interior and exterior environments. This would result in an overall increase of the energy efficiency by reducing the reliance on heating or cooling systems.

Thermoacoustic insulation plays a crucial role in ensuring the comfort and safety of passengers and crew on cruise ships accommodation area, especially within cabins.

These latter are regulated by the international SOLAS Convention (Safety of Life at Sea). Is has been issued by the International Maritime Organization (IMO), a specialized agency of the United Nations responsible for regulating shipping on a global scale. The first Convention was adopted in 1914 (after the Titanic disaster) and the current version entered into force in 1974. SOLAS primary goal is to establish minimum requirements for ship construction, equipment, and operation, compatible with their safety. Merchant ships, like cruise ships, are required to comply with these strict safety standards.

It is divided into fourteen chapters and rules that are comprehensively addressed to distinct aspects of safety in the specific environment of ships. Chapter II-2, titled "Construction – Fire protection, fire detection and fire extinction," specifically focuses on fire protection, detection and extinction. The products referenced in this section, including materials and components used in ship construction (bulkheads, decks, fire doors, fire-resistant closures, upholstered furniture, bed components, lining materials, and curtains) have to withstand international requirements for laboratory testing, type-approval and fire test provided by the International Code for Application of Fire Test Procedures, 2010 (2010 FTP Code).

In particular, non-combustibility tests and substance classification are performed according to IMO 2010 FTP Code Part 1, IMO-Resolution MSC.307(88). Surface flammability ones are compliant to Part 5 and fire tests on A and B divisions are achieved in conformity to Part 3. Furthermore, there are threshold values related to the transmission of noise and vibrations established by the ISO 20283-5:2016 (Measurement of vibration on ships — Part 5: Guidelines for measurement, evaluation and reporting of vibration about habitability on passenger and merchant ships).

To highlight the potential localized interventions, it is important to briefly describe the composition of a standard cabin module, which is comprised of steel ceiling and wall panels (in most cases galvanized) or aluminium alloy. The internal face of each of them is finished by applying decorative coatings. Rock wool is the traditional material used to insulate and fire-proof the external facing. Bulkheads between cabins will be comprised of two adjacent panels, with a small hollow space between them. In the same way, if a passenger cabin is adjacent to a public passageway, the tools and methods of partitioning and finishing will be similar since the corridors too are assembled with similar prefabricated panel elements.

2.1. Thermo-acoustic material selection outlines

The research activity has started with a classification of the main insulating materials applied in the shipbuilding sector, considering the constituent type of the fibres (Fig. 1).

A main difference between Natural-based and Petrolchemical materials is taken into account, each of them further divided into organic (Table 1, 2) and inorganic groups (Table 3, 4).

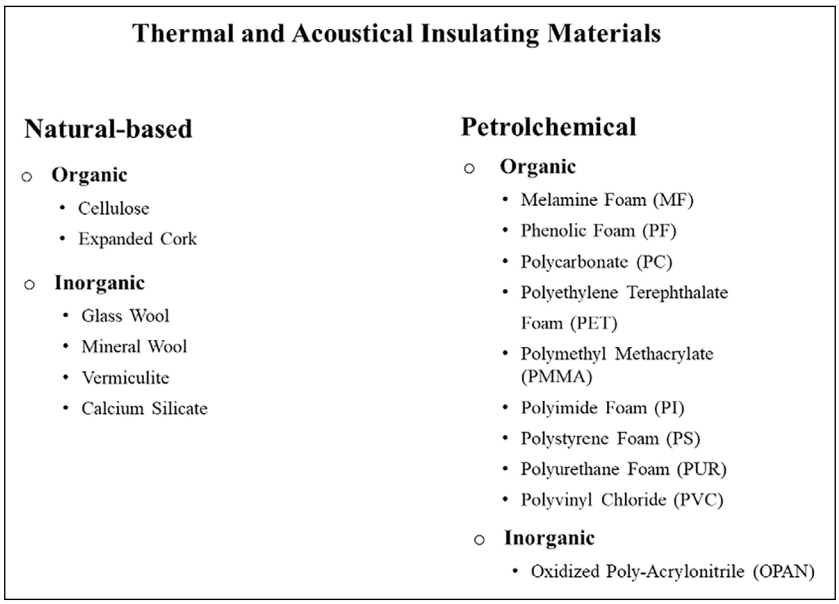

Figure 1. Thermoacoustic material classification.

Table 1. Natural-based organic materials

Type	Technical description	Density [kg/m³]	Thermal conductivity [W/m°C]	Specic heat capacity [J/kg°C]	Acoustic velocity [m/s]	Form	Application
Cellulose [1]	Cellulose-based products made primarily from post-consumer and industrial paper, with recycled newspaper being the main raw material	48–128	0.037	2000	–	Panels	Accommodation and entertainment areas
Expanded cork	Derived from the bark of cork oak trees, specifically quercus suber. It undergoes expansion through heating and pressure treatment	160–240	0.04–0.048	1900–2100	344–525	Sheets, boards	Floors solutions

[1] Referred values for CFAB™ Cellulose-based, thermo-acoustic panels

Table 2. Natural-based inorganic materials

Type	Technical description	Density [kg/m³]	Thermal conductivity [W/m°C]	Specic heat capacity [J/kg°C]	Acoustic velocity [m/s]	Form	Application
Calcium silicate [2]	Inorganic material composed of calcium, silica, and reinforcing fibres. The material is formed through a chemical reaction and heat treatment process, resulting in rigid and fire-resistant boards	280-320	0.07	1100	–	Boards	High-temperature insulation and fireproofing. Acoustic tiles and insulation in ducts a non-combustible autoclaved calcium silicate board
Glass wool	Insulating material made from fine fibres of glass. Glass wool is produced by melting glass and then spinning it into fibres	11–70 [3]	0,033–0.040 [3]	1030 [3]	180 [5]	Boards, rolls	Wall insulation and HVAC (Heating Ventilation and Air Conditioning) system
Mineral wool	Insulating material made from natural or recycled stone The stone is melted and spun into fibres	25–100 [3]	0.033–0.044 [3]	840 [4]	180 [5]	Boards, rolls	Wall insulation and HVAC system
Vermiculite	Composed of hydrated laminar magnesiun-aluminium-ironsilicate which resembles mica. It is most used in its exfoliated (expanded) form	64–160	0.058–0.070	840–1080	630–1360	Hard-core panels, boards	Thermal insulation in structural elements for large public spaces. Acoustic-fireproofing panels

[2] Referred values for Bacchi Spa™ lightweight panel; [3] Hongisto et al. (2022); [4] Rockwool ™ database; [5] Reference value for mineral wools from Isover ™ Database

Table 3. Petrochemical organic materials

Type	Technical description	Density [kg/m^3]	Thermal conductivity [W/m°C]	Specic heat capacity [J/kg°C]	Acoustic velocity [m/s]	Form	Application
Melamine Foam (MF)	Open-cell foam composed of melamine resin, a thermosetting polymer derived from melamine and formaldehyde. It is high porous	9–12	0.032–0.035	1650–1800	95.5–142	Sheets, panels	Cabin ceiling/floors and accomodation areas. HVAC insulation, noise barriers and acoustic absorbers
Phenolic Foam (PF)	Thermosetting plastic foam made from phenol formaldehyde resin. The foam structure consists of a network of cells, providing low thermal conductivity and fire-resistant properties	32–38 (closed cell 0.035)	0.02	1850–1910	334–455	Sheets, boards	Refrigeration and pipes insulation, acoustic panels
Polycarbonate (PC)	Transparent thermoplastic known for its high impact resistance, optical clarity, and UV stability It can be extruded into sheets or molded into panels with varying thicknesses and shapes	1190–1210	0.19–0.22	1150–1250	1390–1430	Sheets, panels	Windows and protective barriers, transparent partitions
Polyethylene Terephthalate Foam (PET)	Closed-cell foam made from polyethylene, a thermoplastic polymer. Lightweight, flexible, and resilient material with closed cells	75–110	0.033–0.035	1140–1260	687–821	Sheets, boards	Core material for sandwich panels, acoustic insulation walls, ceilings, and floors of cabins
Polymethyl Methacrylate (PMMA)	Transparent thermoplastic known for its optical clarity, scratch resistance, and UV stability. It is typically extruded into sheets or molded into panels	1160–1220	0.19–0.21	1400–1480	1410–1800	Sheets, panels	Windows and decorative panels, transparent partitions
Polyimide Foam (PI)	High-temperature resistant foam made from polyimide resin, which is known for its excellent thermal stability and resistance to heat, chemicals, and radiation	15–32	0.032–0.304	1390–1450	119–173	Sheets, rolls	High-temperature insulation and in electronics. Acoustic insulation in machinery spaces
Polystyrene Foam (PS)	Synthetic polymer made from monomers of the aromatic hydrocarbon styrene. Closed-cell structures provides thermal insulation and buoyancy	28–32	0.032–0.036	1200–1220	468–616	Sheets, boards	Insulation boards,walls soundproofing
Polyurethane Foam (PUR)	Foam formed by reacting polyols and isocyanatesopen-cell or closed-cell structure with varying densities	30–34	0.03–0.035	1650–1700	35.1–43.7	Spray foam, boards	Pies and plant insulation
Polyvinyl Chloride (PVC)	Thermoplastic known for its versatility and durability. PVC is produced in various forms through polymerization of vinyl chloride monomer	36–44	0.02–0.03	1120–1140	745–871	Sheets, pipes	Cable insulation Soundproofing and wall coverings

Table 4. Petrochemical inorganic materials

Type	Technical description	Density [kg/m³]	Thermal conductivity [W/m°C]	Specic heat capacity [J/kg°C]	Acoustic velocity [m/s]	Form	Application
Oxidized Poly-Acrylonitrile (OPAN) [6]	Material derived from polyacrylonitrile polymer. It undergoes preoxidation and stabilization processes to enhance its thermal stability and fire resistance	100	0.031	700–750	–	Sheets, rolls	Thermal and fire protection in machinery spaces

[6] Reference values for Zoltex Carbonized PX 35 felt

It could be possible thanks to the application of Granta EduPack Software, currently used in an interdisciplinary matter in the academic field to perform complex analysis which can synoptically consider engineering, design and sustainable development aspects. The user can perform analysis based on three stages. Level 1 database contains an introductory approach of more than 60 records or common engineering materials (metals, plastics, ceramics, glasses, composites and natural materials). A limited set of attributes is linked to records for processes that are used to shape, join or finish them.

Level 2 contains a comprehensive set of mechanical, thermal and electrical properties, as well as Eco Properties and Durability Information, for more than 100 common materials. The materials and the content of the records enable a wide range of selection studies and environmental audits of products. The process records include a simple cost model that allows cost-comparisons between alternative processes.

Belonging to this level is the Building Environment repository, which contains more than 120 materials commonly used in Architectural applications. A set of mechanical, thermal, electrical, hygro-thermal, acoustic is provided, along with durability information.

Level 3 contains a comprehensive set of the previous data, together with mechanical, optical, magnetic and environmental properties for over 4,000 engineering materials. Eco Design database also encompasses environmental properties such as whether a material is restricted, NOx and SOx values, water usage, carbon footprint, embodied energy, and end of life information.

A crossed use of the second and the third level, together with a scoping review activity of the cutting-edge solutions actually present on the market and the support of the scientific literature, helped to create the material classification.

It should be stressed that specific heat and thermal conductivity are related to an ambient temperature set at 23°C. In order to further characterise each substance, the acoustic velocity variable (m/s) has been used, as measure of the speed of longitudinal sound waves in a solid. It is calculated as follows (Equation 1):

$$v = \sqrt{\frac{E}{p}}$$ **Equation 1**. Acoustic velocity formula

where E is Young Modulus (Pa) and ρ is the material density (Kg/m³).

The speed of sound in a solid material can be used as a further indicator of its insulating properties. It depends on the density and compressibility of the matter through which it propagates. In general, in denser and more rigid materials, such as metals, the speed of sound is higher, while in less dense and more flexible ones, such as thermal insulators like wool, fiberglass and foam, the speed of sound is slower.

The parameters considered are related to the substances used and not to the finishes applied, as they could undergo variations in their weight, depending on the different thicknesses applied and their relative stratigraphy. In many

Table 5. Aerogels test methods

Testing category	Test method	Description	References
Thermal conductivity	Cryogenics test laboratory	Used to determine apparent thermal conductivity (k-value) of thermal insulation systems	Johnson et al. (2010)
Non-destructive method for mechanical properties	Diametral compression test	Application of stress load or force to the point where a material object is split in half (down the diameter of the object)	Haj-Ali et al. (2016)
Mechanical properties of silica aerogels	Micro-indentation technique	The sample material is indented using a sharp, pointed probe, with a controlled force application	Moner-Girona et al. (1999)
	Dynamic compressive test	Tests of cross-linked silica aerogel using a split Hopkinson pressure bar (SHPB) for Poisson's ratio determination	Luo et al. (2006)
Fracture toughness tests	Single-edge-notch bending (SENB)	Specimen is subjected to three-point bending loads	Ehrburger-Dolle et al. (1995)
Density measurement	Torsional oscillator measurements	Body suspended by a thread or wire which twists first in one direction and then in the reverse direction, in the horizontal plane	Crowell et al. (1990)
Hydrophobicity and Hydrophilicity	Contact Angle Measurement	Determine the contact angle of water on the aerogel surface to assess its hydrophobic or hydrophilic properties.	Ślosarczyk (2021)
Aging and Stability Tests	Long-Term Stability	Subject the aerogel to aging tests to simulate real-world conditions and evaluate its stability over time.	Perego (2008)
Environmental Resistance	Optical absorption - UV–Vis tests	Proton irradiation tests Test the aerogel's resistance to ultraviolet (UV) radiation	Wu et al. (2020)

solutions on the market these materials often constitute the core of sandwich and honeycomb compounds to combine the aforementioned properties with structural capacity.

3. SMART AND HIGH-PERFORMANCE MATERIALS FOR ADVANCED INSULATION AND FINISHING SOLUTIONS

They are related but distinct concepts in the field of materials science (Ritter, 2006). Smart materials (SM) are known for their adaptability and responsiveness to external stimuli, allowing them to change their properties or behaviour based on variable conditions, examples of which include Shape Memory Alloys and Self-Healing Polymers. On the other hand, high-performance materials (HPM) stand out in terms of their intrinsic properties, such as strength, durability, or conductivity, and are chosen for applications where outstanding, specified characteristics are crucial. While these categories are different in functionality, it's possible for some materials to belong to both if they combine high-performance attributes with adaptive capabilities (Addington, Schodek, 2005).

3.1. Aerogels (HPM)

Aerogels are highly porous, ultra-lightweight substances with very low thermal conductivity (0.017 W/m°C) (Aegerter et al., 2011), primarily composed of air. They are manufactured through a supercritical drying process that removes the liquid content of a gel. Various materials have been implemented, with silica being the most commonly used (Pierre, Anderson, 2011). Historically, aerogels production has been relatively costly, constraining its usage to advanced aerospace operations (Jin et al., 2023). However, as manufacturing expenses decline, they are finding their way into a wider array of applications, including their incorporation into composite materials such as laminated glazing for thermal insulation or integration into blankets for heat protection and acoustic absorption.

The following table show the test methods aimed at characterizing aerogels main properties (Table 5).

In cruise ship design, suitable features and applications can include:

- Internal cabin insulation: it can be used aerogels low thermal conductivity helps maintain comfortable inside temperatures, reducing the reliance on heating and cooling systems. This can lead to energy savings and lower operational costs;
- Energy-Efficient Windows: aerogels can be integrated into windows frames to enhance their thermal insulation properties. This helps reduce heat gain during sunny days and heat loss during cold weather, contributing to energy savings in the ship's overall HVAC system;
- Soundproofing: in addition to thermal insulation, aerogels can provide soundproofing benefits. Installing aerogel-based insulation in cabin walls and ceilings can help minimize noise transfer between cabins and common areas;

Table 6. Vacuum Insulation Panels (VIPs) test methods

Testing category	Test method	Description	References
Standard specification for Vacuum Insulation Panels	ASTM C1484-10(2018)	Specification covers the general requirements for vacuum insulation panels	Nikafkar and Berardi (2020)
Thermal testing	DIN EN 12667:2001	Determination of thermal resistance	Davraz and Bayrakçı (2013)
Fire test method	ISO 834-11:2014	One side of the specimen is exposed to the furnace and measured according to its appearance and ignition	Y. U. Kim et al. (2021)
Insulation performance test	ASTM C 1363	Temperatures of the constant temperature chamber and the low are measured	
Airtightness test	ASTM E 783	Pressure of the test specimen is increased in steps and the airtightness is measured until the flow rate becomes stable	
Aging and Durability Testing	International Energy Agency (IEA) - Annex 39	Thermal cycling and humidity exposure to assess their durability over time	J. Kim et al. (2017)
	Cold Climate Housing Research Center, Mobile Test Lab (CHRC's MTL)	Used to evaluate different wall configurations for durability under high interior moisture loads.	Garber-Slaght and Craven (2012)

- Fire Safety: aerogels are non-combustible materials, which is crucial for safety in cruise ship design;
- Space Constraints: the thin profile is helpful in cruise ship design, where space is often limited. It allows for effective insulation without compromising cabin space or vessel design.

3.2. Vacuum Insulation Panels (VIPs) – (HPM)

VIPs consist of a core material (typically a rigid, porous material like fiberglass or silica aerogel), enclosed in a vacuum-sealed panel, which minimizes heat transfer by eliminating air molecules. They provide high insulation efficiency in a thin profile, making them suitable for space-constrained applications (Baetens, 2010). Here's how VIPs work and why they can be effective also in the maritime field:

- Vacuum Core: core material is placed in a vacuum or near-vacuum environment, which reduces the conduction and convection of heat;
- Airtight Encapsulation: core material is sealed within a gas-tight envelope made of high-quality barrier materials, often metallic or laminated films. This envelope prevents air from entering and disrupting the vacuum, ensuring long-term insulation performance;
- Longevity: if properly maintained and protected from physical damage or perforations, VIPs can maintain their insulation properties for an extended period, making them a durable and cost-effective insulation solution over the long term.

The following table show the test methods aimed at characterizing VIPs main properties (Table 6).

3.3. Phase Change Materials (PCMs) - (SM)

This category includes all smart materials capable of undergoing reversible changes in response to external stimuli, in particular they exhibit phase changes dependent on temperature (Delgado et al., 2018). In the construction and architecture sectors, the term "PCM" has gained relevance concerning materials and products utilized for temperature regulation purposes. PCMs store and release heat energy during phase transitions, such as from solid to liquid or vice versa. They can absorb excess heat during the day and release it at night, helping to maintain a stable indoor temperature. PCMs can be embedded in insulation materials or used as standalone panels.

The following table show the test methods aimed at characterizing PCMs main properties (Table 7).

Potential applications aboard cruise ships may include:

- Temperature Control: PCMs are effective at stabilizing indoor temperatures by absorbing and releasing heat during phase transitions. In cruise ship cabins, PCMs can absorb excess heat during the day when the sun is intense and release it at night when temperatures drop, ensuring a consistent and comfortable environment for passengers;
- Space Efficiency: they are typically applied as thin layers within walls or ceilings, making them ideal for cruise ship cabins with limited space. Their slim profile allows for efficient insulation without sacrificing valuable cabin space;
- Condensation Prevention: PCMs can help prevent condensation on cabin surfaces, which is essential for maintaining a healthy and comfortable indoor environment. Condensation can lead to moisture-related issues like mold growth and corrosion;
- Retrofitting Capabilities: in some cases, existing cruise ships may undergo renovations or upgrades to improve energy efficiency and passenger comfort. PCMs can be integrated into cabin insulation during retrofitting projects to enhance insulation properties;
- Emergency Energy Backup: in the event of a power outage or HVAC system failure, PCMs can temporarily maintain indoor temperatures, ensuring passenger safety and comfort until normal operations are restored.

Table 7. Phase Change Materials (PCMs) test methods

Testing category	Test method	Description	References
Latent Heat of Fusion	Calorimetry	Measure the heat absorbed or released during the phase transition	Kotzé et al. (2014)
Thermal Cycling Stability	Repeated Heating and Cooling Cycles	Assess the stability of the material over multiple cycles, checking for performance degradation	Putra et al. (2019)
Thermal Conductivity	Standardized Methods	Measure the material's ability to conduct heat during solid and liquid phases	C. Xu et al. (2022)
Encapsulation Efficiency	Encapsulation Assessment	Evaluate the efficiency of the encapsulation process, ensuring containment and leak prevention	Y. Huang et al. (2023)
Durability and Long-Term Performance	Extended Testing Periods	Conduct long-term tests to assess durability and performance over extended periods	Egea et al. (2022)
Material Compatibility	Compatibility Tests with Other Materials	Investigate how well the PCM interacts with materials commonly used in specific applications	Ostrý et al. (2019)
Environmental Impact	Environmental Assessment	Evaluate the environmental impact, considering factors like recyclability and potential hazards	Di Bari et al. (2020)

3.4. Shape Memory Materials (SMMs) – (SM)

These materials have the remarkable ability to "remember" a specific shape and return to it when exposed to a certain stimulus, typically heat (Sun et al., 2012) (Vili, 2007). Shape-memory alloys (SMA's) exhibit two distinct crystal structures linked to a phase transformation between a low-temperature, martensitic phase and a high-temperature, austenitic phase. In the first configuration, the metal can easily be deformed into any shape; when the alloy is heated the memory metal is able to recall the shape it had before the deformation. This property enables the creation of dynamic, shape-changing structures and components like self-opening/closing windows and furniture mechanisms that can change their shape or configuration based on temperature changes (Jani et al, 2014).

Stimulus-responsive configurations refer to the ways in which shape memory materials (SMMs) can be triggered or activated to exhibit their shape-changing properties. Different types of shape memory materials respond to various stimuli, allowing for a range of applications in diverse fields. Here are some common stimulus-responsive configurations:

- Thermal Activation: the most common stimulus for shape memory materials is temperature change. For shape memory alloys (SMAs), heating above a certain transition temperature (often called the austenitic finish temperature) causes a reversible phase transformation, allowing the material to recover its original shape;
- Light Activation: some shape memory materials, particularly polymers, can be activated by exposure to light. Photothermal heating induces the required temperature change for triggering the shape memory effect. This feature is often exploited in biomedical applications where light can be precisely controlled;
- Electrical Activation: Applying an electric current to shape memory alloys can generate Joule heating, causing the material to undergo the phase transformation and recover its original shape. This electrical activation is useful in micro actuators and other electronic applications;
- Magnetic Activation: certain shape memory alloys, such as nickel-titanium, are responsive to magnetic fields. This latter induces mechanical deformation, making it possible to control the shape memory effect remotely;
- Chemical Activation: reversible chemical reaction, leading to a change in the polymer's structure and, consequently, in its shape;
- pH Activation: they can to respond to changes in pH. The pH-induced changes can alter the polymer's structure, leading to a reversible shape change;
- Moisture Activation: particularly in hydrogels They can react to changes in moisture levels. Absorption or loss of water can induce a change in the material's conformation and trigger the shape memory effect;
- Mechanical Activation: in some cases, shape memory materials can be activated by applying mechanical stress. This might involve stretching, compression, or other mechanical deformation to initiate the shape memory response;
- Dual/Multi-Stimulus Activation: some advanced configurations involve materials that respond to multiple stimuli simultaneously or sequentially.

The following tables show the test methods aimed at characterizing SMM main properties (Table 8, 9).

Between the possible application we can list the following cases:

- Adaptive Insulation: since SMM can change shape or thickness in response to temperature fluctuations, during colder periods they can expand to provide additional insulation and during summer, they could contract to allow better ventilation. This adaptability can

Table 8. Shape memory polymers (SMPs) test methods

Testing category	Testing method	Description	References
Shape Memory Effect (SME)	Shape Fixity and Recovery Test	Subject the material to a deformation at a certain temperature, then allow it to recover its original shape upon heating	Tcharkhtchi et al. (2014) Zhou and Huang (2015) Abdullah et al. (2012)
	Programming and Recovery Cycles	Assess the material's ability to go through multiple shape memory cycles without significant degradation	Li & Wang, (2016) Zhao et al. (2015) Lendlein (2010)
Thermal Characterization	Differential Scanning Calorimetry (DSC)	Measure the heat flow associated with the phase transitions in the SMP, such as the glass transition and melting temperatures	Martins (2019) McKinley (2004) Staszczak et al. (2022)
Mechanical Testing	Tensile Testing	Assess the tensile properties of SMPs, such as modulus, strength, and elongation, both below and above their transition temperatures	Fisher et al. (2020) Kim et al. (2021) Ohki et al. (2004) Tobushi et al. (2015
	Compression Testing	Investigate SMP response to compressive forces and shape recovery	
Thermo-Mechanical Analysis (TMA)	Coefficient of Thermal Expansion (CTE)	Evaluate dimensional changes in response to temperature variations	Fulcher et al. (2010) Ibarra et al. (2022)
Rheological Testing	Shear Testing	Study flow and deformation behavior under shear stress	Mohamed et al. (2022)
Dynamic Mechanical Analysis (DMA)	Frequency Sweep	Measure viscoelastic properties under dynamic loading conditions	Azra et al. (2013) Wang et al. (2023)
Chemical Resistance Testing	Exposure Tests	Expose SMP to different chemical environments for stability assessment	Jacobson and Iroh (2021) B. Wang et al. (2023)
Microscopic Analysis	Scanning Electron Microscopy (SEM)	Examine microstructure effects of deformation and recovery	Gall et al. (2002) Goda et al. (2020)
Electrical and Thermal Conductivity Testing	Electrical Resistance Measurement Thermal Conductivity Testing	Assess electrical conductivity in deformed and recovered states Evaluate thermal conductivity and heat transfer characteristics	X. Huang et al. (2021) Rybak et al. (2021) Pradhan et al. (2022)

help maintain optimal cabin temperatures without relying entirely on HVAC systems;

- Sealing and gasketing: SMMs can be employed in sealing and gasketing applications to ensure airtight seals around doors, windows, and other openings. They can change their shape or compress when necessary to maintain a tight seal, preventing drafts and heat loss.

It is important to note that SMMs are not commonly used for large-scale applications like cruise ship design at present. While they offer peculiar advantages, their adoption has to be assessed by factors such as cost, complexity, and the need for reliable control mechanisms.

3.5. Thermochromic materials (TMs)–(SM)

Thermochromic materials can be integrated into cruise ship cabin design to enhance insulation and improve the overall passenger experience (Boscolo et al., 2007). They change colour or optical properties in response to temperature variations, which can be used to create adaptive insulation systems and achieve energy efficiency in cruise ship cabins:

- Smart Window Systems: thermochromic coatings or films can be applied to cabin windows to control solar heat gain and glare. When exposed to sunlight or high temperatures, these materials darken, reducing the amount of heat and light entering the cabin. In cooler conditions or at night, they become transparent, allowing natural light to enter and potentially aiding in passive solar heating.

- Temperature-Responsive Surfaces: they can be used on cabin walls, ceilings, or other surfaces to visually indicate temperature changes. When the temperature inside the cabin rises or falls, these surfaces change colour or appearance, providing passengers with a visual cue about the thermal conditions. This can help passengers make informed decisions about adjusting the cabin temperature and HVAC settings.

- Customized Cabin Experience: cruise ship cabins often host passengers with varying preferences for temperature and lighting. Thermochromic materials can be incorporated into cabin controls, allowing passengers to adjust the cabin environment to their liking. For example, passengers can control the tint level on windows or the colour of cabin surfaces.

The test methods aimed at characterizing TH main properties are included in the following section table, since both smart materials acts in a similar way (Table 10).

Table 9. Shape memory alloys (SMAs) test methods

Testing category	Testing method	Description	References
Shape Memory Effect (SME)	One-way Shape Memory Effect	Deform material at a certain temperature and observe recovery	Naresh et al. (2016) Lexcellent et al. (2000) Meddour and Brek (2018) Gan et al. (2012)
	Two-way Shape Memory Effect	Assess ability to recover different shapes upon cooling and heating	
Thermal Characterization	Martensitic Transformation Temperature (Ms)	Determine critical temperatures using DSC or Differential Thermal Analysis	Hartl and Lagoudas (2008) Baradari et al. (2021)
	Austenitic Finish Temperature (Af)	Measure temperature associated with complete phase transformation	
Heat Treatment Analysis	Differential Scanning Calorimetry (DSC)	Study phase transformations and thermal behavior during heat treatment	Liu and Huang (2006)
	Metallography after Heat Treatment	Examine changes in microstructure due to heat treatment processes	Kožuh et al. (2018)
Mechanical Testing	Tensile Testing	Measure strength, yield strength, elongation, and modulus of elasticity	Lavernhe-Taillard et al. (2009)
	Compression Testing	Evaluate compressive strength and deformation behavior	Hashemi et al. (2023)
	Hardness Testing	Assess material hardness using Brinell, Vickers, or Rockwell tests	Arciniegas et al. (2008)
	Impact Testing	Evaluate toughness and resistance to impact loading	Sofocleous et al. (2013)
Chemical Composition Analysis	X-ray Fluorescence (XRF)	Determine elemental composition of the alloy	Alım et al. (2018)
	Atomic Emission Spectroscopy (ICP-AES)	Analyze element composition, especially traces	G. Fisher (2003) Fink et al. (2023)
Non-Destructive Testing (NDT)	Ultrasonic Testing (UT)	Detect internal defects or flaws in the alloy	Lee et al. (2023) Meir et al. (2011)
	Radiographic Testing (RT)	Use X-rays or gamma rays to inspect the internal structure	
	Eddy Current Testing	Detect surface and near-surface flaws in conductive materials	Testing high performance small diameter Nitinol wire - the largest portal of nondestructive testing (NDT). https://www.ndt.net/search/docs.php3?id=22368
Corrosion Testing	Salt Spray Test	Evaluate corrosion resistance in a saline environment	Charfi et al. (2009) Sampath et al. (2023) Rondelli (1996) Soltan et al. (2023)
	Electrochemical Corrosion Testing	Measure corrosion rate under controlled electrochemical conditions	
Fatigue Testing	Rotating Beam Fatigue Test or Axial Fatigue Test	Assess fatigue strength and behaviour under cyclic loading	Dornelas et al. (2021) Kang and Song (2015)

Table 10. Thermochromic (TMs) and electrochromic (ECMs) materials test methods

Testing category	Testing method	Description	References
Optical Properties	Transmittance Spectroscopy	Measure transparency in visible and near-infrared regions	Rai et al. (2020) Jelle and Hägen (1993)
	Coloration Efficiency	Quantify color change per unit of applied charge	Fabretto et al. (2007)
Electrochemical Properties	Cyclic Voltammetry (CV)	Examine redox behavior through potential sweeps	Elgrishi et al. (2017)
	Chronoamperometry	Study electrochemical response over time	K. Zhou (2020)
	Impedance Spectroscopy	Analyze electrical impedance as a function of frequency	Pehlivan et al. (2021)
Mechanical Properties	Durability Testing	Evaluate stability under repeated cycling	Tracy et al. (1999)
	Adhesion Strength	Assess adhesion between electrochromic layer and substrate	Ko et al. (2022)
Environmental Stability	Chemical Resistance	Test resistance to moisture, chemicals, temperature	Fan et al. (2020) Jensen et al. (2013) Borui et al. (2022)
	Long-Term Stability	Assess performance over an extended period	Ye et al. (2018) Chang et al. (2018) (TM) Y. Liu et al. (2023) (TM)
	Colour retention test	Examines how well the material retains its original color after multiple thermal cycles	Wałęsa-Chorab and Skene (2020)
Color transition temperature (TM)	Differential Scanning Calorimetry (DSC)	Measure the heat flow associated with the material's phase transitions, providing information on the color transition temperature	Fu and Hu (2017) Strbac (2022) (TM) Viková and Vik (2023)
Thermal Conductivity (TM)	Thermal Conductivity Measurements	Evaluate the material's ability to conduct heat, which can impact its response time to temperature changes	Ning et al. (2023)
Morphological Changes (TM)	Scanning Electron Microscopy (SEM)	Examine the material's surface morphology to understand any structural changes induced by temperature variations	Jia et al. (2021)
Electrochromic Device	Switching Speed	Measure transition time between colored and bleached states	Bessinger et al. (2021) Xu et al. (2016)
Performance	Cycling Stability	Evaluate performance over numerous coloration/bleaching cycles	Padilla et al. (2023) Fiksman (1997) (TM) Wu et al. (2023)
	Response to external stimuli	Assess material's response to factors like light intensity or temperature changes	R. Li et al. (2021) Hassab et al. (2018)
Energy Efficiency	Energy consumption	Evaluate energy efficiency during coloration and bleaching	Park et al. (2021)

3.6. Electrochromic materials (ECMs) – (SM)

Electrochromic materials change their optical properties in response to an applied electrical voltage quicker than the previous class. To manage solar heat gain and reduce heating or cooling, windows can be controlled by controlling their transparency or reflectivity (Somani, Radhakrishnan, 2003). However, they can contribute to energy efficiency and passenger comfort in cruise ship cabins through the control of natural light and glare (Granqvist et al., 2018). Here's how electrochromic materials can be applied in cruise ship design:

- Smart Windows: cruise ship cabins can incorporate electrochromic windows to control the amount of incoming natural light and reduce glare. They provide passengers with control over their cabin's lighting conditions, allowing them to adjust the opacity of the windows to control visibility from outside the cabin, thus enhancing privacy.
- Energy Efficiency: while not a direct insulation material, electrochromic windows can contribute to energy efficiency by reducing the need for artificial lighting and shading in cabins. By optimizing natural light levels, cruise ships can lower their energy consumption for lighting and cooling, resulting in cost savings and reduced environmental impact.

The following tables show the test methods aimed at characterizing TM and EM main properties (Table 10).

3.8. Dynamic insulation systems

They can be designed to mitigate the effects of vibrations and motions experienced by passengers in their cabins. These systems use sensors, actuators, and control algorithms to counteract ship motions caused by waves, engine vibrations, and other factors, thereby enhancing passenger comfort (Fawaier, Bokor, 2022). Here's how active vibration control works in cruise ship cabins:

- Sensors: vibration sensors are strategically placed in the cabin to detect any vibrations and motions. These sensors continuously monitor the cabin's movement in multiple axes, capturing data about the ship's vibrations and oscillations;
- Control Algorithms: advanced control algorithms process the sensor data in real-time. They calculate the optimal corrective actions needed to counteract the vibrations and motions and maintain a stable and comfortable environment inside the cabin;
- Actuators: devices able to generate forces to counteract the detected vibrations and motions. They are typically located beneath the cabin's floor or within the cabin's structure. These actuators can include hydraulic pistons, electromechanical devices, or other mechanisms capable of applying forces in various directions;
- Feedback Control: it uses feedback from the sensors to adjust the actuators' output. By applying forces in the opposite direction to the detected vibrations and motions, the system effectively cancels out or dampens the cabin's motions;
- Adaptive Control: some advanced systems use adaptive control techniques that continuously adapt to changing ship conditions and passenger preferences. They can optimize their performance based on real-time data and adjust to different sea conditions, cruise speeds, and passenger activities;
- User Interface: passengers may have control over the system through a user-friendly interface in the cabin. They can adjust the level of vibration control or turn it off if they prefer a more natural experience.

Potential benefits of applicating active vibration control in cruise ship cabins can include:

- Improved Comfort: Guests experience less discomfort and motion sickness, especially during rough sea conditions or when the ship is manoeuvring.
- Safety and Structural Benefits: These systems can also help protect the structural integrity of the ship by reducing the wear and tear caused by vibrations over time.

4. SMART MATERIALS FINISHING SOLUTIONS TO REDUCE HUMIDITY IN WET UNITS OF A CRUISE SHIP CABIN

Reducing humidity in these area is crucial to guarantee passenger comfort and preventing issues like mold growth and moisture damage. Several smart materials and technologies can be employed to achieve this target:

- Hygroscopic Coatings: they are designed to absorb moisture from the air. Applying these coatings to cabin surfaces, such as walls and ceilings, can help reduce humidity levels. These coatings could be designed to release the absorbed moisture back into the air when conditions are drier (Hickey et al., 1990);
- Moisture-Absorbing Fabrics: textiles treated with moisture-absorbing compounds can help absorb excess humidity from the air. These fabrics could be used for shower curtains, towels, and other cabin textiles (Wang, 2017);
- Membrane Dehumidification: these systems use selectively permeable membranes to allow moisture vapor to pass through while preventing liquid water from entering (Zhao, 2015);
- Control Systems: a centralized control system that monitors cabin humidity levels and coordinates the operation of various humidity-reducing technologies can ensure efficient and effective humidity management;
- Data Analysis and Feedback: collecting and analysing data on cabin humidity cevels and the performance of humidity-reducing technologies can provide valuable insights for continuous improvement and adjustment.

4.1. Self-cleaning surfaces

Often referred to as "hydrophobic" surfaces, are designed to repel dirt, water, and other contaminants, making them resistant to staining and facilitating easier cleaning. These can be achieved through the use of various technologies and materials (Liu, Jiang, 2012) like:

- Hydrophobic Coatings: designed to repel water, preventing water droplets from adhering to the surface. This not only prevents water spots but also helps to carry away dirt and contaminants as water rolls off (Schmidt et al., 1994);
- Photocatalytic Coatings Surfaces: when exposed to light, they can break down organic compounds and pollutants on the surface. This process helps to keep the surface clean by decomposing dirt and organic matter (Yoshida et al., 2016). Furter characterization will be provide in the next paragraph, with a specific focus on their application in HVAC components;
- Superhydrophobic Coatings: they go beyond hydrophobic coatings by creating a surface with extreme water-repellent properties. These coatings can cause water droplets to form near-perfect spheres and easily roll off the surface, taking dirt and contaminants with them (Wang et al., 2020);
- Self-Cleaning Glass: it is coated with a photocatalytic and hydrophobic layer that breaks down organic matter and allows rainwater to wash away dirt and debris (Chabas et al., 2008);
- Electrodynamic Surface Cleaning: some surfaces can be designed to generate an electrostatic charge that repels dust and particles, helping to keep the surface cleaner over time (Deputatova et al., 2018);
- Anti-Static Coatings: they can help preventing the arise of static charges able to attract dust and dirt, keeping the surface cleaner for longer (Al-Dahoudi et al., 2001).
- Oleophobic Coatings: Oleophobic coatings repel oils and grease, making them particularly effective for surfaces that come into contact with oily substances (Cao, Gao, 2010).

Applications of Self-Cleaning Surfaces in Interior Design can include:

- Wet unit surfaces: self-cleaning surfaces in bathrooms can prevent soap scum, mineral deposits, and water spots on fixtures and tiles;
- Windows and Glass: self-cleaning glass can help maintain clear visibility by repelling water and dirt, reducing the need for frequent cleaning;
- Furniture and Upholstery: self-cleaning upholstery can resist spills and stains, making furniture more durable and easy to maintain.

5. SMART MATERIALS FOR CABIN AIR IMPROVEMENT

Smart materials can play a significant role in improving room air quality by actively monitoring and addressing pollutants, allergens, and other contaminants (Grinshpun et al, 2006). Here are some types of smart materials, strictly related to the previous ones, that can be used for cabin air improvement:

- Photocatalytic coating in HVAC system: a photocatalyst, usually Titanium Dioxide, is applied as a thin coating on a surface within the air purification system, which is often part of a filter or a material that can be exposed to UV light. UV-C LEDs lamps emit ultraviolet light with a wavelength in the range of 254 to 365 nanometres, coinciding with the peak UV absorption of virus RNA (Nunayon et al., 2019). When this latter interacts with the photocatalyst, it triggers a photocatalytic reaction, generating highly reactive oxygen radicals, which break down and oxidize a wide range of indoor air pollutants, including volatile organic compounds (VOCs), bacteria, viruses, and odorous compounds (Zaleska et al., 2010);
- Air-Purifying Paints: these paints contain photocatalytic materials that react as described in the previous topic. Among paints currently available on the market them we can find also Activated Carbon Paints, which can adsorb and trap volatile organic compounds (VOCs) and odours from the air and Mineral-Based paints, which incorporate natural minerals like zeolites, which can neutralize certain pollutants, including ammonia and formaldehyde;
- Active Ventilation Systems: smart materials can be integrated into ventilation systems to actively filter and purify incoming air, removing contaminants before they enter the room.
- Intelligent Air Quality Sensors: smart sensors that detect pollutants, allergens, and other air quality parameters can trigger ventilation or purification systems for real-time air improvement.

6. SELF-HEALING FINISHING SOLUTIONS

Self-healing materials (SHM) can repair damage automatically without external intervention, potentially reducing the need for maintenance (Blaiszik et al., 2010).

They could be used in interior spaces to maintain aesthetics. For example, in cabins or public areas, self-healing coatings on furniture or wall surfaces could help minimize visible damage (White et al., 2001). Here are some examples of self-healing insulation materials and their characteristics:

- Microcapsule-based systems: they contain tiny capsules filled with a healing agent or polymer. When the insulation material is damaged, such as by a crack or hole, the capsules break, releasing the healing agent, which then fills the gap and solidifies, restoring the insulation's integrity;
- Shape Memory Polymers: as seen in the dedicated paragraph, they are materials that can "remember" their original shape and return to it when triggered by a specific stimulus, such as heat;
- Self-Healing Gels: they can autonomously repair themselves when damaged. These gels typically consist of a polymer matrix and a healing agent. When the material is damaged, the healing agent is released and reacts with the polymer to fill the damaged area and restore original properties (Zhao et al., 2014);
- Chemically Responsive Materials: certain materials are designed to be chemically responsive to environmental factors. For instance, they can sense changes in pH,

Table 11. Self-healing materials (SHMs) test methods

Testing category	Test method	Description	References
Microcapsule Healing Test	Microcapsule Preparation	Embedding of microcapsules containing healing agents within the material Evaluated parametres are: size, distribution, and content	J. Lee et al. (2021) White et al. (n.d.) B. Liu et al. (2023) Pan et al. (2022) Bekas et al. (2016) Ma et al. (2023)
	Damage Introduction	Damage is induced, and the release of the healing agent is monitored Techniques like indentation or scratching can be employed	
	Healing Assessment	Recovery of mechanical, thermal, or chemical properties is assessed using techniques such as tensile testing, thermal analysis, or spectroscopy	
Vascular Healing Test	Vascular Network Design	Design and fabrication of vascular networks within the material, ensuring proper distribution and connectivity	Selvarajoo et al. (2020) Shields et al. (2021) Hamilton et al. (2011) M. W. Lee et al. (2018)
	Damage and Healing	Controlled damage is introduced, and the response of the vascular system, including the release and distribution of healing agents, is observed	
	Characterization	Techniques like microscopy, imaging, or chemical analysis are used to characterize the healing process and the effectiveness of the vascular system	
Autonomous Healing Test	Inherent Healing Mechanisms	Identification and understanding of the inherent mechanisms responsible for autonomous healing	Arroyave et al. (2023) Mao et al. (2020) Gojević et al. (2023) Rahman et al. (2012)
	Damage Scenarios	Testing the material under various damage scenarios to observe how it autonomously repairs without external triggers	
	Performance Metrics	Quantifying the recovery in terms of mechanical, thermal, or other relevant properties without external intervention	
Durability	Ageing Tests	Evaluate the long-term stability and performance of the self-healing insulation material under various environmental conditions	Mirzamojeni et al. (2023) Haimei et al. (2023) Zhang et al. (2022)
Failure	Failure Analysis	failure analysis to understand the limitations and potential failure modes of the self-healing material	Mphahlele et al. (2017)

moisture, or temperature and initiate self-healing processes accordingly, often through chemical reactions that bond or seal damaged areas;

- Nanotechnology-Enhanced Materials: they are self-healing materials with nanoscale components. For instance, nano capsules filled with healing agents can be dispersed throughout the material to facilitate autonomous repairs (Amendola, Meneghetti, 2009);
- Carbon Nanotube Networks: they can be used to reinforce materials and provide self-healing capabilities (Joo et al., 2018). When damage occurs, the carbon nanotube network can redistribute stress and prevent further degradation;
- Microfluidic Systems: materials with embedded microfluidic channels can transport healing agents to damaged areas through a network of channels, facilitating autonomous repair (DeMello, 2016).
- Electrochemical Materials: they rely upon an electrochemical process to repair damage by redistributing ions and rebuilding material structures.

The following tables show the test method aimed at characterizing SHM main properties (Table 11).

7. CONCLUSION

In the cruise ship design field there are many constraints that limit the choice of materials and the application of cutting-edge technologies. However, through an analysis of the current state of thermo-acoustic insulation, to the optical and mechanical performance of surfaces, linked to sanitation and wear activities, it is possible to consider the introduction of adaptive solutions which can intrinsically react to external stimuli. The analysis of smart materials has highlighted how they can contribute to increasing safety and comfort on board, even if there could be problems related to the scalability of the solutions and the economic and their practical application feasibility. The taxonomy of smart materials and solutions presents, in a brainstorm-like attempt, a wide range of possible implications which, permeating from and into other areas of scientific research, could provide practical application in the more or less distant future.

DATA AVAILABILITY STATEMENT

The published publication includes all graphics and data collected or developed during the study.

CONFLICT OF INTEREST

The author declared no potential conflicts of interest with respect to the research, authorship, and/or publication of this article.

ETHICS

There are no ethical issues with the publication of this manuscript.

FINANCIAL DISCLOSURE

The authors declared that this study has received no financial support.

REFERENCES

Abdullah, S. C., Jumahat, A., Abdullah, N. R., & Frormann, L. (2012). Determination of shape fixity and shape recovery rate of carbon nanotube-filled shape memory polymer nanocomposites. *Procedia Engineering*, *41*, 1641–1646. [CrossRef]

Adams, T. (2016). *Sound materials: A Compendium of Sound Absorbing Materials for Architecture and Design*. Frame Publishers.

Addington, M., & Schodek, D. (2012). *Smart materials and technologies in architecture*. Routledge. [CrossRef]

Aegerter, M. A., Leventis, N., & Koebel, M. M. (2011). *Aerogels Handbook*. Springer Science & Business Media. [CrossRef]

Al-Dahoudi, N., Bisht, H., Göbbert, C., Krajewski, T., & Aegerter, M. A. (2001). Transparent conducting, anti-static and anti-static–anti-glare coatings on plastic substrates. *Thin Solid Films*, *392*, 299–304. [CrossRef]

Alım, B., Han, I., & Demir, L. (2018). Alloying effect on K shell X-ray fluorescence cross-sections and yields in Ti-Ni based shape memory alloys. *Journal of Radiation Research and Applied Sciences, 11*, 150–156. [CrossRef]

Amendola, V., & Meneghetti, M. (2009). Self-healing at the nanoscale. *Nanoscale, 1*, 74. [CrossRef]

Arciniegas, M. P., Casals, J., Manero, J. M., Peña, J., & Gil, F. (2008). Study of hardness and wear behaviour of NiTi shape memory alloys. *Journal of Alloys and Compounds, 460*, 213–219. [CrossRef]

Arroyave, S., Asensio, E., Perilla, J. E., Narváez-Rincón, P. C., Cadavid, A., & Guerrero, A. (2023). Evaluation and characterization of autonomous self-healing cementitious materials with low carbon footprint using hybrid organic/inorganic microcapsules. *Materials Today: Proceedings*. [CrossRef]

Azra, C., Plummer, C. J. G., & Månson, J. E. (2013). Dynamic mechanical analysis for rapid assessment of the time-dependent recovery behavior of shape memory polymers. *Smart Materials and Structures, 22*, 075037. [CrossRef]

Bætens, R., Jelle, B. P., Thue, J. V., Tenpierik, M., Grynning, S., Uvsløkk, S., & Gustavsen, A. (2010). Vacuum insulation panels for building applications: A review and beyond. *Energy and Buildings, 42*, 147–172. [CrossRef]

Baradari, S., Resnina, N., Belyaev, S., & Nili-Ahmadabadi, M. (2021). Martensitic phase transformation and shape memory properties of the as-cast NiCuTiHf and NiCuTiHfZr alloys. *Journal of Alloys and Compounds, 888*, 161534. [CrossRef]

Barati, M., Kadkhodaei, M., & Chirani, S. A. (2018). Investigation on pseudoelastic training method and the generated two-way shape memory effect in NiTi shape memory alloy. *Modares Mechanical Engineering, 18*, 86–94.

Behl, M., & Lendlein, A. (2007). Shape-memory polymers. *Materials Today, 10*, 20–28. [CrossRef]

Bekas, D., Tsirka, K., Baltzis, D., & Paipetis, A.S. (2016). Self-healing materials: A review of advances in materials, evaluation, characterization and monitoring techniques. *Composites Part B: Engineering, 87*, 92–119. [CrossRef]

Bell, V. B., & Rand, P. (2006). *Materials for architectural design*. Laurence King Pub.

Bengisu, M., & Ferrara, M. (2018). *Materials that Move: Smart Materials, Intelligent Design*. Springer. [CrossRef]

Bessinger, D., Muggli, K., Beetz, M., Auras, F., & Bein, T. (2021). Fast-Switching VIS–IR Electrochromic covalent organic frameworks. *Journal of the American Chemical Society, 143*, 7351–7357. [CrossRef]

Blaiszik, B. J., Kramer, S., Olugebefola, S. C., Moore, J. S., Sottos, N. R., White, S. R. (2010). Self-Healing Polymers and Composites. *Annual Review of Materials Research, 40*, 179–211. [CrossRef]

Bode, S., Enke, M., Hernández, M., Bose, R. K., Grande, A. M., Van Der Zwaag, S., Schubert, U. S., Garcia, S. J., & Hager, M. D. (2015). Characterization of Self-Healing polymers: From macroscopic healing tests to the molecular mechanism. *In Advances in Polymer Science* (pp. 113–142). [CrossRef]

Borui, L., Dang, J., Zhuang, Q., & Lv, Z. (2022). Recent Advances in Inorganic Electrochromic Materials from Synthesis to Applications: Critical Review on Functional Chemistry and Structure Engineering. *Chemistry-An Asian Journal, 17*. [CrossRef]

Boscolo, A., Menosso, E., Piuzzi, B., Toppano, M. (2007). *Thermochromic materials for temperature sensors in new applications*. In Springer eBooks (pp. 139–144).

Cao, L., Gao, D. (2010). Transparent superhydrophobic and highly oleophobic coatings. *Faraday Discussions, 146*, 57. [CrossRef]

Chabas, A., Lombardo, T., Cachier, H., Pertuisot, M., Oikonomou, K., Falcone, R., Verità, M., Geotti-Bianchini, F. (2008). Behaviour of self-cleaning glass in urban atmosphere. *Building and Environment, 43*, 2124–2131. [CrossRef]

Chang, T., Cao, X., Dedon, L. R., Long, S., Huang, A., Shao, Z., Li, N., Luo, H., & Jin, P. (2018). Optical design and stability study for ultrahigh-performance and long-lived vanadium dioxide-based thermochromic coatings. *Nano Energy, 44*, 256–264. [CrossRef]

Charfi, A., Bouraoui, T., Feki, M., Bradaï, C., & Normand, B. (2009). Surface treatment and corrosion behaviour of Fe–32Mn–6Si shape memory alloy. *Comptes Rendus Chimie, 12*, 270–275. [CrossRef]

Coccia, M., Farotti, E., & Lattanzi, A. (2022). Evaluation of the thermomechanical Shape memory polymers in equi-biaxial condition by hydraulic bulge test. *IOP Conference Series: Materials Science and Engineering, 1214*, 012036. [CrossRef]

Crowell, P. A., Wong, G. K., & Reppy, J. D. (1990). Measurement of the superfluid density in silica aerogels. *Physica B: Condensed Matter, 165–166*, 549–550. [CrossRef]

Cunha, M. F., Sobrinho, J. M. B., Da Rocha Souto, C., Santos, A. J. V. D., De Castro, A. C., Ries, A., & Sarmento, N. L. (2019). Transformation temperatures of shape memory alloy based on electromechanical impedance technique. *Measurement, 145*, 55–62. [CrossRef]

Davraz, M., & Bayrakçı, H. C. (2013). Performance properties of vacuum insulation panels produced with various filling materials. *Science and Engineering of Composite Materials. 21*, 521–527. [CrossRef]

Delgado, J. M., Martinho, J. C., Sá, A. V., Guimarães, A. S., & Abrantes, V. (2018). *Thermal Energy Storage with Phase Change Materials: A Literature Review of Applications for Buildings Materials*. Springer. [CrossRef]

deMello, A. J. (2006). Control and detection of chemical reactions in microfluidic systems. *Nature, 442*, 394–402. [CrossRef]

Deputatova, L. V., Syrovatka, R. A., Vasilyak, L. M., Филинов, B. C., Lapitsky, D. S., Vladimirov, V. I., & Pecherkin, V. Y. (2018). Linear electrodynamic trap as a tool for cleaning dusty surfaces. *Contributions to Plasma Physics, 59*, 340–344. [CrossRef]

Di Bari, R., Horn, R., Nienborg, B., Klinker, F., Kieseritzky, E., & Pawelz, F. (2020). The environmental potential of phase change materials in building applications. A multiple case investigation based on life cycle assessment and building simulation. *Energies, 13*, 3045. [CrossRef]

Dornelas, V. M., De Oliveira, S. A., Savi, M. A., Pacheco, P. M. C. L., & De Souza, L. F. G. (2021). Fatigue on shape memory alloys: Experimental observations and constitutive modeling. *International Journal of Solids and Structures, 213*, 1–24. [CrossRef]

Egea, A., Molina-García, Á., Herrero-Martín, R., & Pérez-García, J. (2022). Accelerated testing methods to analyse long term stability of a Phase Change Material under the combined effect of shear stress and thermal cycling. *Journal of Energy Storage, 56*, 105867. [CrossRef]

Ehrburger-Dolle, F., Dallamano, J., Elaloui, E., & Pajonk, G. M. (1995). Relations between the texture of silica aerogels and their preparation. *Journal of Non-Crystalline Solids, 186*, 9–17. [CrossRef]

Elgrishi, N., Rountree, K., McCarthy, B. D., Rountree, E. S., Eisenhart, T. T., & Dempsey, J. L. (2017). A practical Beginner's guide to cyclic voltammetry. *Journal of Chemical Education, 95*, 197–206. [CrossRef]

Fabretto, M., Vaithianathan, T., Hall, C., Murphy, P., Innis, P. C., Mazurkiewicz, J., & Wallace, G. G. (2007). Colouration efficiency measurements in electrochromic polymers: The importance of charge density. *Electrochemistry Communications, 9*, 2032–2036. [CrossRef]

Fan, H., Li, K., Liu, X., Xu, K., Su, Y., Hou, C., Zhang, Q., Li, Y., & Wang, H. (2020). Continuously Processed, Long Electrochromic Fibers with Multi-Environmental Stability. *ACS Applied Materials & Interfaces, 12*, 28451–28460. [CrossRef]

Fan, L., Rong, M. Z., Zhang, M. Q., & Chen, X. (2018). Repeated Intrinsic Self-Healing of Wider Cracks in Polymer via Dynamic Reversible Covalent Bonding Molecularly Combined with a Two-Way Shape Memory Effect. *ACS Applied Materials & Interfaces, 10*, 38538–38546. [CrossRef]

Fawaier, M., & Bokor, B. (2022). Dynamic insulation systems of building envelopes: A review. *Energy and Buildings, 270*, 112268.

Fiksman, G. (1997). Optical memory effects in sol-gel gel-glass based thermochromic material. *Optical Engineering, 36*, 1766. [CrossRef]

Fink, A., Fu, Z., & Körner, C. (2023). Functional properties and shape memory effect of Nitinol manufactured via electron beam powder bed fusion. *Materialia, 30*, 101823. [CrossRef]

Fisher, G. (2003). Chemical Analysis of Nickel-Manganese-Gallium Alloys. *Defence R&D Canada – Atlantic*, 1–22.

Fisher, H., Woolard, P., Ross, C. J., Kunkel, R., Bohnstedt, B. N., Liu, Y., & Lee, C. (2020). Thermomechanical data of polyurethane shape memory polymer: Considering varying compositions. *Data in Brief, 32*, 106294. [CrossRef]

Flexible Eddy Current Test Probe Using a Shape-Memory Alloy for. (2021, March 2). *Southwest Research Institute*. Retrieved from https://www.swri.org/patents/flexible-eddy-current-test-10895554

FTP Code. (2020). *International Code for Application of Fire Test Procedures*, 2010 Edition. International Maritime Organization.

Fu, F., & Hu, L. (2017). *Temperature sensitive colour-changed composites*. In Elsevier eBooks (pp. 405–423). [CrossRef]

Fulcher, J., Yang, L., Tandon, G. P., & Foster, D. C. (2010). Thermomechanical characterization of shape memory polymers using high temperature nanoindentation. *Polymer Testing, 29*, 544–552. [CrossRef]

Gall, K., Dunn, M. L., Liu, Y., Finch, D. S., Lake, M. S., & Munshi, N. A. (2002). Shape memory polymer nanocomposites. *Acta Materialia, 50*, 5115–5126. [CrossRef]

Gan, B., Gatepin, M., Cantonwine, S., & Tin, S. (2012). In situ characterization of the martensitic transformation temperature of NiTi shape memory alloys via instrumented microindentation. *Philosophical Magazine Letters, 92*, 254–261. [CrossRef]

Garber-Slaght, R., & Craven, C. (2012). EVALUATING WINDOW INSULATION FOR COLD CLIMATES. *Journal of Green Building, 7*, 32–48. [CrossRef]

Goda, I., Zubair, Z., L'Hostis, G., & Dréan, J. (2020). Design and characterization of 3D multilayer woven reinforcements shape memory polymer composites. *Journal of Composite Materials, 55*, 653–673. [CrossRef]

Gojević, A., Grubeša, I. N., Marković, B., Juradin, S., & Crnoja, A. (2023). Autonomous Self-Healing methods as a potential technique for the improvement of concrete's durability. *Materials, 16*, 7391. [CrossRef]

Goldade, V., Shil'ko, S., & Neverov, A. (2015). *Smart Materials Taxonomy*. CRC Press. [CrossRef]

Granqvist, C. G., Arvizu, M. A., Pehlivan, İ. B., Qu, H., Wen, R., & Niklasson, G. A. (2018a). Electrochromic materials and devices for energy efficiency and human comfort in buildings: A critical review. *Electrochimica Acta, 259*, 1170–1182. [CrossRef]

Granqvist, C. G., Arvizu, M. A., Pehlivan, İ. B., Qu, H., Wen, R., & Niklasson, G. A. (2018b). Electrochromic materials and devices for energy efficiency and human comfort in buildings: A critical review. *Electrochimica Acta, 259*, 1170–1182. [CrossRef]

Grinshpun, S. A., Adhikari, A., Honda, T., Kim, K. Y., Toivola, M., Rao, K. S., & Reponen, T. (2006). Control of Aerosol Contaminants in Indoor Air: Combining the Particle Concentration Reduction with Microbial Inactivation. *Environmental Science & Technology, 41*, 606–612. [CrossRef]

Haimei, L., Guo, Q., Zhao, T., Zuo, P., & Fengming, E. (2023). Effects of aging and immersion on the healing property of Asphalt–Aggregate interface and relationship to the healing potential of asphalt mixture. *Materials, 16*, 3574. [CrossRef]

Haj-Ali, R., Eliasi, R., Fourman, V., Tzur, C., Bar, G., Grossman, E., Verker, R., Gvishi, R., Gouzman, I., & Eliaz, N. (2016). Mechanical characterization of aerogel materials with digital image correlation. *Microporous and Mesoporous Materials, 226*, 44–52. [CrossRef]

Hamilton, A., Sottos, N. R., & White, S. R. (2011). Pressurized vascular systems for self-healing materials. *Journal of the Royal Society Interface, 9*, 1020–1028.

Hartl, D. J., & Lagoudas, D. C. (2008). *Thermomechanical characterization of shape memory alloy materials*. In Springer eBooks (pp. 53–119). [CrossRef]

Hashemi, Y. M., Kadkhodaei, M., Sgambitterra, E., & Maletta, C. (2023). On the characterization of the compressive response of shape memory alloys using bending. *Smart Materials and Structures, 32*, 035033. [CrossRef]

Hassab, S., Shen, D. E., Österholm, A. M., Da Rocha, M., Song, G., Alesanco, Y., Viñuales, A., Rougier, A., Reynolds, J. R., & Padilla, J. (2018). A new standard method to calculate electrochromic switching time. *Solar Energy Materials and Solar Cells, 185*, 54–60. [CrossRef]

Hickey, A., Gonda, I., Irwin, W. J., & Fildes, F. (1990). Effect of hydrophobic coating on the behavior of a hygroscopic aerosol powder in an environment of controlled temperature and relative humidity. *Journal of Pharmaceutical Sciences, 79*, 1009–1014. [CrossRef]

Hongisto, V., Saarinen, P., Alakoivu, R., & Hakala, J. (2022). Acoustic properties of commercially available thermal insulators – An experimental study. *Journal of Building Engineering, 54*, 104588. [CrossRef]

Huang, W., Ding, Z., Wang, C., Wei, J., Zhao, Y., & Purnawali, H. (2010). Shape memory materials. *Materials Today, 13*, 54–61. [CrossRef]

Huang, X., Panahi-Sarmad, M., Dong, K., Li, R., Chen, T., & Xiao, X. (2021). Tracing evolutions in electro-activated shape memory polymer composites with 4D printing strategies: A systematic review. *Composites Part A: Applied Science and Manufacturing, 147*, 106444. [CrossRef]

Huang, Y., Stonehouse, A., & Abeykoon, C. (2023). Encapsulation methods for phase change materials – A critical review. *International Journal of Heat and Mass Transfer, 200*, 123458. [CrossRef]

Ibarra, D. S., Jacob, M., Li, F., Lü, H., Li, G., & Chen, J. (2022). Deep learning for predicting the thermomechanical behavior of shape memory polymers. *Polymer, 261*, 125395. [CrossRef]

Ibrahim, N. I., Al-Sulaiman, F. A., Saidur, R., Yilbaş, B. S., & Sahin, A. Z. (2017). Heat transfer enhancement of phase change materials for thermal energy storage applications: A critical review. *Renewable & Sustainable Energy Reviews, 74*, 26–50. [CrossRef]

International Maritime Organization (IMO). (2021). SOLAS - *International Convention for the Safety of Life at Sea*. IMO Publications.

Ismaeel, W. S. (2023). *The dynamics of sustainable material selection for Green-Certified Projects. Buildings, 13*, 2077. [CrossRef]

Jacobson, N. D., & Iroh, J. O. (2021). Shape memory Corrosion-Resistant polymeric materials. *International Journal of Polymer Science*, 2021, 1–18. [CrossRef]

Jani, J. M., Leary, M., Subic, A., & Gibson, M. (2014). A review of shape memory alloy research, applications and opportunities. *Materials in Engineering, 56*, 1078–1113. [CrossRef]

Jelle, B. P., & Hägen, G. (1993). Transmission spectra of an electrochromic window based on polyaniline, Prussian blue and tungsten oxide. *Journal of the Electrochemical Society, 140*, 3560–3564. [CrossRef]

Jensen, J., Madsen, M. V., & Krebs, F. C. (2013). Photochemical stability of electrochromic polymers and devices. *Journal of Materials Chemistry C, 1*, 4826. [CrossRef]

Jia, Z., Bao, W., Tao, C., & Song, W. (2021). Reversibly photochromic wood constructed by depositing microencapsulated/polydimethylsiloxane composite coating. *Journal of Forestry Research, 33*, 1409–1418. [CrossRef]

Jin, R., Zhou, Z., Liu, J., Shi, B., Zhou, N., Wang, X., Jia, X., Guo, D., & Jin, X. (2023). Aerogels for thermal protection and their application in aerospace. *Gels, 9*, 606. [CrossRef]

Johnson, W. L., Demko, J. A., Fesmire, J. E., & Weisend, J. G. (2010). Analysis and testing of multilayer and aerogel insulation configurations. *AIP Conference Proceedings*. [CrossRef]

Joo, S. J., Yu, M. H., Kim, W. S., & Kim, K. H. (2018). Damage detection and self-healing of carbon fiber polypropylene (CFPP)/carbon nanotube (CNT) nano-composite via addressable conducting network. *Composites Science and Technology, 167*, 62–70. [CrossRef]

Kang, G., & Song, D. (2015). Review on structural fatigue of NiTi shape memory alloys: Pure mechanical and thermo-mechanical ones. *Theoretical and Applied Mechanics Letters, 5*, 245–254. [CrossRef]

Kim, J., Boafo, F. E., Kim, S., & Kim, J. (2017). Aging performance evaluation of vacuum insulation panel (VIP). *Case Studies in Construction Materials, 7*, 329–335. [CrossRef]

Kim, M., Jang, S., Choi, S. W., Yang, J., Kim, J., & Choi, D. Y. (2021a). Analysis of shape memory behavior and mechanical properties of shape memory polymer composites using thermal conductive fillers. *Micromachines, 12*, 1107. [CrossRef]

Kim, M., Jang, S., Choi, S. W., Yang, J., Kim, J., & Choi, D. Y. (2021b). Analysis of shape memory behavior and mechanical properties of shape memory polymer composites using thermal conductive fillers. Micromachines, 12, 1107. [CrossRef]

Kim, Y. U., Chang, S. J., Lee, Y. J., No, H., Choi, G., & Kim, S. (2021). Evaluation of the applicability of high insulation fire door with vacuum insulation panels: Experimental results from fire resistance, airtightness, and condensation tests. *Journal of Building Engineering, 43*, 102800. [CrossRef]

Ko, K., Cho, T., Ham, D. S., Kang, M., Choi, W. J., & Cho, S. (2022). Preparation of highly adhesive urethane–acrylate-based gel-polymer electrolytes and their optimization in flexible electrochromic devices. *Journal of Electroanalytical Chemistry, 917*, 116423. [CrossRef]

Kotzé, J. P., Von Backström, T. W., & Erens, P. (2014). Simulation and Testing of a Latent Heat Thermal Energy Storage Unit with Metallic Phase Change Material. *Energy Procedia, 49*, 860–869. [CrossRef]

Kožuh, S., Gojić, M., Ivanić, I., Grgurić, T. H., Kosec, B., & Anžel, I. (2018). The effect of heat treatment on the microstructure and mechanical properties of CU-AL-MN shape memory alloy. *Kemija U Industriji, 67*, 11–17. [CrossRef]

Kulkov, S. N. (2019). Smart Materials based on a high and low temperatures SME-Alloys. IOP Conference Series: *Materials Science and Engineering, 613*, 012002. [CrossRef]

Lakatos, A. (2022). Novel Thermal Insulation Materials for Buildings. *Energies, 15*, 6713. [CrossRef]

Lavernhe-Taillard, K., Calloch, S., Chirani, S. A., & Lexcellent, C. (2009). Multiaxial shape memory effect and superelasticity. *Strain, 45*, 77–84. [CrossRef]

Lee, J., Kim, H. W., Lee, J., An, H., & Chung, C. (2021). Microcapsule-Type Self-Healing Protective Coating That Can Maintain Its Healed State upon Crack Expansion. *Materials, 14*, 6198. [CrossRef]

Lee, M. W., An, S., Yoon, S. S., & Yarin, A. L. (2018). Advances in self-healing materials based on vascular networks with mechanical self-repair characteristics. *Advances in Colloid and Interface Science, 252*, 21–37. [CrossRef]

Lee, T., Jeong, S., Woo, U., Choi, H., & Jung, D. S. (2023). Experimental evaluation of shape memory alloy retrofitting effect for circular concrete column using

ultrasonic pulse velocity. *International Journal of Concrete Structures and Materials, 17*. [CrossRef]

Lendlein, A. (2010). *Characterization Methods for Shape-Memory Polymers. In Shape-Memory Polymers* (Vol. 226, pp. 97–143). Springer Science & Business Media. [CrossRef]

Lexcellent, C., Leclercq, S., Gabry, B., & Bourbon, G. (2000). The two-way shape memory effect of shape memory alloys: an experimental study and a phenomenological model. *International Journal of Plasticity, 16*, 1155–1168. [CrossRef]

Li, G., & Feng, X. (2022). *Recent advances in smart Self-Healing polymers and composites*. Woodhead Publishing. [CrossRef]

Li, G., & Wang, A. (2016). Cold, warm, and hot programming of shape memory polymers. *Journal of Polymer Science Part B, 54*, 1319–1339. [CrossRef]

Li, R., Ma, X., Li, J., Cao, J., Gao, H., Li, T., Zhang, X., Wang, L., Zhang, Q., Wang, G., Hou, C., Li, Y., Palacios, T., Lin, Y., Wang, H., & Ling, X. (2021). Flexible and high-performance electrochromic devices enabled by self-assembled 2D TiO2/MXene heterostructures. *Nature Communications, 12*. [CrossRef]

Liu, B., Wang, M., Du, W., Jiang, L., Li, H., Wang, L., Li, J., Zuo, D., & Ding, Q. (2023). The Application of Self-Healing Microcapsule Technology in the field of Cement-Based Materials: *A Review and Prospect. Polymers, 15*, 2718. [CrossRef]

Liu, K., & Jiang, L. (2012). Bio-Inspired Self-Cleaning surfaces. *Annual Review of Materials Research, 42*, 231–263. [CrossRef]

Liu, N., & Huang, W. (2006). DSC study on temperature memory effect of NiTi shape memory alloy. *Transactions of Nonferrous Metals Society of China, 16*, 37–41. [CrossRef]

Liu, Y., Zhang, Y., Chen, T., Jin, Z., Feng, W., Li, M., Chen, L., & Wang, C. (2023). A stable and Self-Healing thermochromic polymer coating for all weather thermal regulation. *Advanced Functional Materials, 33*. [CrossRef]

Liu, Y., & Zhang, X. (2020). Bio-Inspired Self-Healing Surfaces with Mechanical Adaptability: A Review. *Soft Matter, 16*, 5466–5478.

Luo, H., Lu, H., & Leventis, N. (2006). The compressive behavior of isocyanate-crosslinked silica aerogel at high strain rates. *Mechanics of Time-Dependent Materials, 10*, 83–111. [CrossRef]

Ma, E., Chen, X., Lai, J., Kong, X., & Guo, C. (2023). Self-healing of microcapsule-based materials for highway construction: A review. *Journal of Traffic and Transportation Engineering (English Edition), 10*, 368–384. [CrossRef]

Mao, W., Litina, C., & Al-Tabbaa, A. (2020). Development and application of novel sodium silicate Microcapsule-Based Self-Healing Oil Well cement. *Materials, 13*, 456. [CrossRef]

Martins, G. S. (2019a). Differential scanning thermal analysis of Shape-Memory polymers, polymer blends and composites. *In Advanced structured materials* (pp. 153–166). [CrossRef]

Martins, G. S. (2019b). Differential scanning thermal analysis of Shape-Memory polymers, polymer blends and composites. *In Advanced structured materials* (pp. 153–166). [CrossRef]

Materials, *G. I. O. N. A performance test method of electrochromic device*. Retrieved from https://eureka.patsnap.com/patent-CN110824197B

McKinley, G. (2004). Actuation of shape memory polymer using magnetic fields for applications in medical devices.*Department of Mechanical Engineering, Massachusetts Institute of Technology*, 144.

Meddour, B., & Brek, S. (2018). *Modeling of the Two-Way shape memory effect*. In InTech eBooks.

Meir, S., Gordon, S., Karsh, M., Wiezman, A., Ayers, R., & Olson, D. L. (2011). Nondestructive evaluation of ni-ti shape memory alloy. *AIP Conference Proceedings*. [CrossRef]

Mirzamojeni, M., Aghayan, I., & Behzadian, R. (2023). Evaluation of field aging effect on self-healing capability of asphalt mixtures. *Construction and Building Materials, 369*, 130571. [CrossRef]

Mohamed, A., Salehi, S., Ahmed, R., & Li, G. (2022). Experimental study on rheological and settling properties of shape memory polymer for fracture sealing in geothermal formations. *Journal of Petroleum Science and Engineering, 208*, 109535. [CrossRef]

Moner-Girona, M., Roig, A., Molins, E., Martínez, E., & Esteve, J. (1999). Micromechanical properties of silica aerogels. *Applied Physics Letters, 75*, 653–655. [CrossRef]

Mphahlele, K., Ray, S. S., & Колесников, A. B. (2017). Self-Healing Polymeric Composite Material Design, Failure Analysis and Future Outlook: A review. *Polymers, 9*, 535. [CrossRef]

Naresh, C., Bose, P. S. C., & Rao, C. (2016). Shape memory alloys: a state of art review. IOP Conference Series: *Materials Science and Engineering, 149*, 012054. [CrossRef]

Nikafkar, M., & Berardi, U. (2020). Experimental verification of the theoretical aging of vacuum insulated panels. *XV International Conference on Durability of Building Materials and Components. eBook of Proceedings*. [CrossRef]

Ning, J., Chen, S., Wang, J., He, C., Fang, K., Yin, H., Liu, Y., Li, Y., & Yu, D. (2023). Smart thermally responsive perovskite materials: Thermo-chromic application and density function theory calculation. *Heliyon, 9*, e12845. [CrossRef]

Nunayon, S. S., Zhang, H., & Lai, A. C. (2019). Comparison of disinfection performance of UVC-LED and conventional upper-room UVGI systems. *Indoor Air, 30*, 180–191. [CrossRef]

Ohki, T., Ni, Q., Ohsako, N., & Iwamoto, M. (2004). Mechanical and shape memory behavior of composites with shape memory polymer. *Composites Part A: Applied Science and Manufacturing, 35*, 1065–1073. [CrossRef]

Ostrý, M., Bantová, S., & Struhala, K. (2019). Tests on material compatibility of phase change materials and selected plastics. *Molecules, 24*, 1398. [CrossRef]

Padilla, J., Niklaus, L., Schott, M., Posset, U., Faceira, B., Mjejri, I., Rougier, A., Alesanco, Y., Viñuales, A., Shen, D. E., Österholm, A. M., & Reynolds, J. R. (2023). Quantitative assessment of the cycling stability of different electrochromic materials and devices. *ACS Applied Optical Materials, 1*, 1174–1183. [CrossRef]

Pan, H., Li, Y., Zhang, H., Sun, D., Hu, X., Yang, J., & Xu, F. (2022). In situ investigation of the healing process in dual-microcapsule self-healing materials by the synchrotron radiation computed tomography. *Composites Part A: Applied Science and Manufacturing, 158*, 106955. [CrossRef]

Park, C., Kim, J., Kim, Y., Bae, S., Do, M., Im, S., & Yoo, S. D. (2021). High-Coloration Efficiency and Low-Power Consumption Electrochromic Film based on Multifunctional Conducting Polymer for Large Scale Smart Windows. *ACS Applied Electronic Materials, 3*, 4781–4792. [CrossRef]

Park, S. I., Quan, Y., Kim, S., Kim, H., Kim, S., Chun, D., Lee, C. S., Taya, M., Chu, W., & Ahn, S. (2016). A review on fabrication processes for electrochromic devices. *International Journal of Precision Engineering and Manufacturing-Green Technology, 3*, 397–421. [CrossRef]

Pehlivan, E., Granqvist, C. G., & Niklasson, G. A. (2021). Impedance spectroscopy of electrochromic hydrous tungsten oxide films. *Electronic Materials, 2*, 312–323. [CrossRef]

Peijnenburg, W. J., Oomen, A. G., Soeteman-Hernández, L. G., Groenewold, M., Sips, A. J. a. M., Noorlander, C., Kettelarij, J., & Bleeker, E. A. (2021). Identification of emerging safety and sustainability issues of advanced materials: Proposal for a systematic approach. *NanoImpact, 23*, 100342. [CrossRef]

Perego, D. L. (2008). Ageing tests and recovery procedures of silica aerogel. *Nuclear Instruments and Methods in Physics Research Section A: Accelerators, Spectrometers, Detectors and Associated Equipment, 595*, 224–227. [CrossRef]

Peters, S., & Drewes, D. (2019). *Materials in progress: Innovations for designers and architects*. Birkhäuser. [CrossRef]

Pierre, A. C., & Anderson, M. A. (2011). *Aerogels: Synthesis, Characterization, and Applications*. Wiley.

Pradhan, S., Sahu, S. K., Pramanik, J., & Badgayan, N. D. (2022). An insight into mechanical & thermal properties of shape memory polymer reinforced with nanofillers; a critical review. *Materials Today: Proceedings, 50*, 1107–1112. [CrossRef]

Putra, N., Hakim, I. I., Erwin, F. P., Abdullah, N. A., Ariantara, B., Amin, M., Mahlia, T., & Kusrini, E. (2019). Development of a novel thermoelectric module based device for thermal stability measurement of phase change materials. *Journal of Energy Storage, 22*, 331–335. [CrossRef]

Rahman, A., Penco, M., Peroni, I., Ramorino, G., Janszen, G., & Di Landro, L. A. (2012). Autonomous healing materials based on epoxidized natural rubber and ethylene methacrylic acid ionomers. *Smart Materials and Structures, 21*, 035014. [CrossRef]

Rai, V., Singh, R. S., Blackwood, D. J., & Zhao, D. (2020). A review on Recent Advances in Electrochromic Devices: A Material Approach. *Advanced Engineering Materials, 22*. [CrossRef]

Ritter, A. (2006). *Smart materials in architecture, interior architecture and design*. Walter de Gruyter.

Rondelli, G. (1996). Corrosion resistance tests on NiTi shape memory alloy. *Biomaterials, 17*, 2003–2008. [CrossRef]

Rybak, A., Malinowski, Ł., Adamus-Włodarczyk, A., & Ulański, P. (2021). Thermally Conductive Shape Memory Polymer Composites Filled with Boron Nitride for Heat Management in Electrical Insulation. *Polymers, 13*, 2191. [CrossRef]

Sampath, S., Harris, W. B. J., & Srivatsan, T. S. (2023). Environment-Induced Degradation of shape Memory alloys: Role of alloying and nature of environment. *Materials, 16*, 5660. [CrossRef]

Schmidt, D. L., Coburn, C. E., DeKoven, B. M., Potter, G. E., Meyers, G. F., Fischer, D. A. (1994). Water-based non-stick hydrophobic coatings. *Nature, 368*, 39–41. [CrossRef]

Selvarajoo, T., Davies, R., Freeman, B. L., & Jefferson, T. (2020). Mechanical response of a vascular self-healing cementitious material system under varying loading conditions. *Construction and Building Materials, 254*, 119245. [CrossRef]

Shields, Y., De Belie, N., Jefferson, T., & Van Tittelboom, K. (2021). A review of vascular networks for self-healing applications. *Smart Materials and Structures, 30*, 063001. [CrossRef]

Ślosarczyk, A. (2021). Carbon microfibers/silica aerogel nanocomposites based on water-glass. *Advanced Materials Proceedings, 3*, 45–49. [CrossRef]

Sofocleous, K., Ogin, S., Tsakiropoulos, P., Draconakis, V., & Doumanidis, C. C. (2013). Controlled impact testing of woven fabric composites with and without reinforcing shape-memory alloy wires. *Journal of Composite Materials, 48*, 3799–3813. [CrossRef]

Soltan, A., Esen, İ., Kara, S. A., & Ahlatçı, H. (2023). Examination of the corrosion behavior of shape memory NITI material for biomedical applications. *Materials, 16*, 3951. [CrossRef]

Somani, P. R., & Radhakrishnan, S. (2003). Electrochromic materials and devices: present and future. *Materials Chemistry and Physics, 77*, 117–133. [CrossRef]

Staszczak, M., Kalat, M. N., Golasiński, K., Urbański, Ł., Takeda, K., Matsui, R., & Pieczyska, E. A. (2022). Characterization of polyurethane shape memory polymer and determination of shape fixity and shape recovery in subsequent thermomechanical cycles. *Polymers, 14*, 4775.[CrossRef]

Sun, L., Huang, W., Ding, Z., Zhao, Y., Wang, C. C., Purnawali, H., & Tang, C. (2012). Stimulus-

responsive shape memory materials: A review. *Materials in Engineering, 33*, 577–640. [CrossRef]

Tcharkhtchi, A., Abdallah-Elhirtsi, S., Ebrahimi, K., Fitoussi, J., Shirinbayan, M., & Farzaneh, S. (2014). Some new concepts of shape memory effect of polymers. *Polymers, 6*, 1144–1163. [CrossRef]

Tobushi, H., Matsui, R., Takeda, K., & Hayashi, S. (2015). *Mechanical testing of shape-memory polymers for biomedical applications*. In Elsevier eBooks (pp. 65–75). [CrossRef]

Tracy, C. E., Zhang, J., Benson, D. K., Czanderna, A. W., & Deb, S. K. (1999). Accelerated durability testing of electrochromic windows. *Electrochimica Acta, 44*, 3195–3202. [CrossRef]

Treml, S., Engelhardt, M., Sprengard, C., & Butko, W. (2019). Determination of the internal pressure of vacuum insulation panels with the envelope lift-off technique – methods for analysing test data. *Energy and Buildings, 184*, 44–52. [CrossRef]

Viková, M., & Vik, M. (2023). Transition temperature of color change in thermochromic systems and its description using sigmoidal models. *Materials, 16*, 7478. [CrossRef]

Vili, Y. Y. F. C. (2007). Investigating smart textiles based on shape memory materials. *Textile Research Journal, 77*, 290–300. [CrossRef]

Wałęsa-Chorab, M., & Skene, W. G. (2020). Extending the color retention of an electrochromic device by immobilizing color switching and Ion-Storage complementary layers. *Electronic Materials, 1*, 40–53. [CrossRef]

Wang, B., Liu, J., Liu, M., & Chen, G. (2023). Preparation and corrosion resistance of shape memory self-healing coatings responsive to near-infrared light. *Polymer Testing, 126*, 108146. [CrossRef]

Wang, D., Sun, Q., Hokkanen, M. J., Zhang, C., Lin, F., Liu, Q., Zhu, S., Zhou, T., Chang, Q., He, B., Zhou, Q., Chen, L., Wang, Z., Ras, R. H. A., & Deng, X. (2020). Design of robust superhydrophobic surfaces. *Nature, 582*, 55–59. [CrossRef]

Wang, H., Zhang, Y., & Tan, Z. (2023). Dynamic Response and Deformative Mechanism of the Shape Memory Polymer Filled with Low-Melting-Point Alloy under Different Dynamic Loads. *Polymers, 15*, 423. [CrossRef]

Wang, J., Chen, Y., An, J., Xu, K., Chen, T., Müller-Buschbaum, P., & Zhong, Q. (2017). Intelligent Textiles with Comfort Regulation and Inhibition of Bacterial Adhesion Realized by Cross-Linking Poly(n-isopropylacrylamide-co-ethylene glycol methacrylate) to Cotton Fabrics. *ACS Applied Materials & Interfaces, 9*, 13647–13656. [CrossRef]

Wang, L., & Tang, S. (2022). High-Performance construction Materials: latest advances and Prospects. *Buildings, 12*, 928. [CrossRef]

White, S. R., Maiti, S., Jones, A. S., Brown, E. N., Sottos, N. R., & Geubelle, P. H. (2005). Fatigue of self-healing polymers: Multiscale analysis and experiments. *11th International Conference on Fracture 2005*, ICF11, 3888–3891.

White, S. R., Sottos, N. R., Geubelle, P. H., Moore, J. S., Kessler, M. R., Sriram, S. R., Brown, E. N., Viswanathan, S. (2001). Autonomic healing of polymer composites. *Nature, 409*, 794–797. [CrossRef]

Wu, Y., Ju, D., Yang, L., Zhao, H., Wang, H., Sun, C., Wu, Y., Cao, Z., & Guo, B. (2020). Evaluation of radiation damage behavior in polyimide aerogel by infrared camera and photoacoustic spectroscopy. *Polymer Testing, 85*, 106405. [CrossRef]

Wu, Y., Mishra, Y. K., & Xiong, J. (2023). Electrochromic Materials: scope for the cyclic decay mechanisms and performance stability optimization strategies. *Coloration Technology*. [CrossRef]

Xia, Z., Wang, H., Su, Y., Tang, P., Dai, M., Lin, H., Zhang, Z., & Shi, Q. (2020). Enhanced electrochromic properties by improvement of crystallinity for sputtered WO3 film. *Coatings, 10*, 577. [CrossRef]

Xu, C., Zhang, H., & Fang, G. (2022). Review on thermal conductivity improvement of phase change materials with enhanced additives for thermal energy storage. *Journal of Energy Storage, 51*, 104568. [CrossRef]

Xu, T., Walter, E., Agrawal, A., Bohn, C. D., Velmurugan, J., Zhu, W., Lezec, H. J., & Talin, A. A. (2016). High-contrast and fast electrochromic switching enabled by plasmonics. *Nature Communications, 7*. [CrossRef]

Ye, T., Sun, Y., Zhao, X., Lin, B., Yang, H., Zhang, X., & Le, G. (2018). Long-term-stable, solution-processable, electrochromic carbon nanotubes/polymer composite for smart supercapacitor with wide working potential window. *Journal of Materials Chemistry A, Materials for Energy and Sustainability, 6*, 18994–19003. [CrossRef]

Yoshida, N., Takeuchi, M., Okura, T., Monma , H., Wakamura, M., Ohsaki, H., Watanabe, T. (2006). Super-hydrophobic photocatalytic coatings utilizing apatite-based photocatalyst. *Thin Solid Films, 502*, 108–111. [CrossRef]

Zaleska, A., Hänel, A., & Nischk, M. (2010). Photocatalytic air purification. *Recent Patents on Engineering, 4*, 200–216. [CrossRef]

Zhang, L., Hoff, I., Zhang, X., & Yang, C. (2022). Investigation of the self-healing and rejuvenating properties of aged asphalt mixture containing multi-cavity Ca-alginate capsules. *Construction and Building Materials, 361*, 129685. [CrossRef]

Zhao, B., Peng, N., Liang, C., Yong, W. F., Chung, T. S. (2015). Hollow fiber membrane dehumidification device for air conditioning system. *Membranes, 5*, 722–738. [CrossRef]

Zhao, Q., Hu, Q., & Xie, T. (2015). Recent progress in shape memory polymer: New behavior, enabling materials, and mechanistic understanding. *Progress in Polymer Science, 49–50*, 79–120. [CrossRef]

Zhao, W., Yang, J., Zhou, J., Xu, F., Zrínyi, M., Dussault, P. H., Osada, Y., Chen, Y. M. (2014). Self-healing gels

based on constitutional dynamic chemistry and their potential applications. *Chemical Society Reviews, 43*, 8114–8131. [CrossRef]

Zhou, K. (2020). Coloration and ion insertion Kinetics Study in Electrochromic WO3 films by Chronoamperometry. *International Journal of Electrochemical Science, 15*, 7821–7832. [CrossRef]

Zhou, Y., & Huang, W. (2015). Shape Memory Effect in Polymeric Materials: Mechanisms and optimization. *Procedia IUTAM, 12*, 83–92. [CrossRef]

Крыльский, Д. В. (2013, March 29). RU2524963C1 - *Electroconductive adhesive for electrochromic devices*. Retrieved from https://patents.google.com/patent/RU2524963C1/en

Research Articles

Review